FLIGHT DETERMINATION OF THE AERODYNAMIC STABILITY AND CONTROL CHARACTERISTICS OF THE NASA SGS 1-36 SAILPLANE IN THE CONVENTIONAL AND DEEP STALL ANGLES-OF-ATTACK OF BETWEEN -5 AND 75 DEGREES

FINAL REPORT

PRINCIPAL INVESTIGATORS

Faramarz A. Mahdavi

Doral R. Sandlin

June 1, 1984

California Polytechnic State University

Aeronautical Engineering Department

San Luis Obispo, California

Grant No. NCC4-1

TABLE OF CONTENTS

LIST OF FIGURES

LIST OF TABLES

SYMBOLS

All data are referenced to fuselage body axes according to right-handed sign conventions.

A	state equation matrix
a_n	normal acceleration, g
a_x	longitudinal acceleration, g
a_y	lateral acceleration g
B	state equation matrix
b	reference span, m (ft)
C	observation matrix
C_A	axial force coefficient
C_D	drag coefficient
CG	center of gravity, fraction of chord
C_L	lift coefficient
C_ℓ	rolling moment coefficient
C_m	pitching moment coefficient
C_N	normal force coefficient
C_n	yawing moment coefficient
C_Y	lateral force coefficient
c	reference chord, m (ft)
D	observation matrix
E	observation matrix
g	acceleration of gravity, m/sec^2 (ft/sec^2)

H	observation matrix
h	altitude, m (ft)
I	identity matrix
I_x	moment of inertia about roll axis, N-m^2 (slug-ft^2)
I_{xy}, I_{xz}, I_{yz}	cross products of inertia, N-m^2 (slug-ft^2)
I_y	moment of inertia about pitch axis, N-m^2 (slug-ft^2)
I_z	moment of inertia about yaw axis, N-m^2 (slug-ft^2)
J	cost functional
K_α, K_β	flow amplification factors for angle of attack and angle of sideslip
M	Mach number
m	mass, kg (slug)
q	pitch rate, deg/sec
$\bar{q}$	dynamic pressure, N/m^2 (lbf/ft^2)
R	state equation matrix
$\mathscr{R}$	degrees per radian (57.2958)
r	yaw rate, deg/sec
S	state equation matrix
s	reference area, m^2 (ft^2)
T	total time, sec
t	time, sec
u	control vector
V	velocity, m/sec (ft/sec)
W	*a priori* weighting matrix

x	state vector
α	angle of attack, deg
β	angle of sideslip, deg
Φ	bank angle, deg
δ	control deflection, deg
δ_a	aileron deflection, deg
δ_c	extra control deflection
δ_e	elevator deflection, deg
δ_r	rudder deflection, deg
δ_s	stabilator deflection, deg
θ	pitch angle, deg

Subscripts:

CG_{flt}, CG_{ref}	at flight or reference center of gravity
c	corrected
i, j, k	general indices
m	measured
p, q, r	rotary derivatives, per rad
α, β	static derivatives, per deg
δ, δ_a, δ_c, δ_e, δ_r, δ_s	control derivatives with respect to indicated quantity

Chapter 1

INTRODUCTION

In September of 1981 the National Aeronautics and Space Administration at the Ames/Dryden Flight Research Facility began the investigation of the "Deep Stall" phenomenon using a modified SGS 1-36 sailplane. This investigation was directed at demonstrating the feasibility of unpowered Controlled Deep Stall flights at angles-of-attack of between 30 and 75 degrees. The primary research objectives of the SGS 1-36 Controlled Deep Stall Sailplane Project was to control the aircraft in the Deep Stall regions by using large in-flight deflections of the all moveable horizontal stabilizer, and to assess the vehicle's longitudinal and lateral-directional dynamic stability and control characteristics. Initial qualitative flight tests were conducted on radio controlled model sailplanes having both low and high (T-tail) horizontal stabilizers. A quarter scale model of the modified SGS 1-36 was later used in wind tunnel tests at NASA Langley Research Center to obtain the static stability and control aerodynamic characteristics of the aircraft. These data along with the estimated rotary derivatives were incorporated into a fixed based flight simulation to facilitate engineering evaluation, pilot familiarization,

and planning for the full scale flight tests. Due to limited flight operations support and available time, only a total of twenty manned flight tests were conducted using the modified SGS 1-36 at C.G. positions of 33.1% and 28.4% Mean Aerodynamic Cord (MAC).

Since the early 1940's, several variations of the Deep Stall concept have been incorporated into "free flying" model airplanes to recover them rapidly and safely at the end of their flight by "popping" the horizontal tail using a timing device. This technique, called the "Dethermalizer" (Reference 1) , first introduced in 1942 by Carl Goldberg, has since generated interest toward the possible applications in safe recovery of high aspect ratio remotely piloted vehicles from high altitudes through turbulent atmospheric layers. In addition, in recent years several modern transport aircraft have experienced accidents related to the Deep Stall phenomenon either in service or during flight test programs. Despite the incorporation of computer-controlled stick pushers on many of these aircraft to prevent entering an angle-of-attack region where a Deep Stall could occur, several "T" tail configured aircraft (such as the British Aerospace BAC 111, Boeing 727, Canadair Challenger CL-600, F 101, F 104, and several high performance sailplanes) have crashed when they entered a stable deep stall where the pilot was not able to recover by means of normal stall recovery techniques because of inadequate pitch control (Reference 2).

Given adequate pitch authority through the use of large in-flight horizontal tail deflection, an uncontrolled flight may then become controllable. This increase in pitch control authority can be used in assisting to recover from inadvertent deep stall, spins, or spiral dives in IFR conditions. Additionally, near vertical descents in areas of restricted lateral maneuvering and precision recovery of Remotely Piloted Vehicles(RPV's) in conjunction with a retro-rocket landing system could be achieved using the controlled deep stall technique.

This report describes the flight test procedure and discusses the preliminary analysis of the results obtained from twenty manned flights of the SGS 1-36 in the high angles-of-attack Deep Stall region. A comparison of the flight determined stability and control derivatives and those of the wind tunnel and the estimated aerodynamic data is also presented. Furthermore, deep stall dynamic response of the SGS 1-36 is discussed briefly to explain some of the unexpected flight observations.

Chapter 2

VEHICLE DESCRIPTION AND MODIFICATIONS

The NASA SGS 1-36 Controlled Deep Stall Vehicle is a modified version of the standard single place, T-tail design Schweizer 1-36 sailplane that is commercially used as an advanced trainer. It is made primarily of aluminum structure and skin except the rudder surface that is fabric covered. The modifications were made to the fixed horizontal stabilizer, control cables, canopy, cockpit, and the nose cone of the aircraft.

The physical characteristics of the vehicle are presented in Tables 1 through 3. The aircraft moments of inertia listed were obtained experimentally by means of an "inertia swing". Measurements were made at 33.1% mean aerodynamic cord and the resulting inertia were analytically corrected to 23.8% mean aerodynamic cord C.G. position for data reduction of flights at this forward center of gravity. Figure 1 is a picture of the modified SGS 1-36. Figure 2 is a three-view drawing of the modified vehicle.

Aerodynamic control is accomplished by means of conventional manual control system. The pilot is provided a center stick for elevator and aileron control, pedals for rudder control, and a side control lever to deflect the

horizontal stabilizer. In addition, a spoiler control handle is provided for speed control and rapid descent.

The fixed, single control, standard T-tail was modified into an all moveable dual control horizontal tail configuration. The new configuration allows the horizontal stabilizer to be deflected from 0 to 73 degrees trailing edge up (Figure 3) through the use of the horizontal stabilizer control lever mounted on the port side of the cockpit (Figure 4). Only partial elevator travel authority is retained throughout the range of stabilizer deflection. As the stabilizer setting is increased to 73 degrees trailing edge up, the elevator travel authority is reduced from full -24 to +17 degrees deflection to only -11 to -24 degrees. Furthermore, two six-pound counter weights were added to the stabilizer to reduce the risk of in-flight flutter of the tail section (Figure 3).

During the original modifications to the horizontal stabilizer, cables and pulleys were employed to connect the stabilizer control lever to the stabilizer, but due to excessive cable elongation and friction under load, the cable and pulley system was replaced by a bellcrank and pushrod system.

In order to assure safe and quick pilot exit from the cockpit in case of an uncontrolled flight, several modifications were made to the cockpit and canopy. An "Egress" pneumatic escape system was added to the the cockpit that would enable the pilot to eject the canopy and

release his shoulder harness and seatbelt simultaneously, by pulling a single escape handle located to his right on the instrumentation panel (Figure 5).

The original nose cone was modified to accommodate a special made nose boom. Figure 6 contains a picture of the nose cone with the boom installed.

Chapter 3

INSTRUMENTATION

In flight data were obtained using the onboard data acquisition system and were transmitted and recorded digitally on magnetic tapes at the ground station. This system, a 28-channel 10-bit pulse code modulation telemetery system, consisted of a 3-axis rate gyro, a vertical gyro, 3-axis linear accelerometers, and control position transmitters (CPT's) to measure angular rates, Euler angles, linear accelerations, and control surface positions respectively. All of the system components are mounted on a single aluminum platform for easy installation and removal. Figure 7 depicts the data acquisition platform onboard the aircraft.

Angle-of-attack, angle-of-sideslip, dynamic pressure, and static pressure were measured using a special made nose boom. This nose boom contained a self-aligning pitot-static tube, angle-of-attack and angle-of-sideslip vanes and was wired to the data acquisition package onboard the aircraft (Figure 8). Corrections were made to the angle-of-attack and angle-of-sideslip data for boom position and alignment. The control surface position, angular rate, and translational acceleration data were taken at 110, 220, and 440 samples per second (SPS)

respectively. For post-flight data analysis the sample rate used was 50 samples per second for longitudinal, and 25 SPS for lateral-directional data. In addition to the basic flight instrumentation six flutter accelerometers were installed externally on the vertical and horizontal tail surfaces for initial ground and flight flutter clearance tests.

Table 4 includes the instrumentation parameters and their corresponding range, resolution, and accuracy.

Chapter 4

FLIGHT TEST PROCEDURES AND MANEUVERS

A total of twenty manned flight tests were conducted at C.G. positions of 33.1% and 28.4% Mean Aerodynamic Cord using the modified NASA SGS 1-36 vehicle. Prior to the first deep stall flight the C.G. position of 33% MAC was selected to assure that the aircraft will have adequate longitudinal stability in the conventional and deep stall flight regime (The standard SGS 1-36 is certified by the Federal Aviation Administration for flight at C.G. range of 20% to 40% MAC). It was also decided to fly the aircraft at the C.G. position of 28% MAC to increase the longitudinal stability and obtain trim data at this center of gravity configuration. Weight and balance measurements were made to verify the location of the vehicle's longitudinal center of gravity prior to initial flights at the two desired C.G. locations. Moments of inertia were determined experimentally at 33.1% mean aerodynamic cord by means of an "inertia swing" and corrected analytically for 28.4% mean aerodynamic cord center of gravity position.

Figure 11 is the complete flight schedule matrix indicatingthe number of flights and their respective C.G., stabilator setting, and control stick position.

As a glider, the SGS 1-36 was towed to an approximate altitude of 3353 meters (11,000 feet) mean sea level (MSL) and then released for an unpowered flight. Upon release, the pilot would maneuver the aircraft into a steady-state flight condition. The airspeed was then decreased to the stall speed of about 36 Knots using the center control stick. Just prior to complete stall, the stabilizer control lever was moved back quickly but gently to a preset position of 40, 50, or 60 degrees stabilizer setting depending on the required angle-of-attack. This action caused the angle-of-attack of the aircraft to increase rapidly through the "transition region" of between 15 to 30 degrees to the desired deep stall angle-of-attack. This so-called transition region, is characterized by large asymmetry in the lateral-directional forces and moments (more pronounced for high aspect ratio aircraft) that would cause the SGS 1-36 to enter an undesirable spin or spiral dive.

Once the aircraft was in the deep stall region, the pilot stabilized the aircraft on a trim point for about five seconds and then performed elevator, rudder, and aileron doublet maneuvers. As the next step, handling quality evaluation maneuvers were performed using the elevator, rudder, and ailerons. At an approximate altitude of 2393 meters (7850 feet) MSL or 1676 meters (5500 feet) above ground level (AGL) recovery was initiated by using the stabilator to lower the angle-of-attack to the transition

area. Although the actual angle-of-attack was not displayed in the cockpit, the transition region was sensed by the pilot from the mild tail buffet due to the wing wake. Upon encountering the tail buffet, the stabilator was rapidly moved to zero stabilator deflection position. During recovery 91 to 152 meters (300 to 500 feet) of altitude were lost while the airspeed typically increased from 38 to 55 Knots.

The concept of the Controlled Deep Stall flight is illustrated in Figure 9. Figure 10 depicts the SGS 1-36 in deep stall flight at 50 degrees angle-of-attack.

During initial flight test planning, provisions were made to fly the aircraft at 30, 40, 50, 60, and 70 degrees trailing edge up stabilizer setting with the C.G. at two different positions. Initially, the wind tunnel data had indicated that with the C.G. at about 33% MAC there would be a one-to-one correspondence between the stabilizer setting and the angle-of-attack. However, during the first and second deep stall flights with the horizontal stabilizer at 60 degrees and the center of gravity at 33.1% MAC, the average angle-of-attack was recorded to be 72 degrees. In addition, some unexpected lateral-directional, apparent Dutch-Roll, oscillations were observed. Based on this observation the remaining flights with higher stabilizer setting (70 degrees, with forward and aft center stick positions) were deemed too risky and were consequently cancelled. With the stabilizer setting at 40 degrees

trailing edge up, C.G. position of 28.3% MAC, and elevator control stick fully aft the pilot was not able to maintain the aircraft in the deep stall region for any sustained period of time. In this flight regime the aircraft had a tendency to enter and remain in the transition region. Hence, it was decided not to perform the remaining one flight in the same configuration with the stick fully forward.

During the first deep stall flight of the SGS 1-36 with the angle-of-attack of about 72 degrees, two unexpected phenomena were encountered. Firstly, as soon as the aircraft entered the deep stall flight, the pilot experienced an unusually large, unstable lateral control stick hinge moment. He estimated the force on the center stick to be approximately 25 pounds and indicated that he had difficulty keeping the stick centered using his right hand (he used his left hand to keep the stabilator control lever in the deflected position) since the stick had a tendency to deflect either to the right or to the left. Secondly, as mentioned earlier, in the deep stall flight the aircraft exhibited an unstable lateral-directional oscillation. During the flights that followed it was discovered that the magnitude of the unstable control stick hinge moments and the lateral-directional instabilities were functions of the angle-of-attack. As the angle-of-attack increased so did the magnitudes of the unstable stick hinge moment and the apparent divergent Dutch-Roll

oscillation to a constant limit cycle. This phenomena will be discussed in more detail in the following sections.

Due to rapid aircraft descent in the deep stall region, up to 1372 meters per minute (4500 feet per minute), the pilot had only about 60 to 100 seconds to complete his maneuvers. Because of the limited time available for obtaining flight data and rapidly changing flight conditions, there was only one opportunity to perform each maneuver. Thus maneuvers were practiced on the flight simulator prior to each flight. Post flight analysis of these maneuvers indicated that a doublet or pulse, followed by two to five seconds in which the pilot made no input, was most effective in providing satisfactory stability data. It was also discovered that the range of the angle-of-sideslip calibration was not sufficiently large, which prevented the magnitude of raw side-slip-angles greater than 35 degrees from being recorded.

Chapter 5

WIND TUNNEL TESTS

A low speed wind tunnel investigation was conducted at NASA Langley Research Center's 30 x 60 wind tunnel to determine the static aerodynamic characteristics of a quarter scale model of the modified SGS 1-36 sailplane (Reference 3). For economical reasons, the model used was a low-cost "free-flight" model which limited the wind tunnel's dynamic pressure and hence the Reynolds number. Longitudinal and lateral-directional force tests were conducted over an angle-of-attack range of 0 to 90 degrees and angle-of-sideslip range of +/-10 degrees. Control effectiveness was determined for horizontal stabilizer deflections of 0 to 70 degrees trailing edge up, elevator deflections from +20 to -25 degrees, aileron deflections of 32 degrees up and 12 degrees down, and full rudder deflection of +/-27 degrees. The wind tunnel speed was measured at 12.19 meters per second (40 feet per second) which corresponds to a dynamic pressure of about 85.9 Newton per square meter (1.8 pounds per square foot) and Reynolds number of about 1.8×10^5, based on a chord length of .24 meters (0.8 feet). This low Reynolds number is generally considered to be on the high side of the sub-critical range. Sub-critical Reynolds number data is known to

greatly underpredict the effectiveness of any trailing edge control surfaces.

During the initial wind tunnel test a significant change in the wing dihedral was observed due to extreme wing flexibility. Therefore, a limited second series of tests were conducted with the wings restrained from bending so that a comparison could be made between the two series of tests. The final test results were a combination of the two series of tests. All the wind tunnel data were provided in the aircraft stability axis and were later transformed into body axis for the final comparison with the flight test results.

With regards to the validity of using low Reynolds number wind tunnel data for application to the full scale sailplane, Figure 12 of Reference 4 indicates that the effects of Reynolds number on the longitudinal characteristics of the aircraft are minimal above 30 degrees angle-of-attack. Sincethe the aerodynamic characteristics of the SGS 1-36 in the range of 30 to 75 degrees angle-of-attack were of the prime interest, it was assumed that the final wind tunnel results were reasonable representation of the conditions that would exist at the full scale Reynolds number range of about 1.0×10^6 to 3.0×10^6. The values of C_L obtained from wind tunnel tests were corrected for high Reynolds number of the full scale aircraft based on results of Figure 12.

Chapter 6

COMPUTED AERODYNAMIC STABILITY DERIVATIVES

In the conduct of the SGS 1-36 Controlled Deep Stall Project, a complete set of static and dynamic(rotary) aerodynamic stability derivatives were required for the angle-of-attack range of -5 to 90 degrees, so that a comprehensive comparison could be made between flight test and predicted data. The wind tunnel testing of the SGS 1-36 quarter scale model fulfilled part of the requirement by providing a set of static aerodynamic derivatives. In order to obtain a complete set of rotary derivatives, a decision had to be made as to which technique should be employed to predict these derivatives at such wide range of angles-of-attack. Theory had been well established to estimate the rotary derivatives at low angles-of-attack (-5 to 15 degrees), but there were no techniques available for determining these derivatives at high angles-of-attack range of 20 to 90 degrees. Based on this fact, a decision was made to use a combination of computer programs and computational methodsto obtain the rotary derivatives in the low angles-of-attack, and to develop some new techniques to compute these derivatives in the high angles-of-attack region.

Vortex-Lattice program of Reference 5 was used to compute Cl_p, Cn_r, Cm_q, CN_q, and CY_r in the low angle-of-

attack region of -5 to +15 degrees. This program, an extension of the finite step lifting-line method, assumes steady state, irrotational, inviscid, incompressible, attached flow and uses Prandtl-Glavert similarity rule to model the compressibility effects. In the past, the Vortex-Lattice program has been used extensively at NASA Ames/Dryden and the results indicated a good correlation between derivatives obtained using this program and that of the flight tests. Therefore, it was assumed that acceptable results could be obtained using the Vortex-Lattice program.

The computational method used to determine the values of Cn_p and Cl_r at angles-of-attack of between -5 and +15 degrees were based on the well established, empirical procedures of reference 6.

To obtain results in the high angle-of-attack range of 20 to 90 degrees, an equation was developed to compute the values of Cl_p assuming drag as the only source of aerodynamic force and moment (Appendix C). No other analytical equations were possible to develop without some gross oversimplifications that would have rendered them useless. Therefore, estimations of the remaining rotary derivatives were made purely based on trends exhibited by the available static and dynamic derivatives in this high angle-of-attack region.

In the deep stall flight regime, the parameter CN_q was predicted to behave similar to the calculated Cl_p which

is also a function of the wing's C_N. Given that Cm_q is a function of moment arm l_t (the distance between the wing and the tail quarter cord), and that this moment arm decreases as a function of COS(α) as the angle-of-attack increases, it was assumed that the magnitude of Cm_q would also decrease as a function of COS(α) in the range of 20 to 90 degrees.

The value of CY_r was selected to be constant through -5 to 90 degrees angle-of-attack since the Vortex-Lattice computation of this parameter at low angles-of-attack region had resulted in a constant value.

The parameters Cn_p and Cl_r were presumed to decrease with angle-of-attack similar to the decrease in $Cl_{\delta a}$, aileron control effectiveness (a wing parameter), once past the stall angle-of-attack. Similarly, Cn_r was assumed to decrease with angle-of-attack just as $Cn_{\delta r}$, rudder control effectiveness (vertical tail parameter), decreased above 20 degrees angle-of-attack.

It is important to notice that the damping derivatives obtained using the Vortex-lattice program were pure rotary derivatives without the inclusion of the translational acceleration derivatives. In general, the damping derivatives obtained from flight or oscillatory wind tunnel tests are a combination of the rotary and translational acceleration derivatives. As an example the two parameters Cm_q and $Cm_{\dot{\alpha}}$ could not be individually determined from flight data, therefore the combination of

the two is commonly referred to as Cm_q, its rotary derivative name. In this report all flight derivatives are called only by their rotary derivative name.

Ordinarily, during the damping derivatives calculations, the translational acceleration derivatives are neglected because of their relatively small magnitude and lack of readily available techniques to compute them. However, since translational acceleration derivatives $Cm_{\dot{\alpha}}$ and $Cn_{\dot{\beta}}$ often have significant magnitude, it is possible for the predictions of $Cm_q+Cm_{\dot{\alpha}}$ and $Cn_r+Cn_{\dot{\beta}}$ to be lower than that of the actual flight due to under estimation of $Cm_{\dot{\alpha}}$ and $Cn_{\dot{\beta}}$. In predicting the values of $Cm_q+Cm_{\dot{\alpha}}$ and $Cn_r+Cn_{\dot{\beta}}$, the Vortex-Lattice program was used to determine the magnitude of Cm_q and Cn_r. Based on established guide lines, the magnitudes of $Cm_{\dot{\alpha}}$ and $Cn_{\dot{\beta}}$ were set equal to 40% of the values obtained for Cm_q and Cn_r respectively.

A complete set of wind tunnel determined static forces and moments as well as the predicted rotary aerodynamic stability derivatives versus angle-of-attack are presented in the appendix A.

Chapter 7

DATA ANALYSIS

To determine the longitudinal and lateral-directional aerodynamic stability derivatives from the recorded flight test time histories a digital computer program was used. This Fortran program, the Modified Maximum Likelihood Estimation (MMLE) of Reference 7 is a generalized dynamic analysis program which includes specific provisions applicable to aircraft dynamic analysis. The MMLE program employs a modified Newton-Raphson iteration technique to minimize the error between the various flight recorded time responses and the corresponding responses of the mathematical model of the aircraft (Appendix B). As an example, the flight recorded time histories of Flight 7 are presented in Figure 13.

The aircraft mathematical model is represented by two independent sets of three degree-of-freedom linearized differential equations of motion with the stability derivatives as the unknown coefficients. These two sets of equations are known as the longitudinal and lateral-directional equations of motion. The longitudinal equations are excited by flight measured elevator deflection and the lateral-directional equations by flight measured aileron and rudder deflections. The MMLE program uses the predicted

static and rotary derivative set as the starting coefficient values to solve either the longitudinal or lateral-directional equations of motion and produce a system response time history. The resulting time responses and the corresponding flight time histories are then compared to determine the difference between them that constitutes the error. This error is represented by the error vector,

$$\Delta Y = [\, \Delta \dot{p}, \Delta \dot{r}, \Delta p, \Delta r, \Delta \beta, \Delta a_y \,]^T$$

where the objective is then to minimize ΔY in an optimal fashion using the cost functional

$$J = \int_{\bullet}^{T} (\Delta Y)^T W \Delta Y \, dt$$

where W is a weight matrix reflecting the relative confidence in the instrument measurements. To accomplish this task the Newton-Raphson iteration method was selected and modified to provide successful minimization. Once the error has been minimized the corresponding values of the coefficients are selected as the best estimation of the aircraft's aerodynamic stability and control derivatives. Figures 14 and 15 represent examples of MMLE produced and flight determined lateral-directional and longitudinal time histories for Flights 7 and 13.

A measure of the accuracy of these estimated derivatives is provided in the form of the Cramèr-Rao bound. The smaller the Cramèr-Rao bound, the more confidence that can be placed in the estimated values of the derivatives. An evaluation of the use and accuracy of the Cramèr-Rao bound

is given in Reference 8. Ordinarily the Cramèr-Rao bound produced by MMLE tends to indicate a high degree of accuracy for the estimated derivatives, where in reality the accuracies are lower due to aerodynamic modeling errors (i.e. no consideration for non-linearities), poorly conditioned maneuvers, presence of state noise, and inevitable sensor errors (despite provisions within the MMLE to account for some of these modeling errors). To compensate for these anomalies the resulting Cramèr-Rao bounds were multiplied by a factor of 3 based on previous experience that have shown this to produce a more realistic representation of the error bound .

The MMLE program contains several options that facilitates the convergence of the initial values to a final derivative set. For stable systems, the program normally converges in 6 or 7 iterations, but in some instances where the dynamic response may be unstable or non-linear, the program would not easily converge without the use of the "A priori" option. This option, allowed the starting set of derivatives to be weighted, which tended to hold the derivatives near their starting values if no information about them was contained in the maneuver. Early in the flight program, wind tunnel and the computed predictions were used as the starting values. However, as different trends in the data developed, previously obtained flight-determined derivatives were used. Since a high "a priori" Value during complete iteration process tended to

produce unrealistic results, the weighing was removed after 4 iterations so that the derivatives could change freely in the remaining 4 or 5 iterations as they converged to a final set of values. Because in the high angles-of-attack regions a small banking of the aircraft translated into some unrealisticaly high sideslip angles, the flight recorded angle-of-sideslip was multiplied by the cosine of angle-of-attack to arrive at the corrected sideslip angle.

To gain insight into the lateral-directional instabilities observed during flights at high angles-of-attack, the DIGIKON computer program of Reference 9 was used to conduct a simple open loop analysis of the aircraft dynamics using the results from Flight 7. DIGIKON represents an advanced state-of-the-art tool for modeling and analyzing digital and continous flight control systems. It uses the modern state-space approach for modeling the aircraft and its various flight control systems. To facilitate the aircraft modeling in the state-space form, an interactive interface program between the user and DIGIKON was created. This interface program, ACST, accepts the non-dimensional aerodynamic stability and control derivatives produced by MMLE, along with their corresponding flight condition and mass properties, to generate the dimensionalized, linear, differential equations of motion of the aircraft in the state-space format, as expected by DIGIKON. Once the aircraft is modeled, DIGIKON allows the user to interactively perform time domain or frequency

domain analysis for a given input (control surface deflection). For this report only two S-plane Root-Locus plots were generated. One plot represents the aircraft response if the pilot (assumed to behave as a pure gain) tries to control the bank angle using his ailerons (Figure 19), and the second plot, if he controls the sideslip angle using his rudder (Figure 20).

Chapter 8

RESULTS AND DISCUSSION

In the past, dynamic response and handling qualities of aircraft at very high angles-of-attack have seldom been investigated. The NASA SGS 1-36 Controlled Deep Stall project has, for the first time, provided limited data in this extreme angles-of-attack region for a full-scale, piloted aircraft. The analysis presented in this section is the first qualitative investigation of the phenomenon at high Reynolds numbers. Hence, the preliminary nature of the presented analysis is herein emphasized.

Flight 7 has been selected as a case example to represent the results from the majority of the 20 flights that were conducted in the deep stall region. For this reason, the data obtained from flight 7 is analyzed in detail in order to provide some explanation for the observed flight characteristics of the aircraft in this flight regime.

Figure 13 is the presentation of the complete deep stall time histories for flight 7. An inspection of these time responses reveals the ease with which the pilot was able to enter and exit the deep stall flight. As the aircraft enters into the deep stall (the average angle-of

attack of about 65 degrees), the dynamic pressure decreases to about 239 N/m^2 (5 psf). This low dynamic pressure eliminates any risk of possible structural damage to the airframe. The vertical descent rate increases to a value of 1219 meters per minute or 4500 Ft/Min (plotted data are truncated above 1219 m/min or 4000 Ft/min of vertical velocity due to sensor limitations). The elevator effectiveness is shown to diminish drastically at this high angle- of-attack, but the lack of any significant longitudinal oscillation indicates a damped pitch characteristic. One of the most important observations to be made is the lateral-directional oscillation that is signified by the bank and sideslip angles oscillations at the rate of 1.39 rad/sec. Initially, the magnitude of the oscillations increases to a constant limit cycle as the aircraft enters the deep stall, with the angle-of-attack of about 65 degree, but decreases as the pilot decreases the angle-of-attack to about 50 degrees using his stabilator. The oscillations increase again as the angle-of-attack is increased back to 65 degrees. This phenomenon indicates a direct correlation between the angle-of-attack and the magnitude of the lateral-directional oscillation for flights in this high angle-of-attack regime.

The attitude time history plot points out a mostly level aircraft all through the deep stall portion of the flight. The pitch rate time history denotes a small, higher frequency oscillation (3.14 rad/sec), but lower magnitude

(average of 14 deg/sec) than that of the roll and yaw rates (1.4 rad/sec with average magnitude of 45 and 17 deg/sec respectively). The maximum normal acceleration of about 1.9 G is encountered only during the recovery phase, where as during the deep stall flight the normal acceleration remains at 1 G.

The apparent independence of the bank and sideslip angles from the aileron and rudder deflections connotes a very low aileron and rudder effectiveness at extreme angles-of-attack. As indicated in the previous sections the plotted sideslip angle time history is truncated due to limited calibration range at high angles-of-attack.

Figure 14 is the MMLE computed lateral-directional time histories for a given maneuver of Flight 7 as compared to the flight determined time histories of the same flight. Three points could be made regarding these plots. First, the aileron and rudder doublet maneuvers are quite good despite the uncontrolled lateral-directional oscillations. Second, the MMLE computed time responses match that of the flight quite well. But the matches during the aileron and rudder deflection time intervals are not as good. This indicates that the final MMLE output may not provide a realistic control effectiveness values for this maneuver. Third, since the sideslip angle was truncated due to calibration limitations, a low weight was imposed on this parameter during the MMLE iterations to reduce its ill effects on the estimated derivatives. It should be noted

that the lateral acceleration data provide the same information as that of sideslip angle. Therefore, MMLE is not deprived of any significant information. The lateral-directional time history matches presented in Figure 14 are typical of the other matches produced by MMLE for the remaining 19 flights at high angles-of-attack.

The longitudinal flight determined and MMLE computed time histories of Flight 13 are compared in Figure 15. This figure is an example of a typical MMLE match for conventional low angle-of-attack flight (about 2.5 degrees). The angle-of-attack time response, following the elevator doublet maneuvers, implies an over damped longitudinal dynamic characteristic for the aircraft in this flight regime.

In Figure 16, the flight envelope of the SGS 1-36 is presented in the form of flight determined trim data (elevator deflection versus angle-of-attack), at C.G. positions of 33.1% and 28.4% MAC, and four stabilator settings of 0, 40, 50, and 60 degrees. In addition, the normal and controlled deep stall flight regime as well as transition and uncontrolled deep stall flight regions are clearly marked by dashed line. However, it should be noted that the dashed lines only approximate the border between the different regions.

One of the significant characteristics of the trim plots is that in the normal flight regime the slope of the elevator deflection versus angle-of-attack decreases as the

center of gravity is shifted from 28.4% to 33.1% MAC, in a conventional manner. Where as, in the deep stall region no significant change of slope is noticed. Instead, the plotted trim data exhibit a shift to the right following the C.G. shift to the aft.

The final MMLE estimated and predicted longitudinal stability and control derivatives of the NASA SGS 1-36 sailplane are presented in Figure 17. The lateral-directional stability derivatives are plotted in Figure 18. The presented MMLE estimates, consist of results obtained from the 20 flights of the vehicle at the two C.G. positions of 28.4% and 33.1% MAC, which have been corrected to 40% MAC for comparison to the wind tunnel and the estimated aerodynamic derivatives. Those MMLE estimates with high Cramer-Rao bound are eliminated from the plots according to the tolerances set forth in Table 5.

The flight determined values of the Cm_{α} and Cm_{q} (Figure 17) disclose a more stable longitudinal characteristic for the aircraft than that of the predicted, in the deep stall flight regime. On the other hand, the conventional flight regime comparison indicates that the damping derivative Cm_{q}, was not predicted with accuracy using the Vortex-Lattice program. The plot of CN_{α} versus the angle of attack reveals a higher than predicted normal force in the deep stall region. As denoted by Figure 17, the elevator effectiveness decreases sharply as the angle-of-attack is increased to 72 degrees, but the

negative values of $CN_{\delta e}$ might be due to the fact that elevator effect could not be modeled separately, and its value is a combination of elevator and stabilator effectiveness (stabilator would deflect about 2 degrees due to aerodynamic moment produced by elevator deflection).

The lateral-directional static and dynamic stability and control characteristics of the NASA SGS 1-36 sailplane as estimated by MMLE are compared to that of the predictions in Figure 18. The parameter CY_{β}, displays lower than predicted magnitudes in the deep stall as well as conventional flight regime. In the deep stall this parameter displaysa magnitude approximately equal to that of the normal flight regime. Since in the conventional flight regime the bulk of the side force due to side-slip-angle is created by the vertical stabilizer, and that in the deep stall the air flow over the vertical stabilizer is reduced markedly, it would therefore be reasonable to assume that the bulk of the side force in the deep stall flight regime is created by the fuselage.

It is important to notice that the parameters $CY_{\delta r}$ and $Cl_{\delta r}$ do not contain as many flight determined data points as the rest of the parameters. This occurrence can be attributed to the lack of information contained in the flight data about these parameters which when supplied to MMLE results in high Cramer-Rao bound. A Cramer-Rao bound greater than the predetermined tolerances (Table 5), will

result in the omission of some of those derivatives from the presented plots.

Although the quarter scaled wind tunnel model used the same amount of differential aileron deflection as the full scaled aircraft, the examination of $CY_{\delta a}$ at low angles-of-attack points out to higher wind tunnel predication than the MMLE produced estimates (differential aileron deflection can reduce or eliminate the magnitude of this parameter). The parameter $CY_{\delta a}$ is, also, a weak parameter, that is to say, the deep stall and low angles values for this parameter could not accurately be estimated using MMLE.

The undesirable, lower than predicted values for Cl_{β} in the deep stall region, is perhaps due to the Reynolds number difference between the wind tunnel model and the actual aircraft. A combination of low MMLE estimated values of this effective dihedral parameter and Cn_{β}, a primary directional stability parameter, may be one the major contributors to the lateral-directional instability observed in the high angles-of-attack flights. The low angles estimation of Cn_{β} corresponds well with the prediction, except the negative value of one of the maneuvers, that should be regarded as unrealistic.

The plot of $Cl_{\delta a}$ versus angle-of-attack, follows the wind tunnel predicted trend quit accurately, except with lower magnitudes in the conventional flight regime. The value of this parameter approaches zero as the angle-of-

attack is increased to 72 degrees, which indicates lack of any significant aileron effectiveness in the extreme angles-of-attack, as expected.

The tendency of the $Cn_{\delta a}$ to change from a proverse, favorable yaw characteristic at low angles-of-attack to adverse undesirable yaw characteristics in the high angles-of-attack region is emphasized in Figure 18. The favorable, proverse, yaw characteristics of the aircraft in the conventionalflightregime is, primarily, due to the large differential aileron deflection of this high aspect ratio vehicle. This desirable handling quality diminishes rapidly at higher angles when the completely separated flow eliminates any aileron effectiveness.

A higher than expected rudder effectiveness is displayed at lower angles, and with lesser degree in the higher angles-of-attack by the plot of $Cn_{\delta r}$. The flight determined values of Cl_p in the conventional flight regime nicely follows the trend set forth by the prediction but with lower magnitude. On the other hand, as the aircraft enters the deep stall region the value of this primary roll damping derivative rapidly approaches zero. The same observation holds true for Cl_r, the primary yaw damping derivative. A combination of near zero value of Cl_p and Cl_r is the principal cause of the lateral-directional oscillation at angles-of-attack higher than 60 degrees. Although, the low angles MMLE estimations of Cn_p exhibits a definite, precise trend, the larger than predicted negative values

for this parameter at low angles-of-attack, is an undesirable handling quality for the aircraft.

To gain further insight into the lateral-directional dynamic response of the SGS 1-36 in the deep stall region, two S-plane root locus plots of $\phi/_{\delta a}$ and $\beta/_{\delta r}$ transfer functions for Flight 7 are presented in Figures 19 and 20. Because most pilots use visual cues to fly aircraft, and that the bank and sideslip angles are two of the strongest visual cues, $\phi/_{\delta a}$ and $\beta/_{\delta r}$ transfer functions were selected for the open loop analysis of the vehicle, to obtain the closed loop dynamic characteristics of the aircraft (the pilot is assumed to be pure gain). In Figure 19, one of the interesting dynamic characteristics of the aircraft at this angle-of-attack (65 degrees) is the unstable, oscillatory Dutch-roll mode of the sailplane. This mode is signified by a pair of imaginary poles of the aircraft's characteristics equation oscillating at a frequency of 1.34 rad/sec. The near zero damping of Dutch-roll mode (.015), along with the low damping of the oscillatory roll-spiral mode (.91) might explain the observed flight oscillations. It is important to notice that the flight-determined dutch-roll oscillation frequency of 1.39 rad/sec is very close to the dutch-roll frequency of 1.34 rad/sec computed by DIGIKON, and plotted in Figure 19. One of the zeros of the of the $\phi/_{\delta a}$ transfer function is shown to be in the right hand plane which is considered unconventional. But this characteristic does not appear to contribute to any possible instability, because

as indicated by the gain versus real axis plot of Figure 19, a very large pilot gain (about 3.5) is required to drive the roll-spiral mode unstable (pilot gain is normally between .5 and 1). The Dutch-roll mode, on the other hand, has a tendency to become more stable as the pilot's gain is increase to a value of 1. A pilot gain of 1 can easily be achieved at such high angle-of-attack due to low aerodynamic damping and control surface effectiveness.

Although the transfer function β/δ_r is considered to be less important than ϕ/δ_a, a root locus analysis of it may help in presenting a clearer picture of the over-all dynamic response of the aircraft in the high angle-of-attack deep stall flight region. Figure 20 contains the S-plane root locus plot of β/δ_r for Flight 7. As indicated by Figure 20, the coupled roll-spiral mode has a tendency to become unstable if the pilot makes any effort to control the sideslip angle using his rudder. In this case any increase in the gain tends to stabilize the dutch-roll mode in a desirable manner.

Chapter 9

CONCLUDING REMARKS

A flight investigation of the controlled deep stall concept was conducted using a full scaled, modified, piloted SGS 1-36 sailplane, at angles-of-attack of between -5 and 75 degrees. Despite the pioneering nature of this investigation, all of the primary objectives of the project were achieved, and for the first time a complete set of flight determined dynamic stability and control derivatives was obtained for an aircraft at such extreme angles-of-attack.

The aircraft was flown successfully in the deep stall region using large in-flight deflection of the all-movable horizontal stabilizer. This proved to be a viable technique for longitudinally controlling the aircraft in the deep stall flight regime. The NASA SGS 1-36 demonstrated excellent longitudinal and lateral-directional stability and control characteristics in the angle-of-attack range of 30 to 50 degrees, but displayed some undesirable lateral-directional instabilities in the form of unstable Dutch-Roll oscillation above 55 degrees angle-of-attack. The magnitude of the oscillation appeared to be a function of angle-of-attack, and became more pronounced as the angle-of-attack increased.

In order to predict the dynamic behavior of the aircraft before the first deep stall flight, new techniques had to be developed for calculating the rotary derivatives at extreme angles-of-attack. Post flight comparison of the predicted and the flight determined rotary derivatives, showed some of these techniques to be quite good while others proved inadequate. The comparison of static force and moment derivatives with that of the wind tunnel tests indicated some discrepancies in the low as well as the high angles-of-attack regions, which could be attributed to the Reynolds number difference between the full scale and the quarter scale wind tunnel model.

The research of the deep stall phenomenon is in its infancy. The present investigation has only scratched the surface in revealing the handling qualities and dynamic responses of aircraft in the deep stall flight regime. And more work is left to be done to gain more understanding of different phenomenon observed during the SGS 1-36 flights. the following is a list of other possible areas were more research can take place.

1) A more detailed analysis of the data obtained from the present research could be conducted to provide more concrete evidence as to the causes of the unstable lateral-directional behavior exhibited by the aircraft at very high angles-of-attack.

2) Detailed investigation of the separated flow through further test flights of the SGS 1-36 with the nose

boom removed to determine the effects of the vortesis shed by the nose boom on the aircraft dynamics in deep stall regions.

3) Spin testing of the SGS 1-36 in determining the possible spin recovery techniques using the in-flight deflection of the horizontal stabilator.

REFERENCES

1. Goldberg, Carl : Bring Them Down Safely. Model Airplane News, September 1943.

2. Millicer, Henry : The Deep Stall of Sailplanes. Technical Soaring, Vol. 5,No. 2, December 1978, PP. 35.

3. Paulson, John W. : Low Speed Wind Tunnel Investigation of a .25-Scale Model Similar to the Schwiezer SGS 1-36 Sprite Sailplane. NASA TR D-086, July 1983.

4. Bihrle Associates : Static Aerodynamic Characteristics of a Typical Single Engine, Low Wing General Aviation Design for An Angle of Attack Range of -8 to 90 Degrees. NASA CR-2971. July 1978.

5. Margason, Richard; Lamar, John : Vortex-Lattice Fortran Program for Estimating Subsonic Aerodynamic Characteristics of Complex Planforms. NASA TN D-6142, February 1971.

6. Smetana, Frederick O.; Summey, Delbert C.; Johnson, Donald w.: Riding and Handling Qualities of Light Aircraft- a Review and Analysis. NASA CR-1975. March 1977.

7. Maine, Richard E.; Illif, Kenneth W. : User's Manual for MMLE3, a General Fortran Program for Maximum Likelihood Parameter Estimation. NASA TP-1563. November 1980.

8. Maine, Richard E.; Illif, Kenneth W. : Estimation of Accuracy of Dynamic Flight-Determined Coefficients. AIAA Paper 80-0171, January 1980.

9. Mahesh, K. J.; Konar, F. A.; Ward D. M.: Interactive Flight Control System Analysis Program, Volume II, DIGIKON IV user's Reference Manual. NASA CR NASI-/6483, December, 1982.

TABLE 1.- PHYSICAL CHARACTERISTICS OF THE NASA SGS 1-36 VEHICLE

Total height, m (ft)	1.50 (4.92)
Total length, m (ft)	7.27 (23.86)
Wing -	
Reference & actual planform area, m^2 (ft^2)	13.08 (140.80)
Reference & actual span, m (ft)	14.07 (46.17)
Mean Aerodynamic Cord, m (ft)	0.97 (3.19)
Reference cord, m (ft)	1.00 (3.28)
Root cord, m (ft)	1.28 (4.20)
Tip cord, m (ft)	0.58 (1.89)
Taper ratio	0.451
Aspect ratio	15.15
Incidence at the root, deg	1
Incidence at the tip, deg	0.065
Sweep angle, deg	0
Dihedral angle, deg	4
Airfoil section at the root	FX 61-163
Airfoil section at the tip	FX 60-126
Horizontal tail -	
Planform area, m^2 (ft^2)	1.23 (13.2)
Span, m (ft)	2.41 (7.92)
Average cord, m (ft)	0.51 (1.67)
Root cord, m (ft)	0.56 (1.83)
Aspect ratio	4.76
Leading edge sweep angle, deg	5
Dihedral angle, deg	0
Stabilator range, deg	3 TEU/76 TED
Airfoil section	NACA 64-012
Vertical tail -	
Planform area, m^2 (ft^2)	0.85 (9.10)
Span, m (ft)	1.23 (4.04)
Average cord, m (ft)	0.69 (2.25)
Root cord, m (ft)	0.80 (2.64)
Aspect ratio	1.8
Leading edge sweep angle, deg	27
Airfoil section	NACA 64-012

TABLE 2.- PHYSICAL CHARACTERISTICS OF THE PRIMARY CONTROL SURFACES

Ailerons -	
Total planform area (both wings), m^2 (ft^2)	1.01 (10.90)
Span, m (ft)	2.53 (8.30)
Root cord, m (ft)	0.56 (1.84)
Tip cord, m (ft)	0.39 (1.29)
Average cord, m (ft)	0.40 (1.31)
Hinge line, % average cord	72
Range, deg	12 Up/32 Down
Elevator -	
Total planform area, m^2 (ft^2)	0.42 (4.48)
Root cord, m (ft)	0.23 (0.74)
Tip cord, m (ft)	0.17 (0.56)
Range, deg	20 Up/10 Down
Rudder -	
Planform area, m^2 (ft^2)	0.44 (4.72)
Span, m (ft)	1.13 (3.70)
Root cord, m (ft)	0.42 (1.39)
Tip cord, m (ft)	0.30 (0.97)
Average cord, m (ft)	0.39 (1.28)
Hinge line sweep angle, deg	8
Range, deg	30 Lft/30 Rgt

TABLE 3.- MASS PROPERTIES OF THE NASA SGS 1-36

Masses -	
Empty weight, N (lbs)	3002.4 (675.0)
Useful load, N (lbs)	1089.8 (245.0)
Maximum gross weight, N (lbs)	4092.2 (920.0)
Inertias -	
Long. center of gravity, % MAC	33.4
Measurement weight, N (lbs)	3883.1 (873.3)
Ixx, Kg-m2 (slug-ft2)	1374.9 (1014.4)
Iyy, Kg-m2 (slug-ft2)	869.3 (641.3)
Izz, Kg-m2 (slug-ft2)	2213.5 (1633.0)
Ixz, Kg-m2 (slug-ft2)	67.0 (49.4)

TABLE 4.- SELECTED INSTRUMENTATION RANGE AND ACCURACY FOR THE NASA SGS 1-36 VEHICLE

Parameter Description	Range	Resolution (Bit/unit)	Accuracy
Angle of attack, deg	-10 , 90	0.1193	0.5
Angle of sideslip, deg	-30 , 30	0.0717	0.2
Pitch attitude, deg	-42 , 42	0.0822	0.25
Bank angle, deg	-90 , 90	0.1869	0.54
Elevator deflection, deg	-25 , 25	0.0439	1.60
Stabilizer deflection, deg	0 , 100	0.0597	2.10
Aileron deflection, deg	-50 , 50	0.0886	4.60
Rudder deflection, deg	-50 , 50	0.0606	3.60
Roll rate, deg/sec	-60 , 60	0.1171	0.84
Pitch rate, deg/sec	-50 , 50	0.0864	1.30
Yaw rate, deg/sec	-50 , 50	0.0870	0.90
Long. acceleration, g	-0.5 , 0.5	0.0012	0.001
Lateral acceleration, g	-0.5 , 0.5	0.0017	0.002
Normal acceleration, g	-1.0 , 4.0	0.0047	0.002
Static pressure, hN/m^2	587.9 , 936.7	0.8700	4.19
Static pressure, lbs/ft^2	1232.0 , 1963.0	1.8288	8.77
Dynamic pressure, hN/m^2	0.0 , 16.7	0.0200	0.02
Dynamic pressure, lbs/ft^2	0.0 , 35.0	0.0362	0.04
Static pres. rate, m/min	-914.4 , 914.4	1.8400	1.83
Static pres. rate, ft/min	-3000 , 3000	6.0460	6.00

TABLE 5.- MAXIMUM CRAMER-RAO BOUND TOLERANCES FOR PLOTTED DATA INCLUDING A SCALE FACTOR OF 3

Parameter	±Tolerance
CM_{α}	0.002700
CM_{q}	4.000000
$CM_{\delta e}$	0.001200
$CN_{\delta e}$	0.003000
CN_{α}	0.013000
Cl_{β}	0.000100
Cn_{β}	0.000400
$Cl_{\delta a}$	0.000130
$Cn_{\delta a}$	0.000028
$Cl_{\delta r}$	0.000022
$Cn_{\delta r}$	0.000018
Cl_{p}	0.015000
Cl_{r}	0.013000
Cn_{p}	0.015000
Cn_{r}	0.010000
CY_{β}	0.000800
$CY_{\delta r}$	0.000500
$CY_{\delta a}$	0.000400

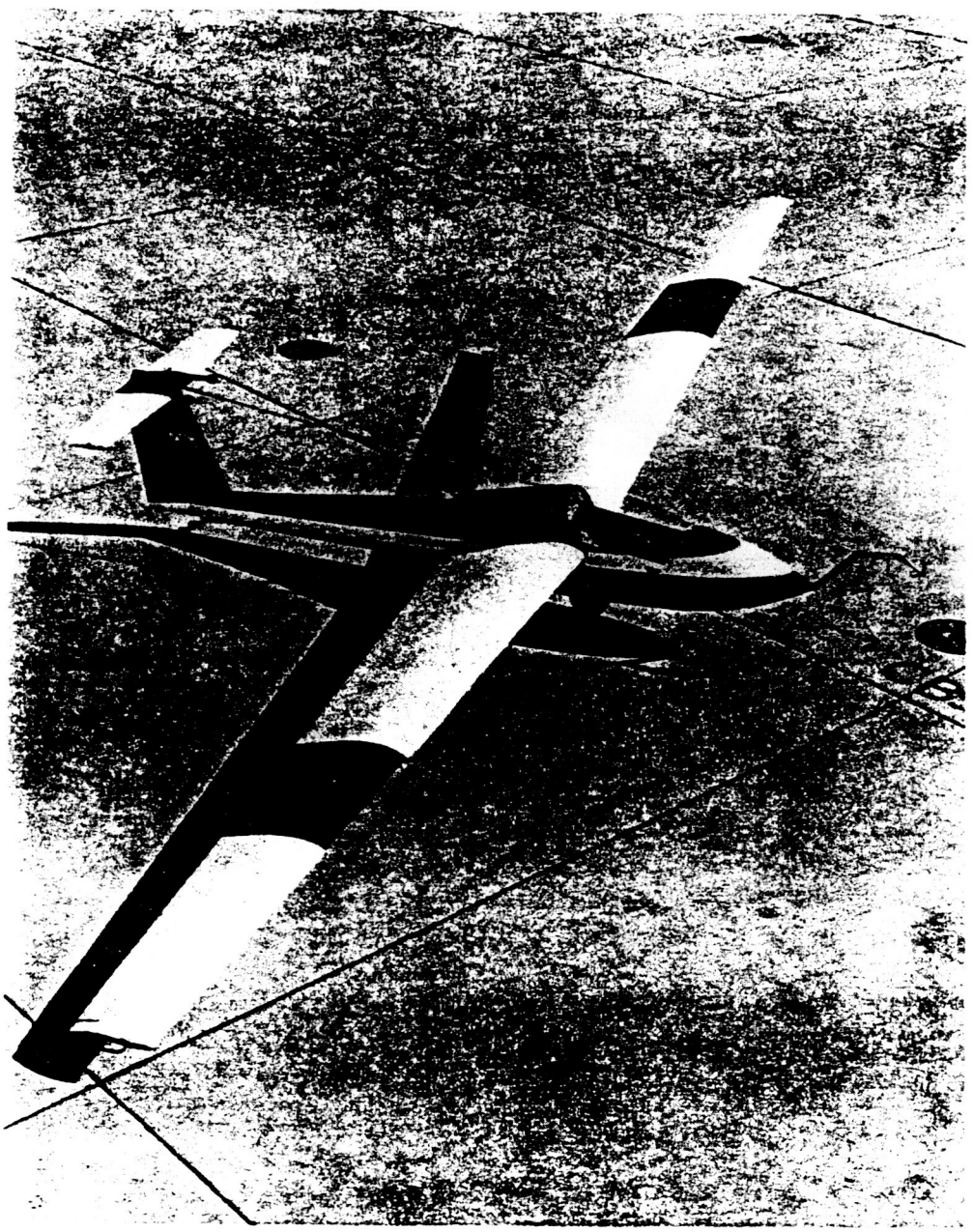

Figure 1: Full scale modified NASA SGS1-36.

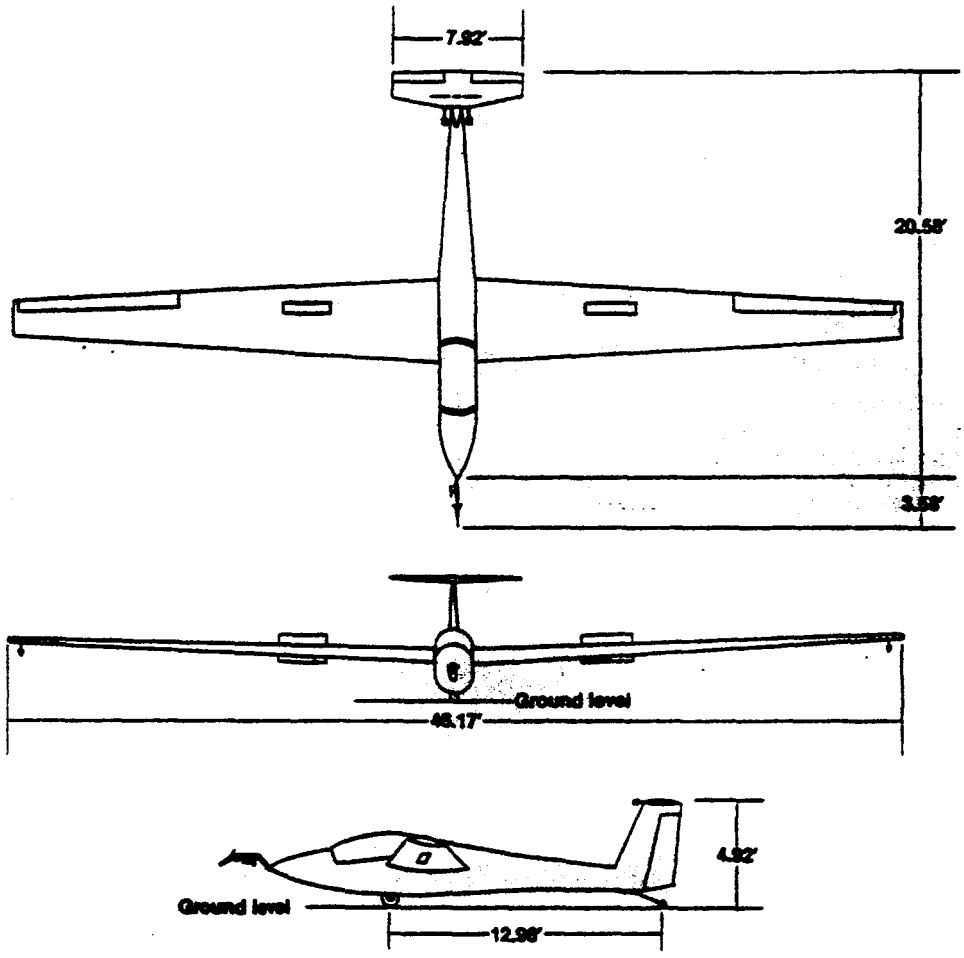

Figure 2: SGS1-36 controlled deep stall

Figure 3: SGS1-36 horizontal stabilizer at 60° trailing edge up position (full deflection).

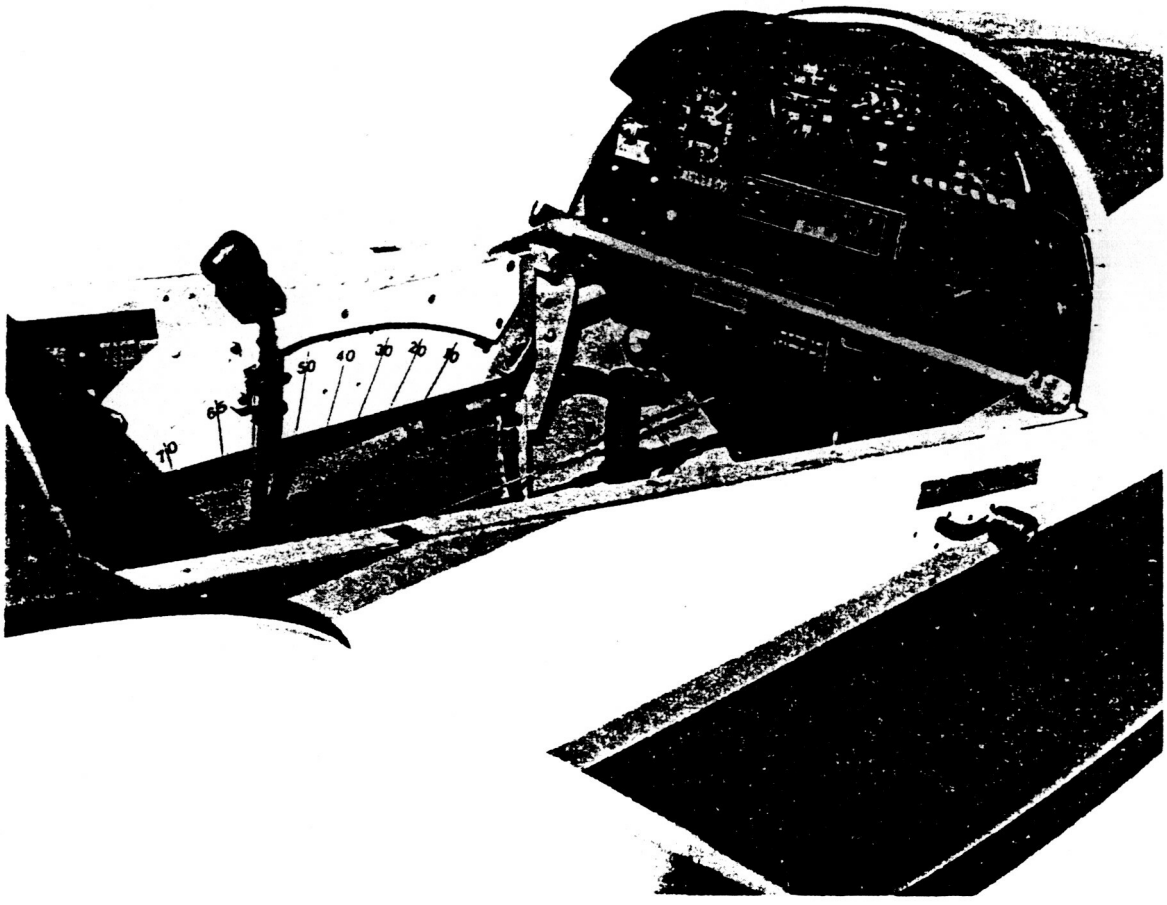

Figure 4: Stabilator control lever positioned for 60° stabilator deflection.

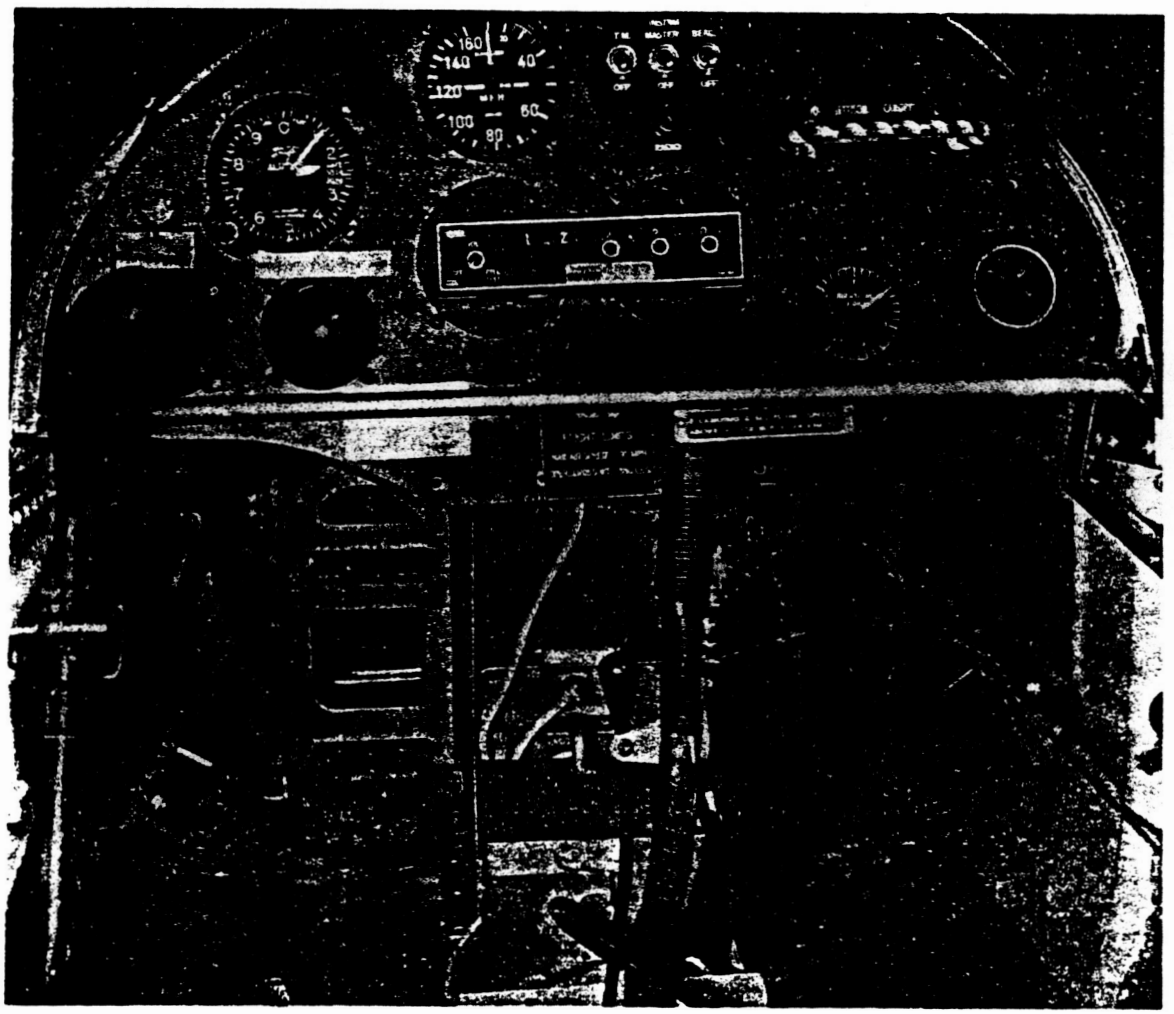

Figure 5: SGS1-36 instrument panel with the automatic canopy ejection control handle.

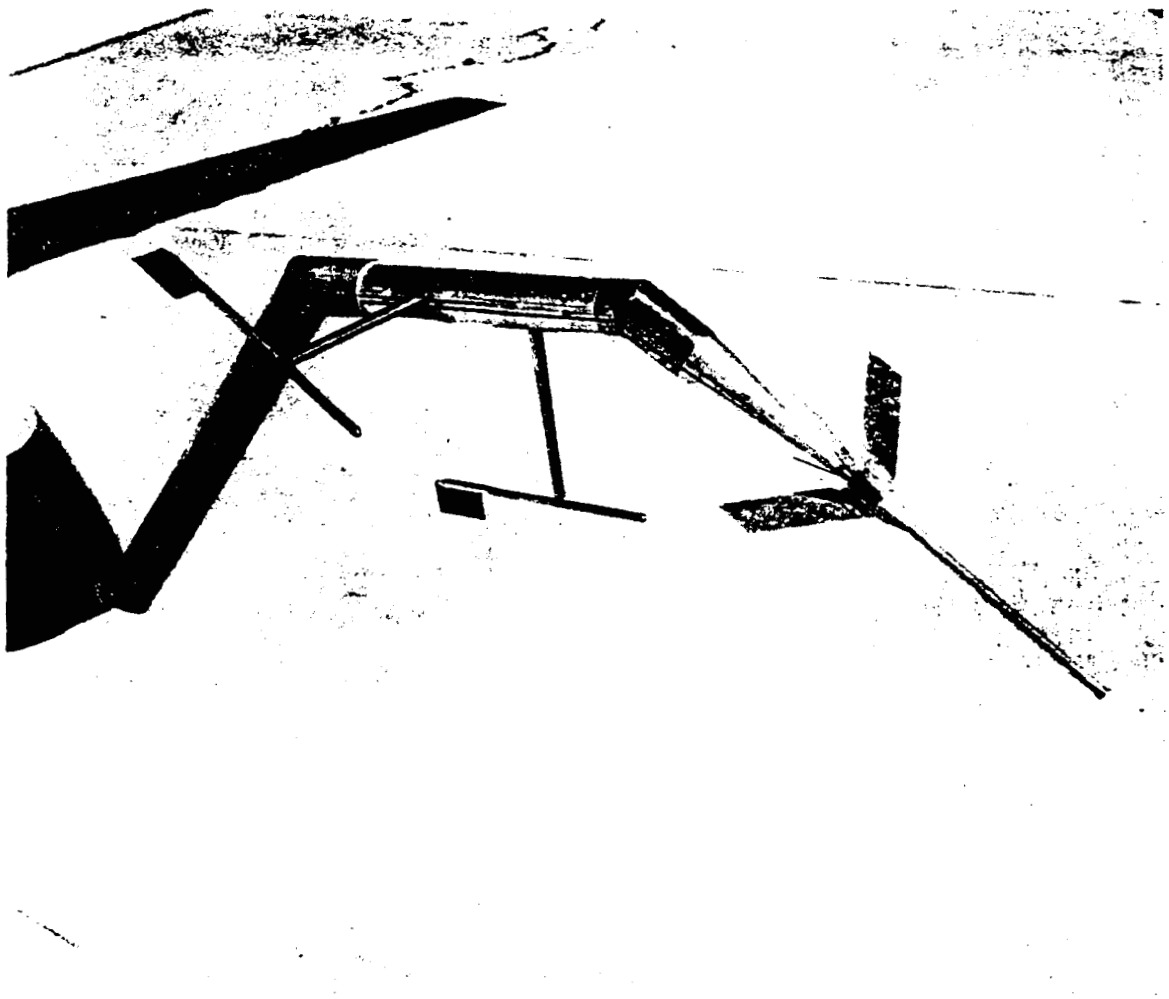

Figure 6: SGS1-36 nose cone with the boom installed.

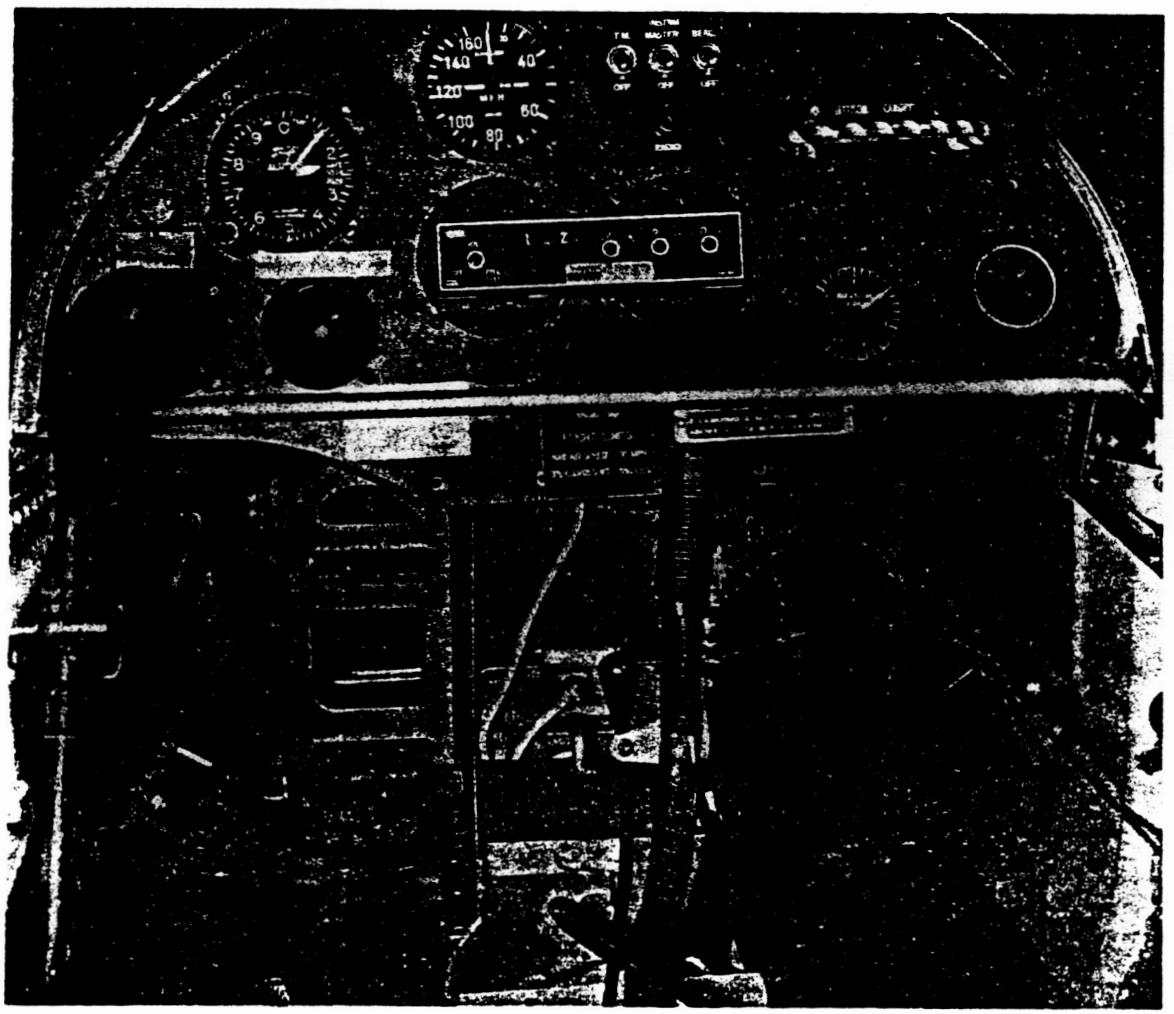

Figure 5: SGS1-36 instrument panel with the automatic canopy ejection control handle.

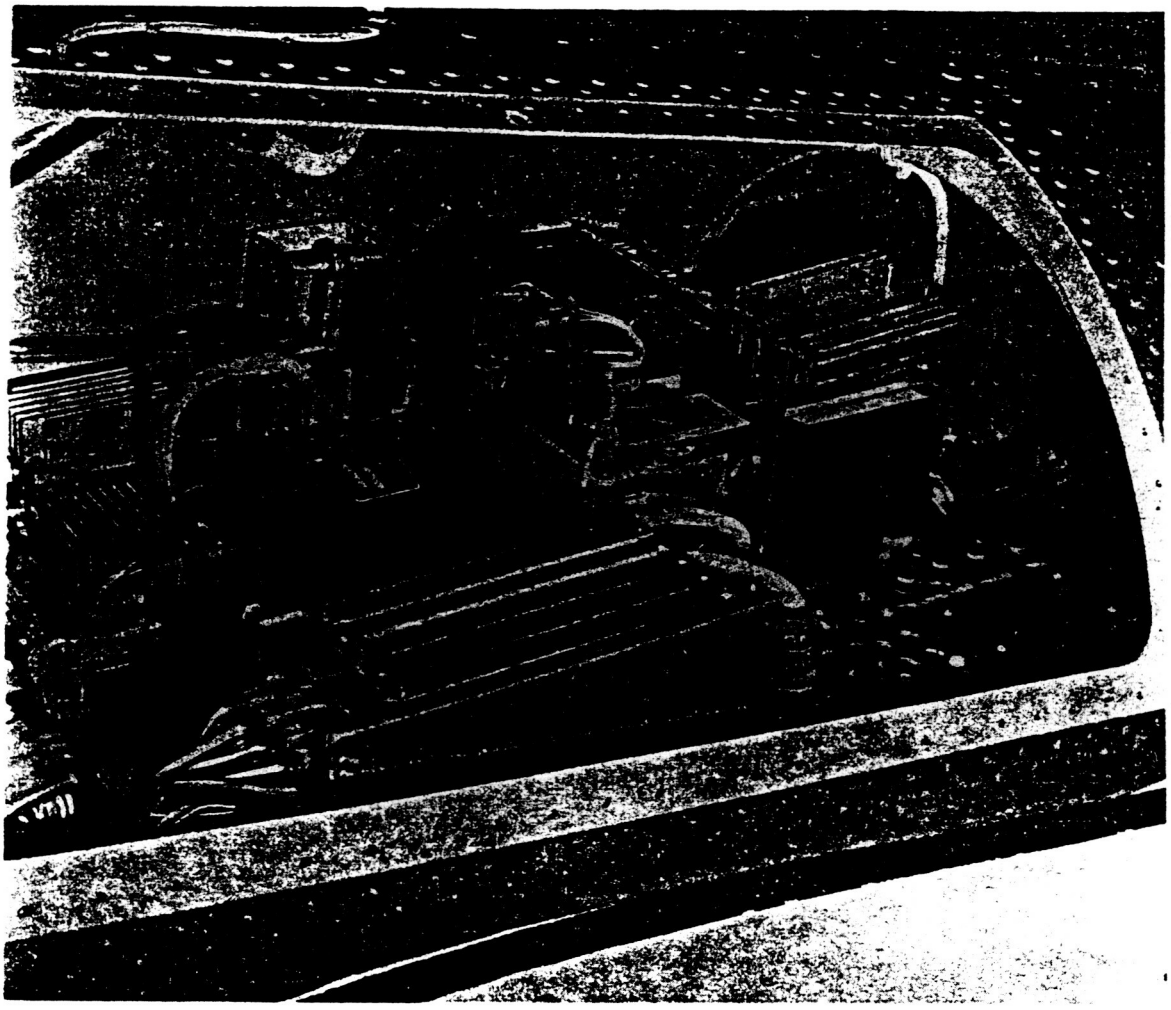

Figure 7: The onboard data acquisition system.

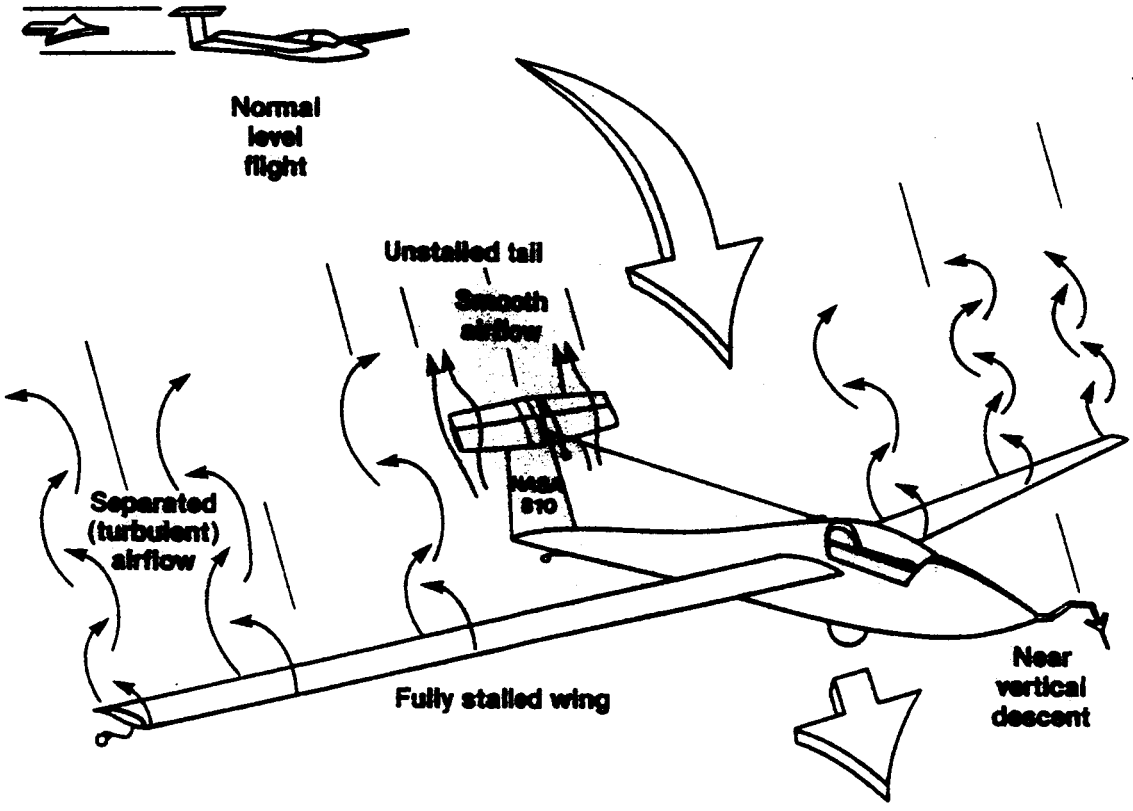

Figure 9: Basic controlled deep stall concept

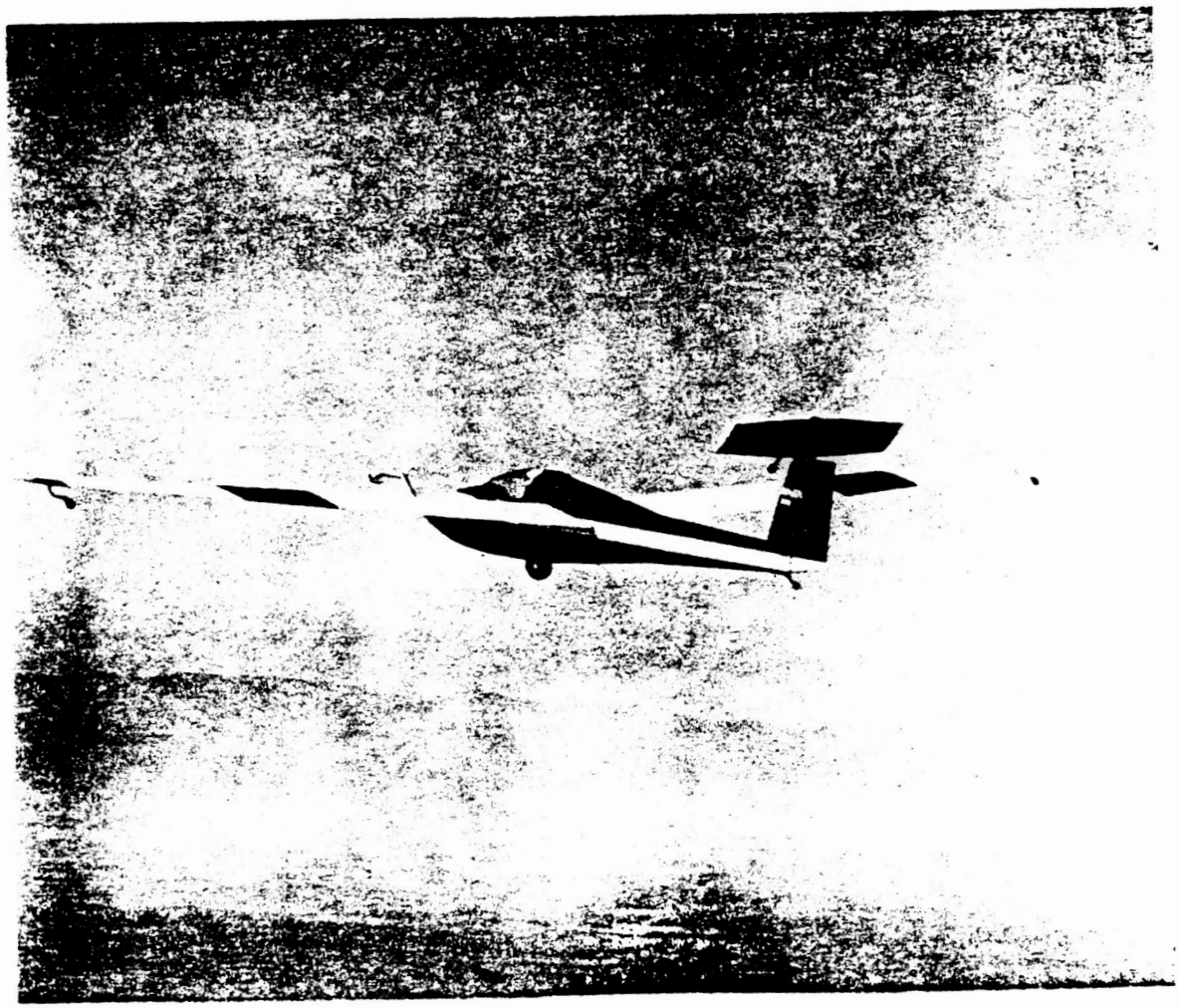

Figure 10: NASA SGS1-36 in deep stall flight with 50° angle of attack.

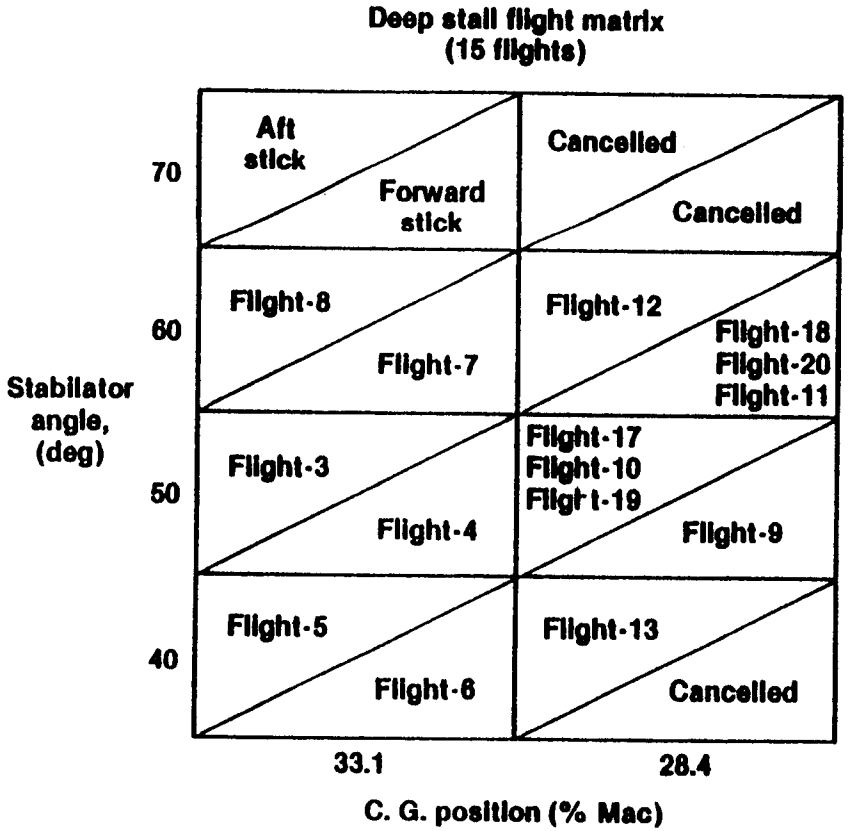

Exploritory flights	2
Deep stall data flights	15
Air-to-air photo flights	3
Total flights	20

Flight 1: System checkout of standard configuration

Flight 2: First deep stall flight, non data

Flights 14, 15, 16 photo flights

Figure 11: NASA SGS1-36 deep stall flight program

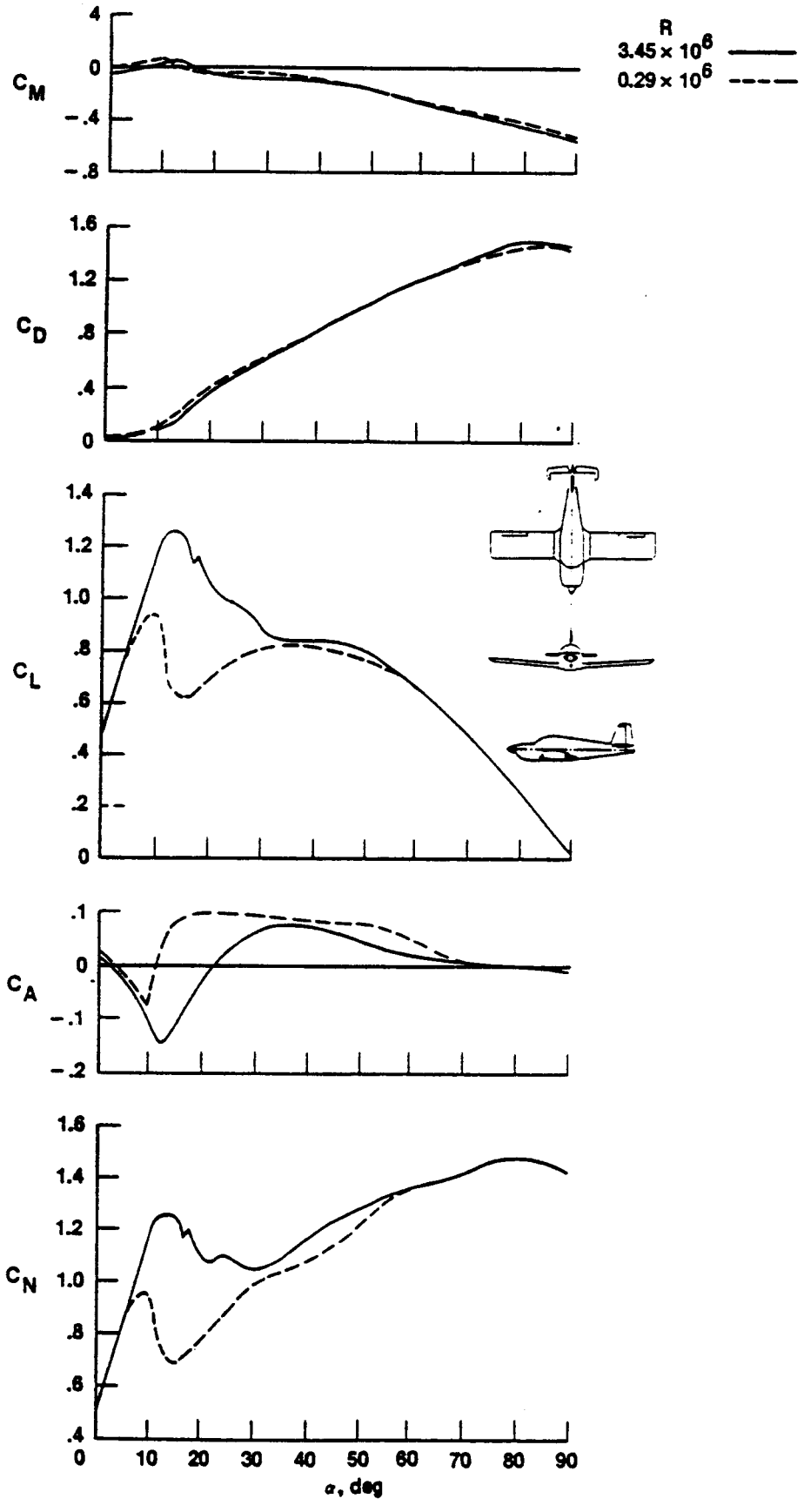

Figure 12: Effect of Reynolds Number on longitudinal characteristics of a typical light plane (Ref. 4)

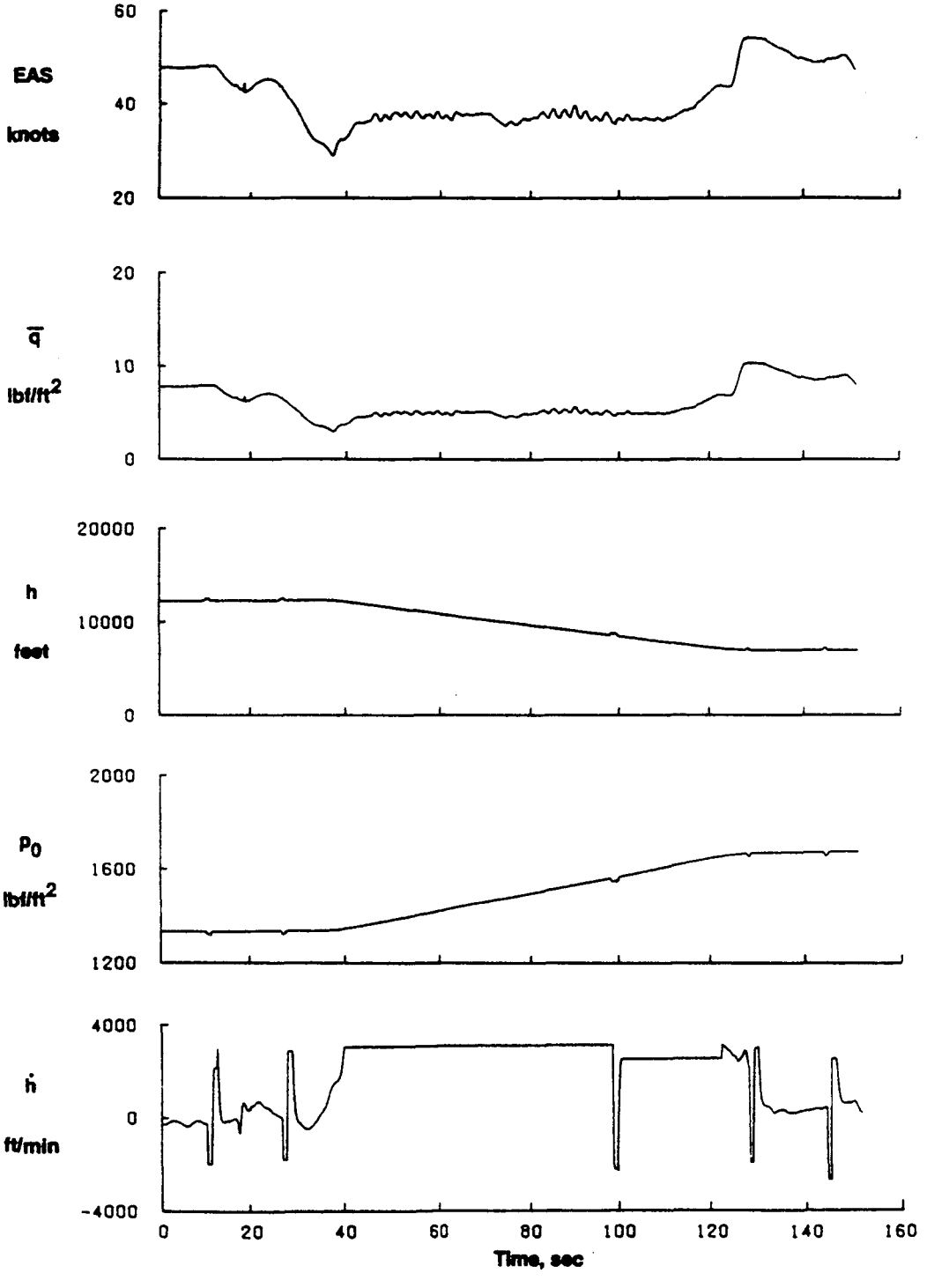

Figure 13: Complete deep stall time histories from flight 7.

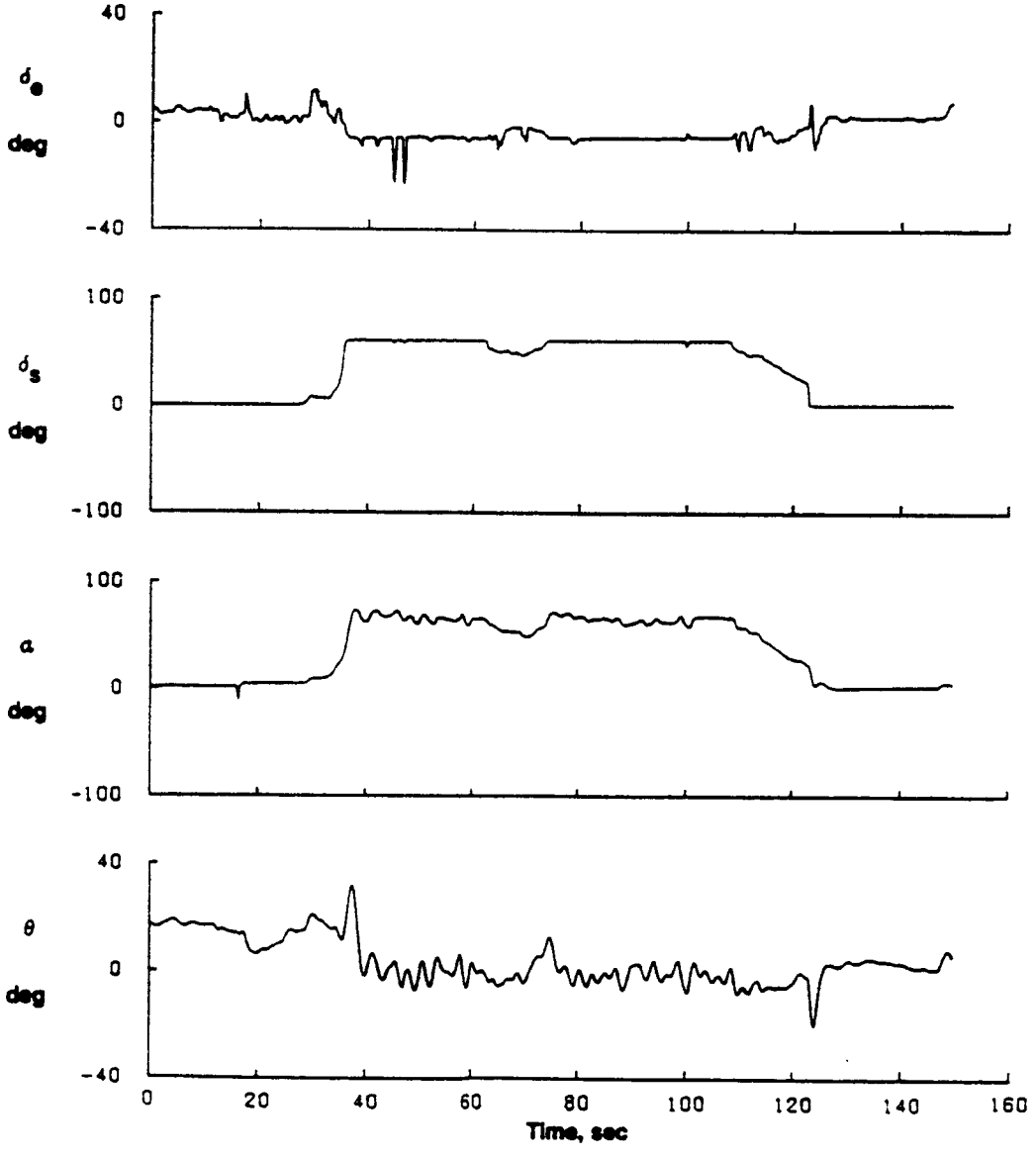

Figure 13: Continued.

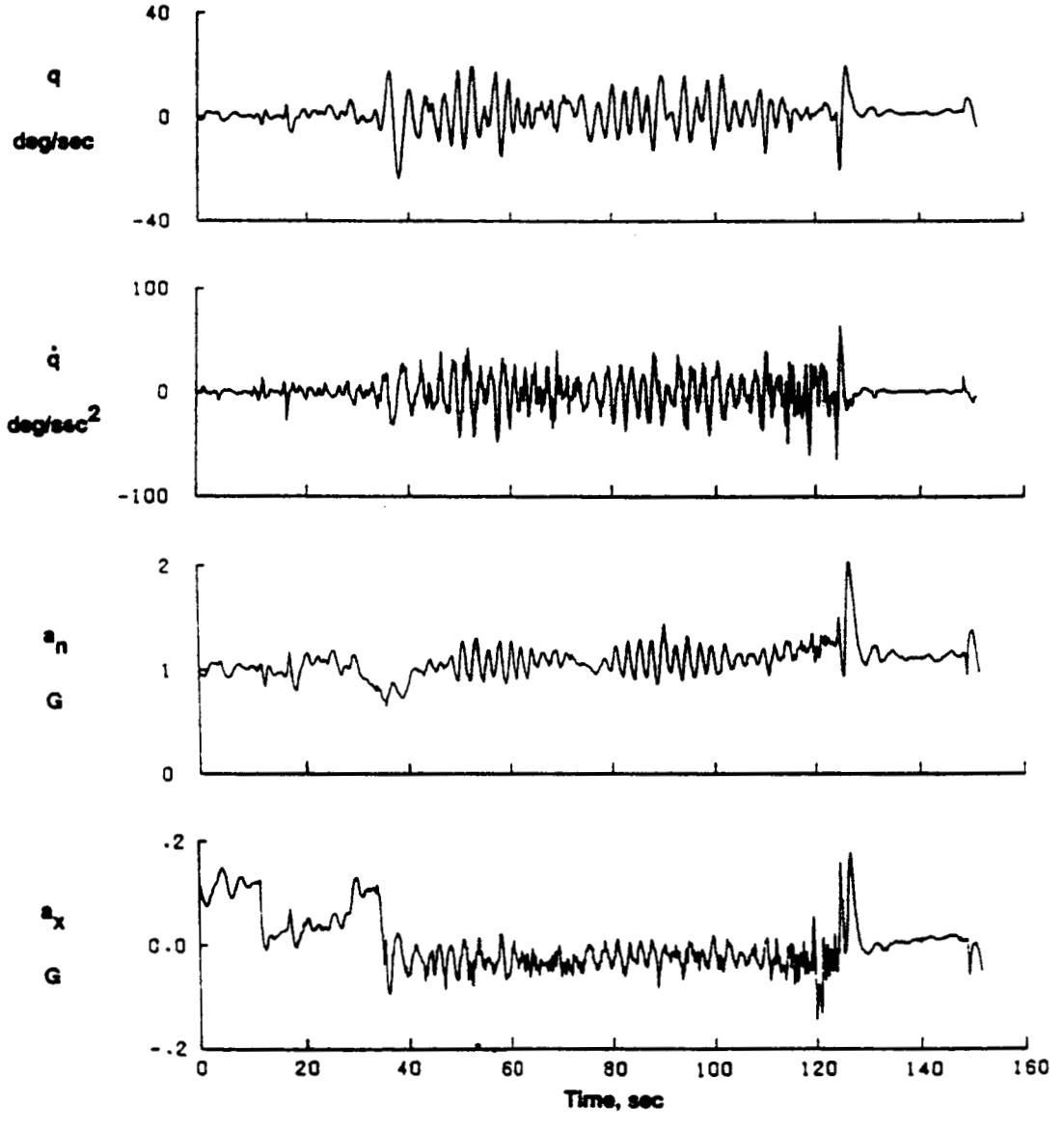

Figure 13: Continued.

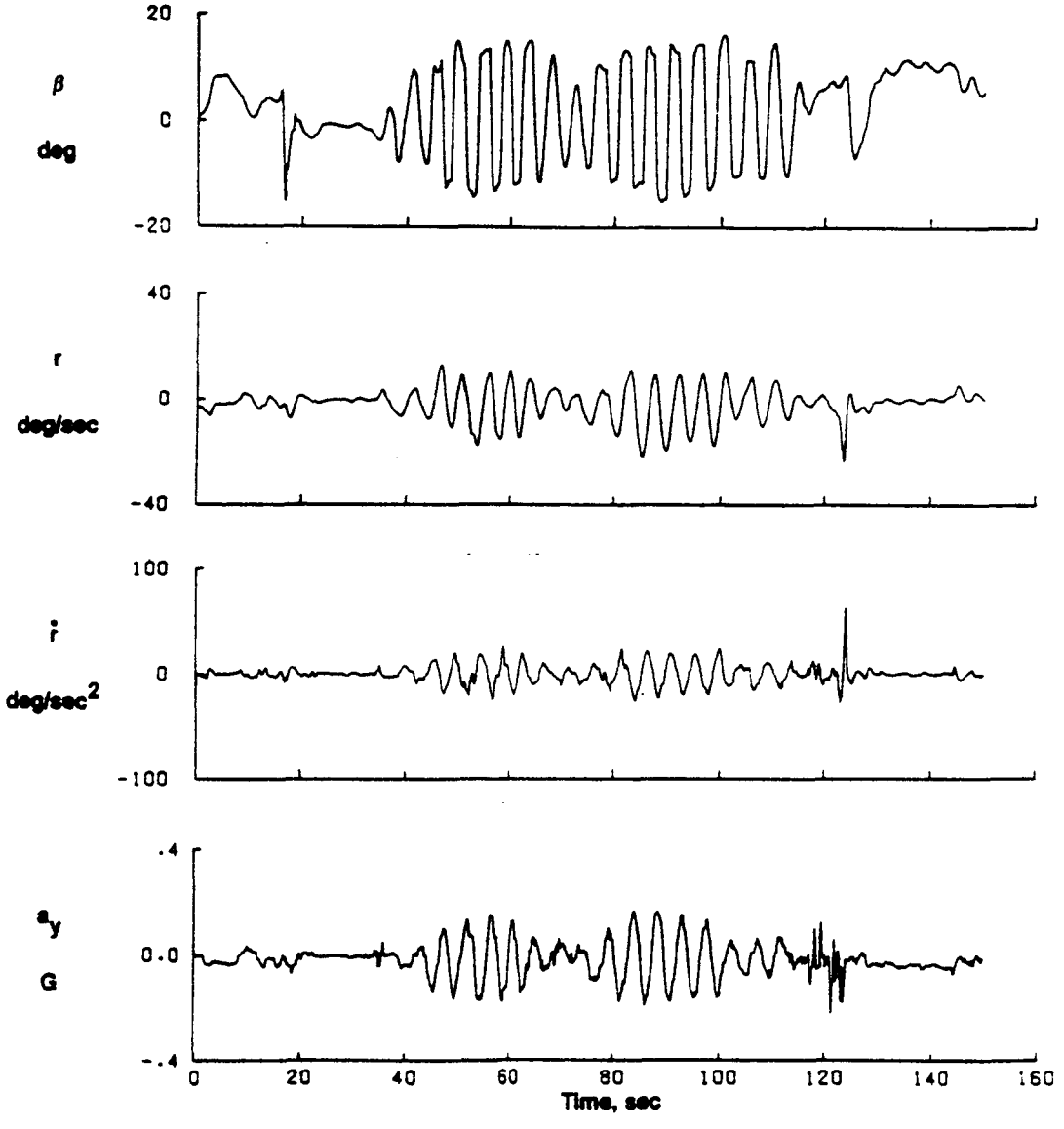

Figure 13: Continued.

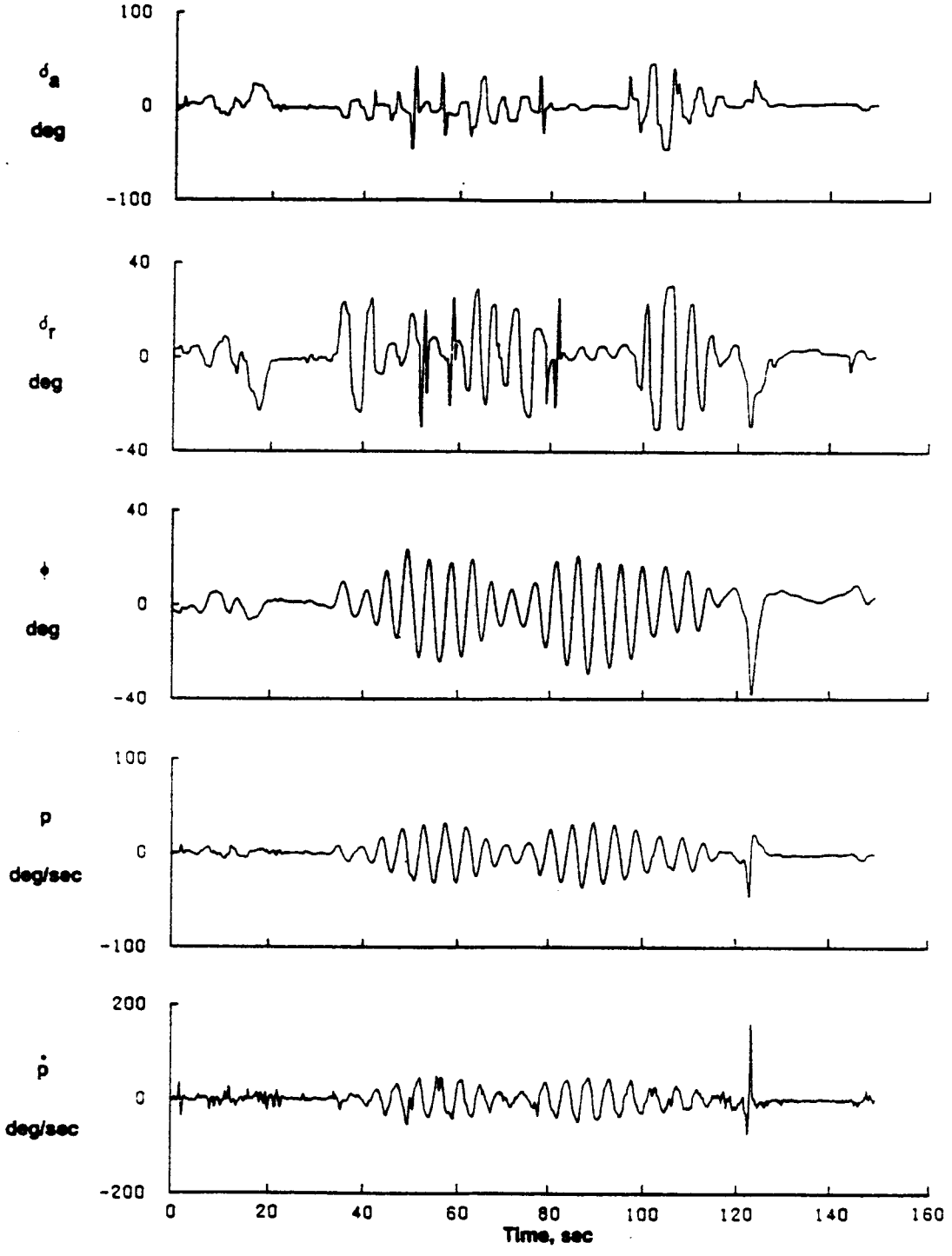

Figure 13: Continued.

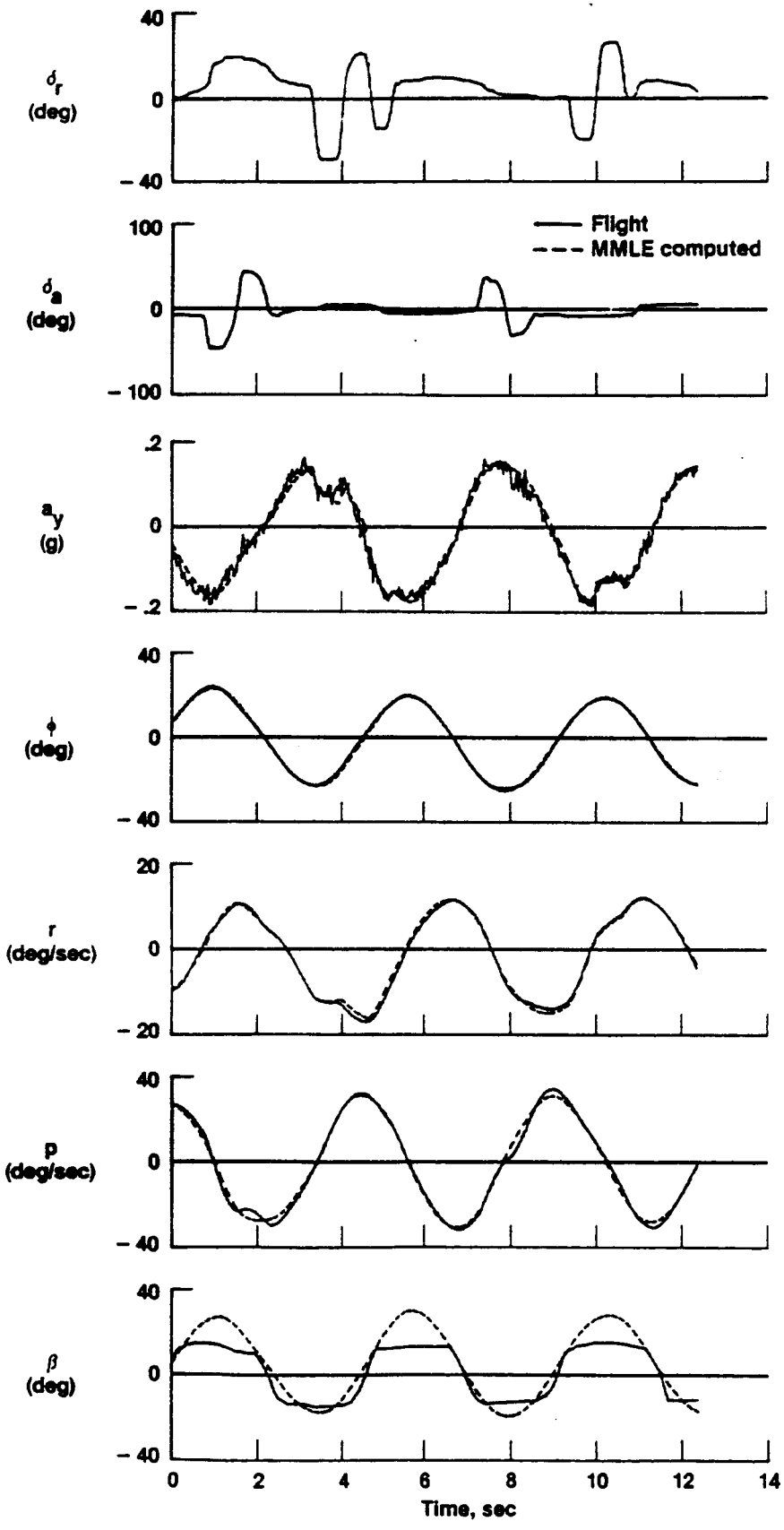

Figure 14: Lateral-directional flight determined and MMLE computed histories for Flight 7.

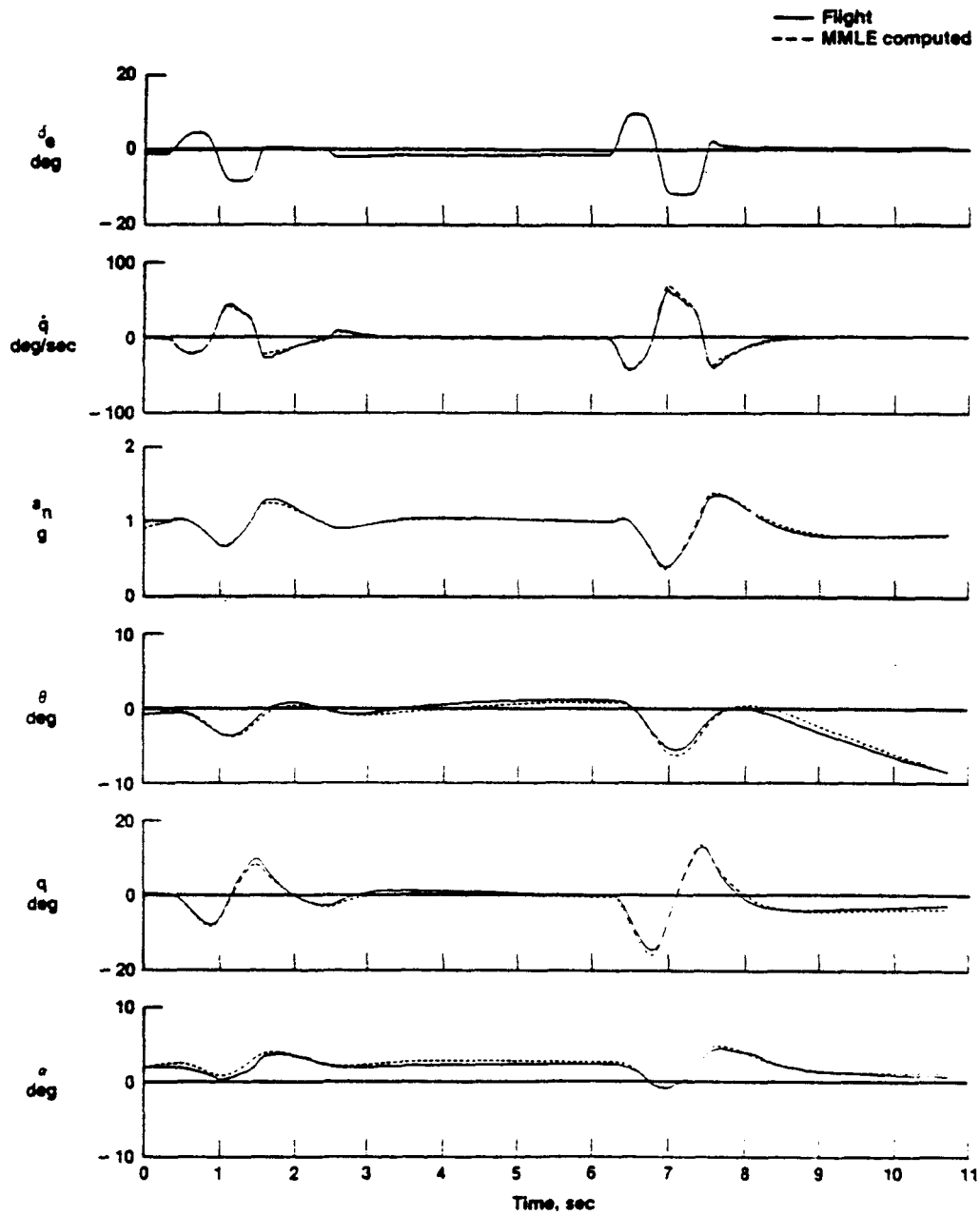

Figure 15: Longitudinal flight determined and MMLE computed time histories for Flight 13.

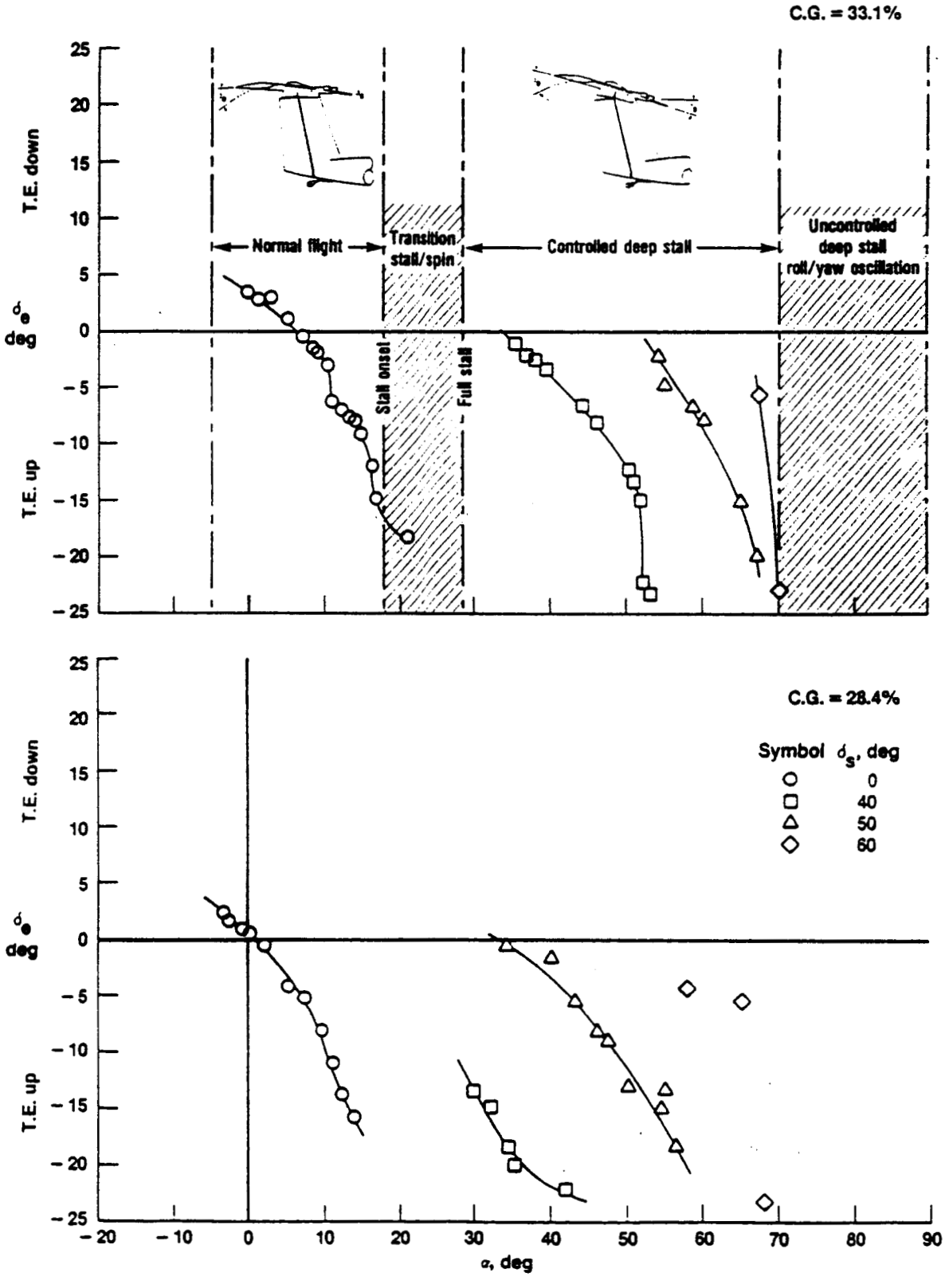

Figure 16: SGS-136 deep stall longitudinal flight determined trim data

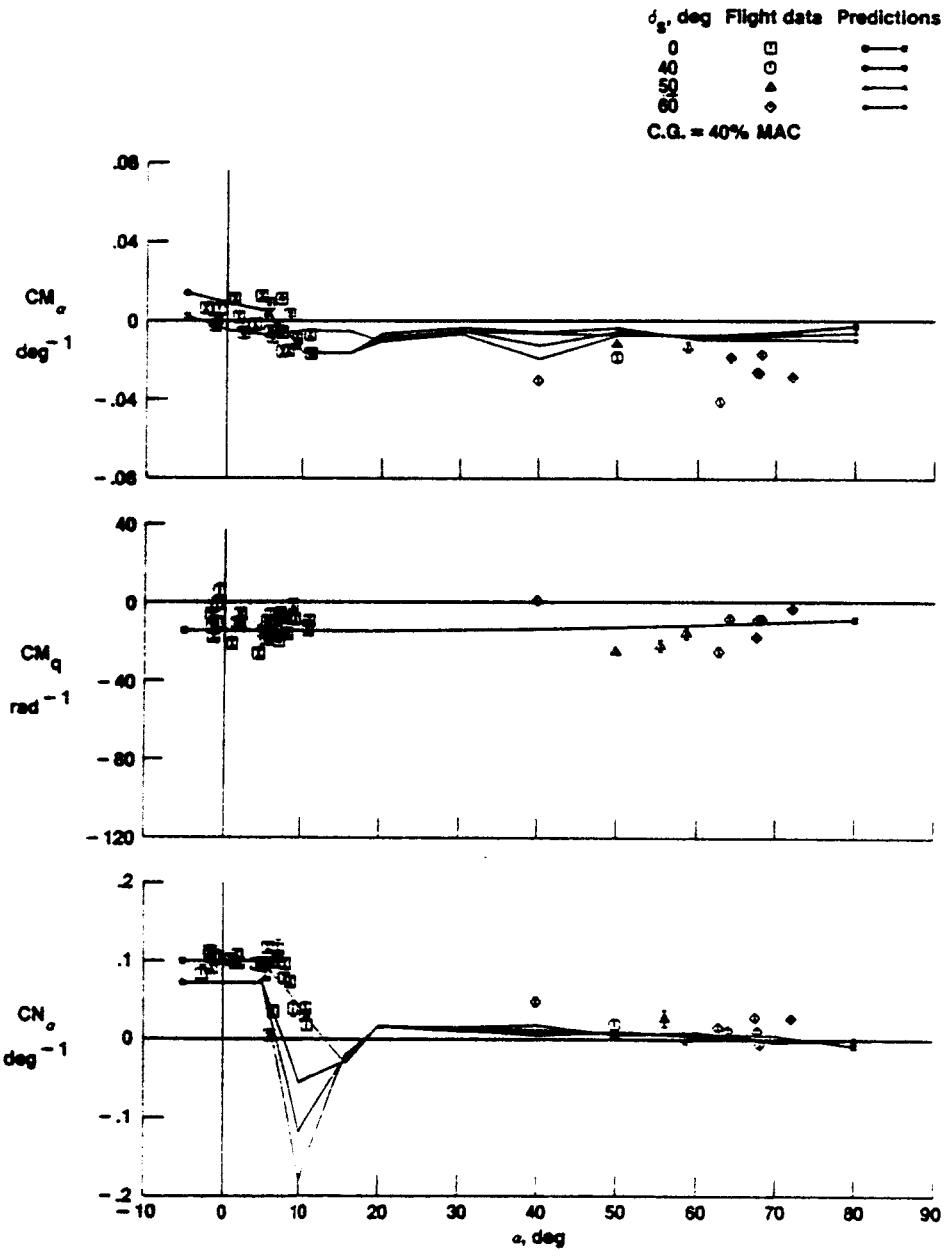

Figure 17: Predicted and flight determined longitudinal stability and control derivatives of NASA SGS 1-36.

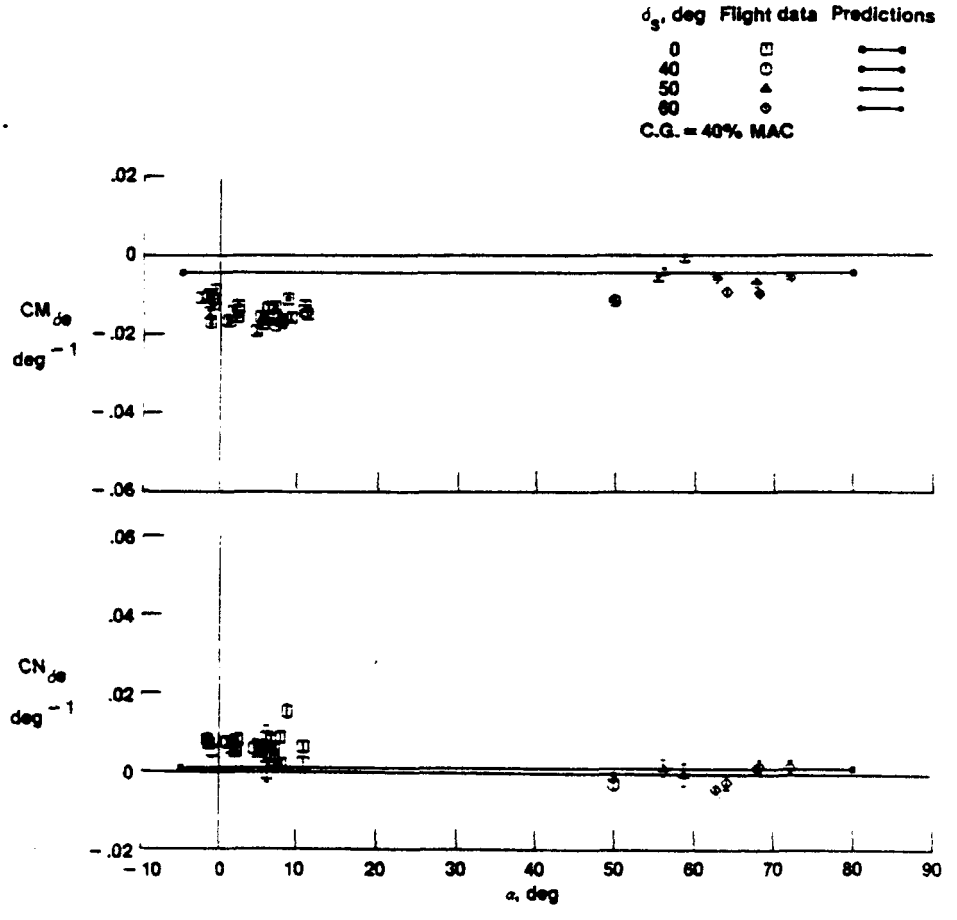

Figure 17: Continued.

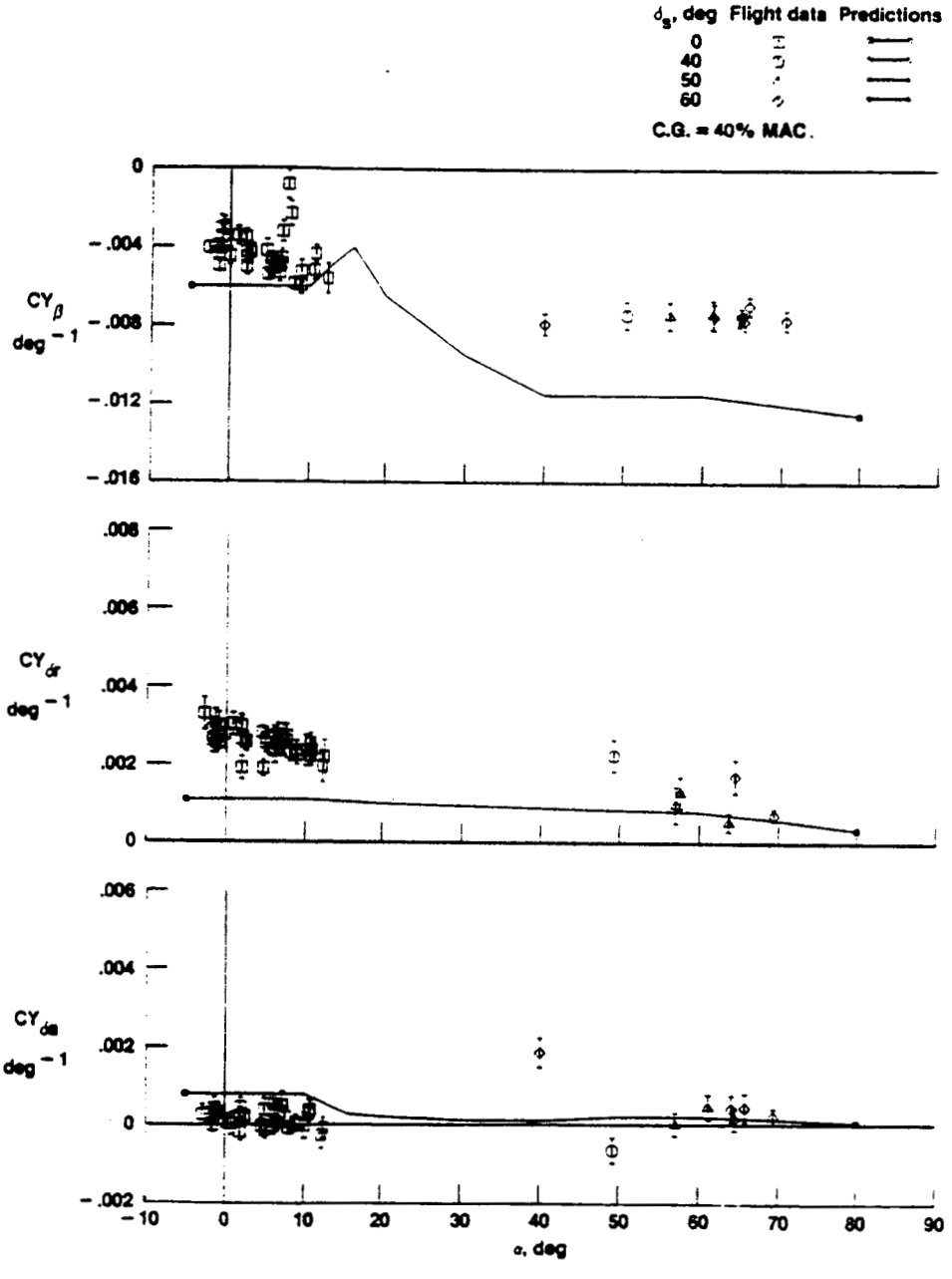

Figure 18: Predicted and flight determinded lateral-directional stability and control derivatives of NASA SGS 1-36.

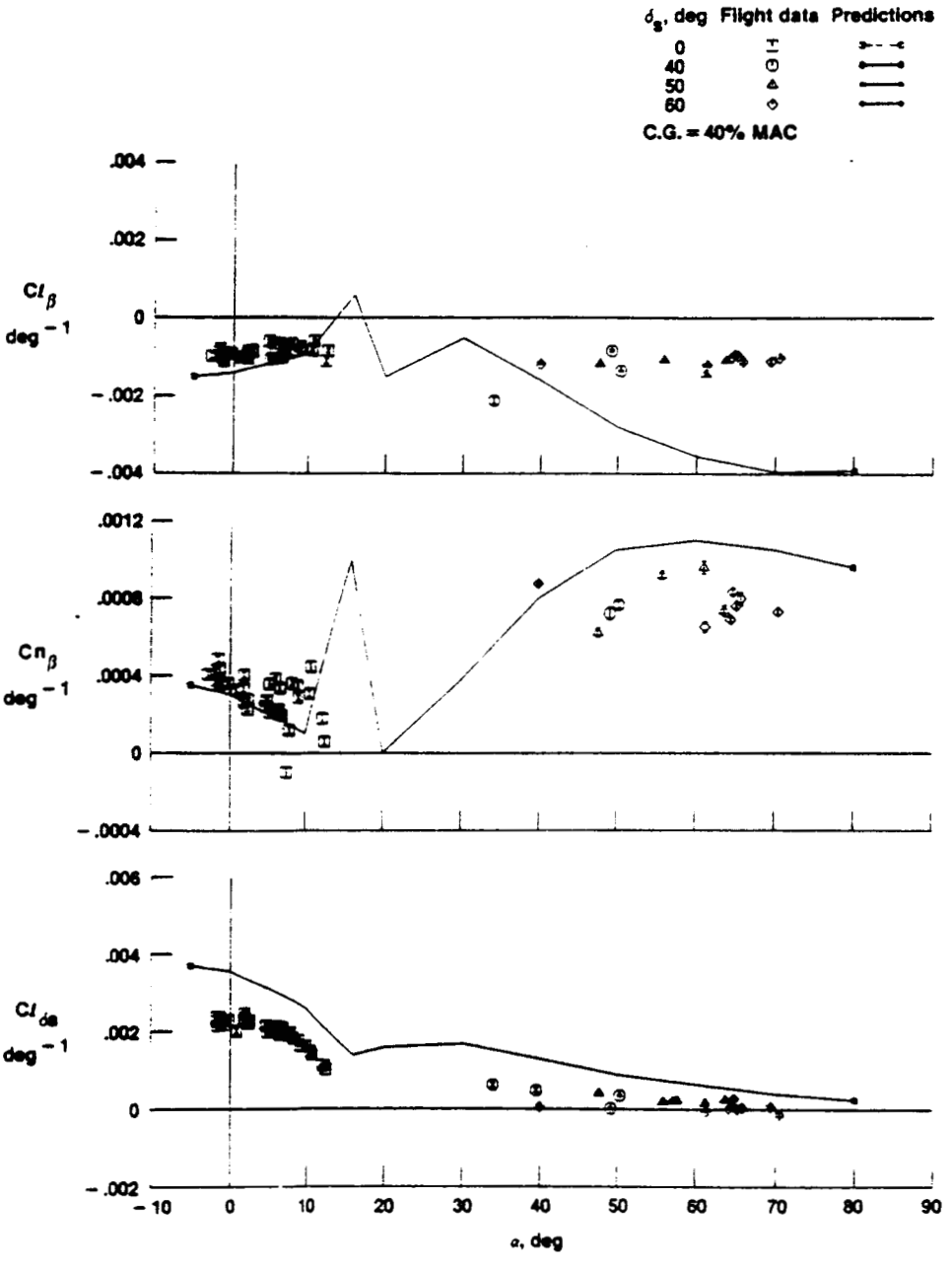

Figure 18: Continued.

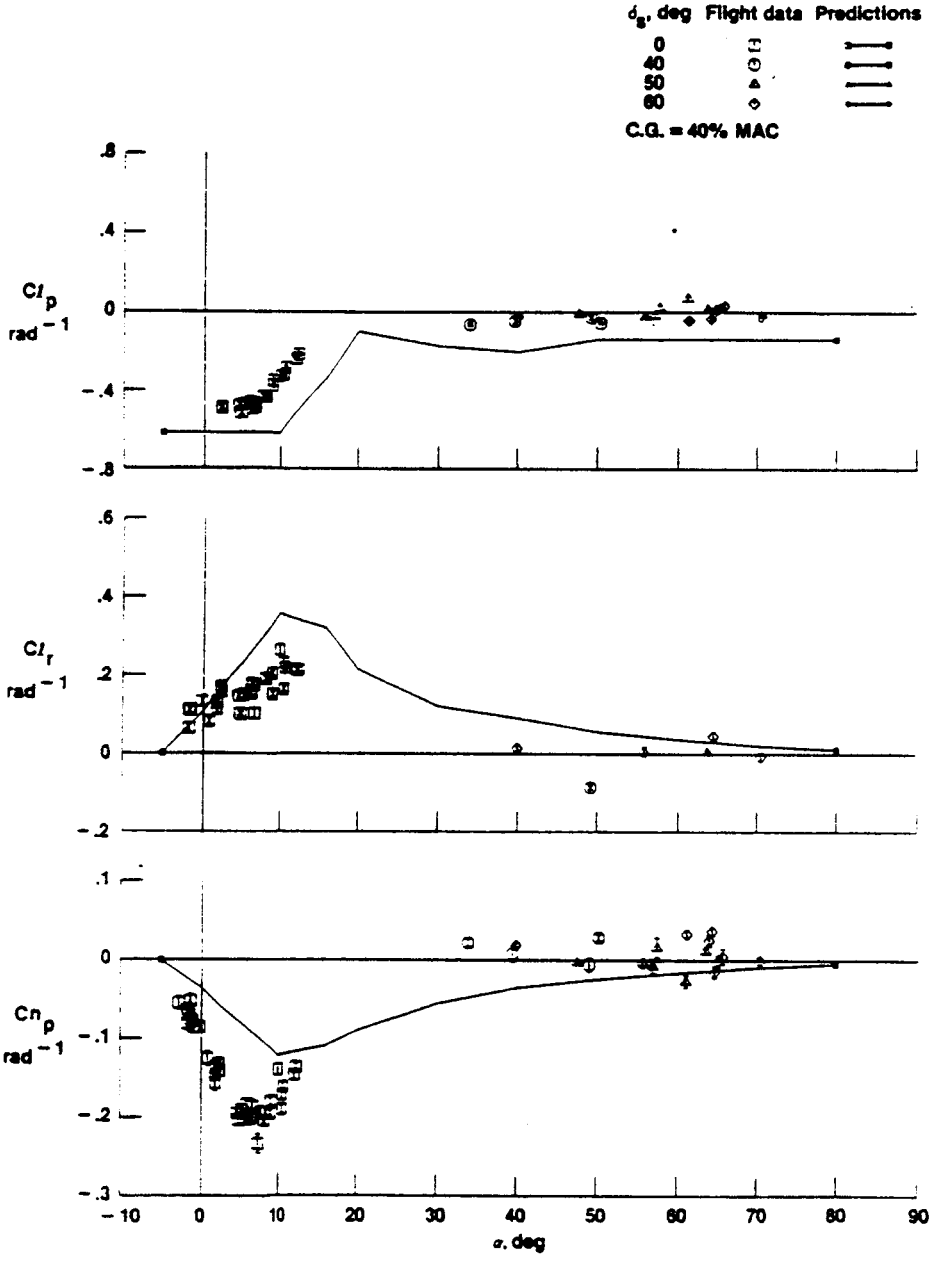

Figure 18: Continued.

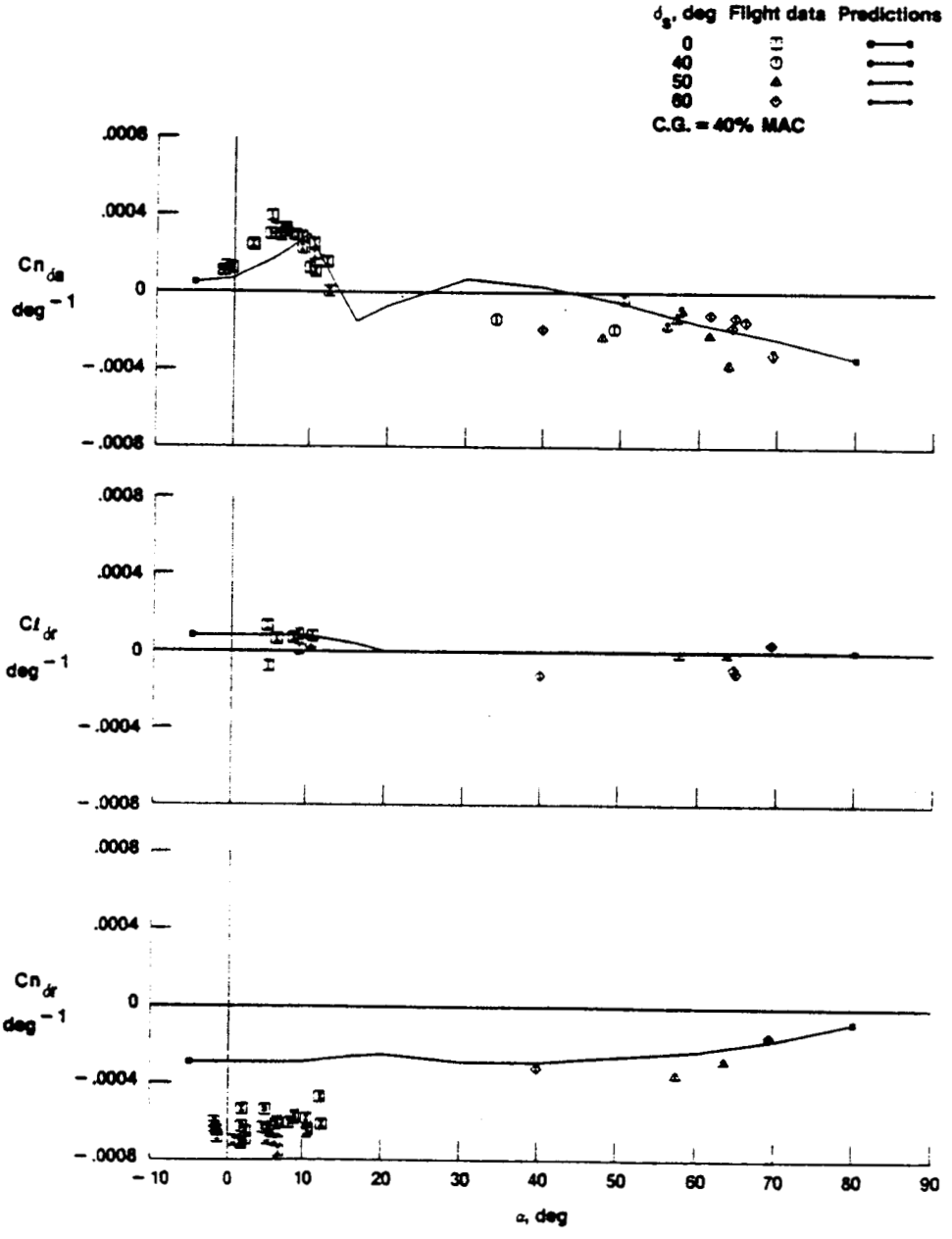

Figure 18: Continued.

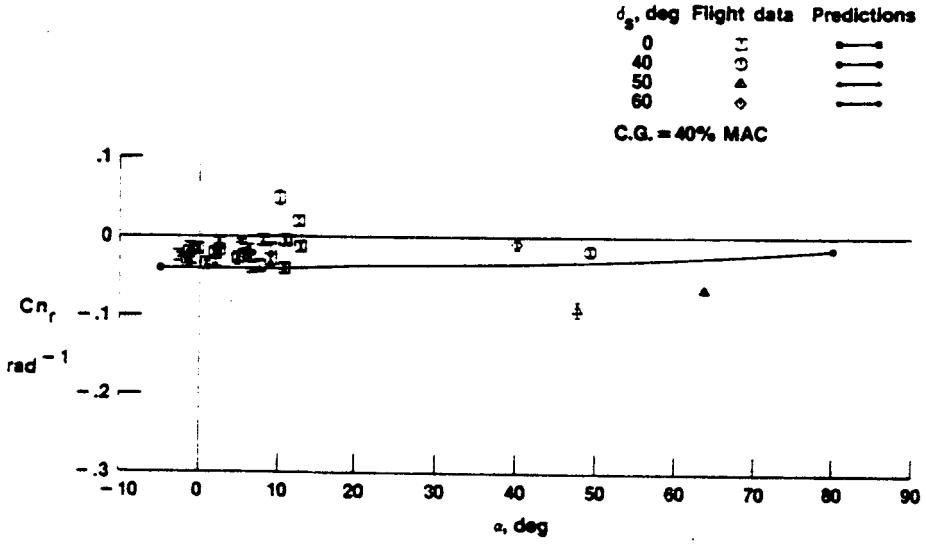

Figure 18: Continued.

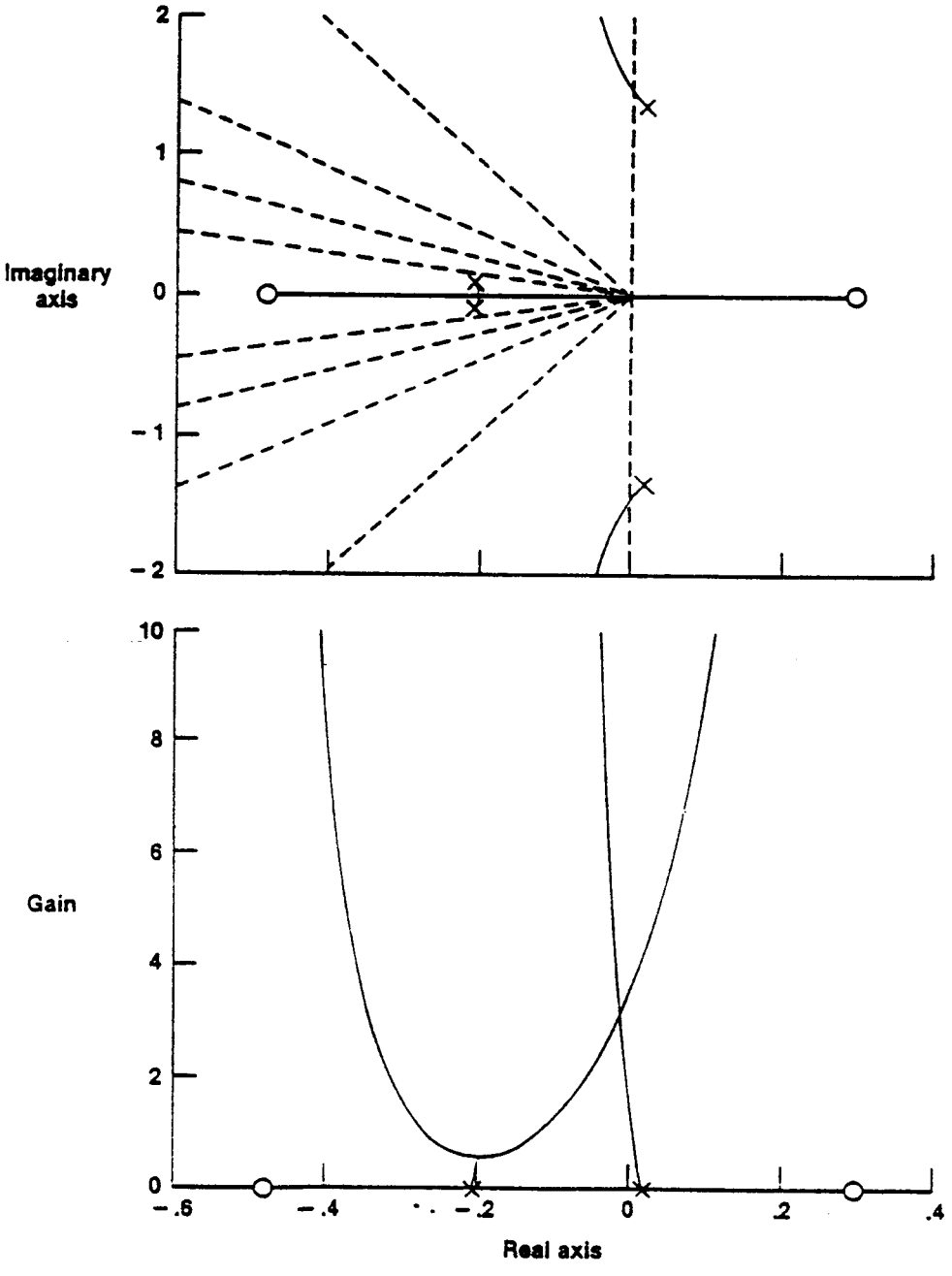

Figure 19: S-plane root locus plot of $^{a_y}/_{\delta a}$ for Flight 7.

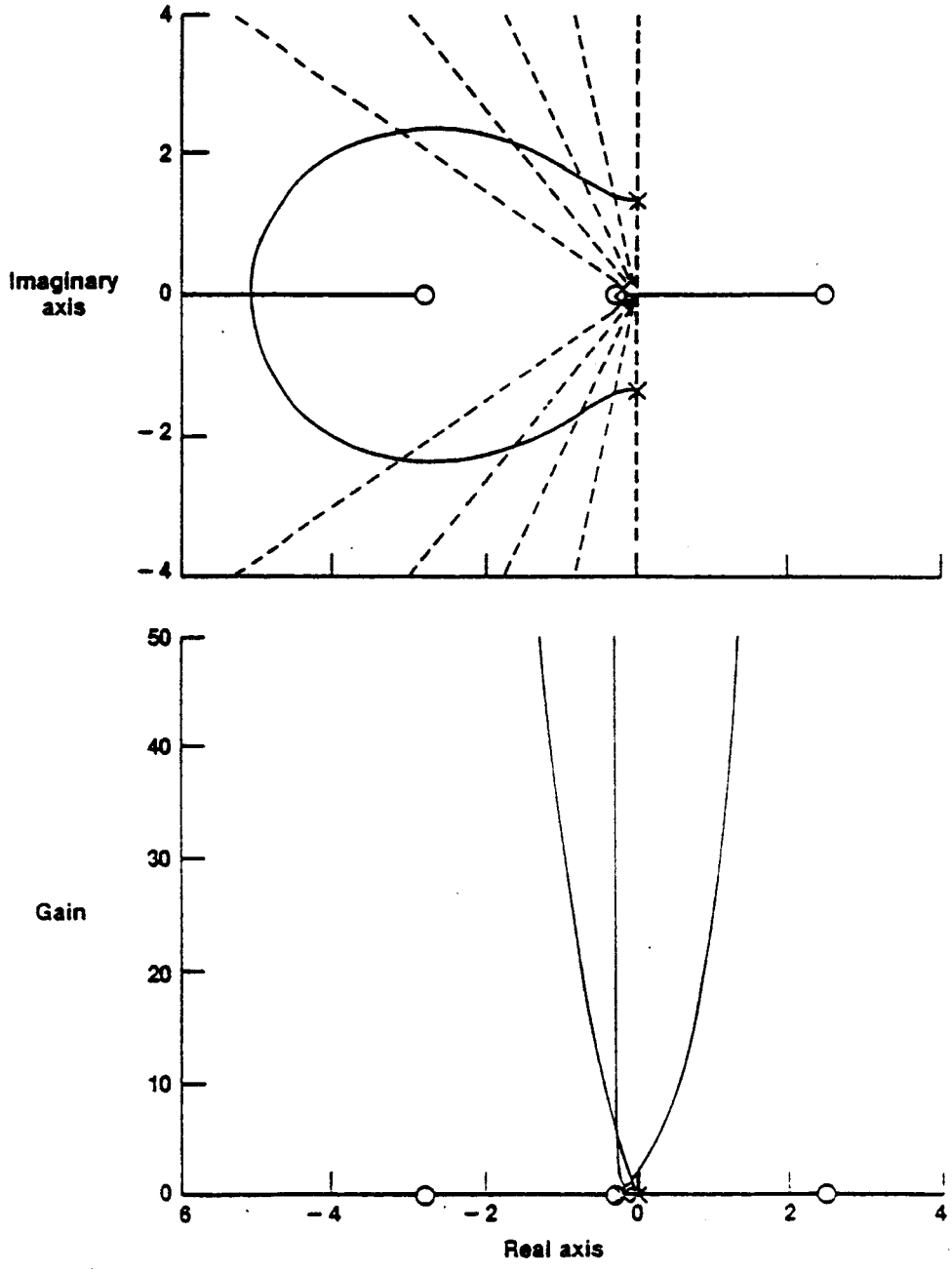

Figure 20: S-plane root locus plot of βI_{dr} for Flight 7.

Appendix A: This appendix presents the NASA SGS 1-36 non-dimensional aero-data package used for the real time simulation and initial linear analysis. The same data set was used as the initial starting values for the MMLE analysis. The static force and moment derivatives were obtained from the wind tunnel testing of the quarter scaled "free flight" model in stability axis and were transformed into body axis for presentation here. All the rotary aerodynamic stability derivatives are the predicted values as describe in the " Computed Aerodynamic Stability Derivatives" section of this report and are presented in body axis.

ORIGINAL PAGE IS
OF POOR QUALITY

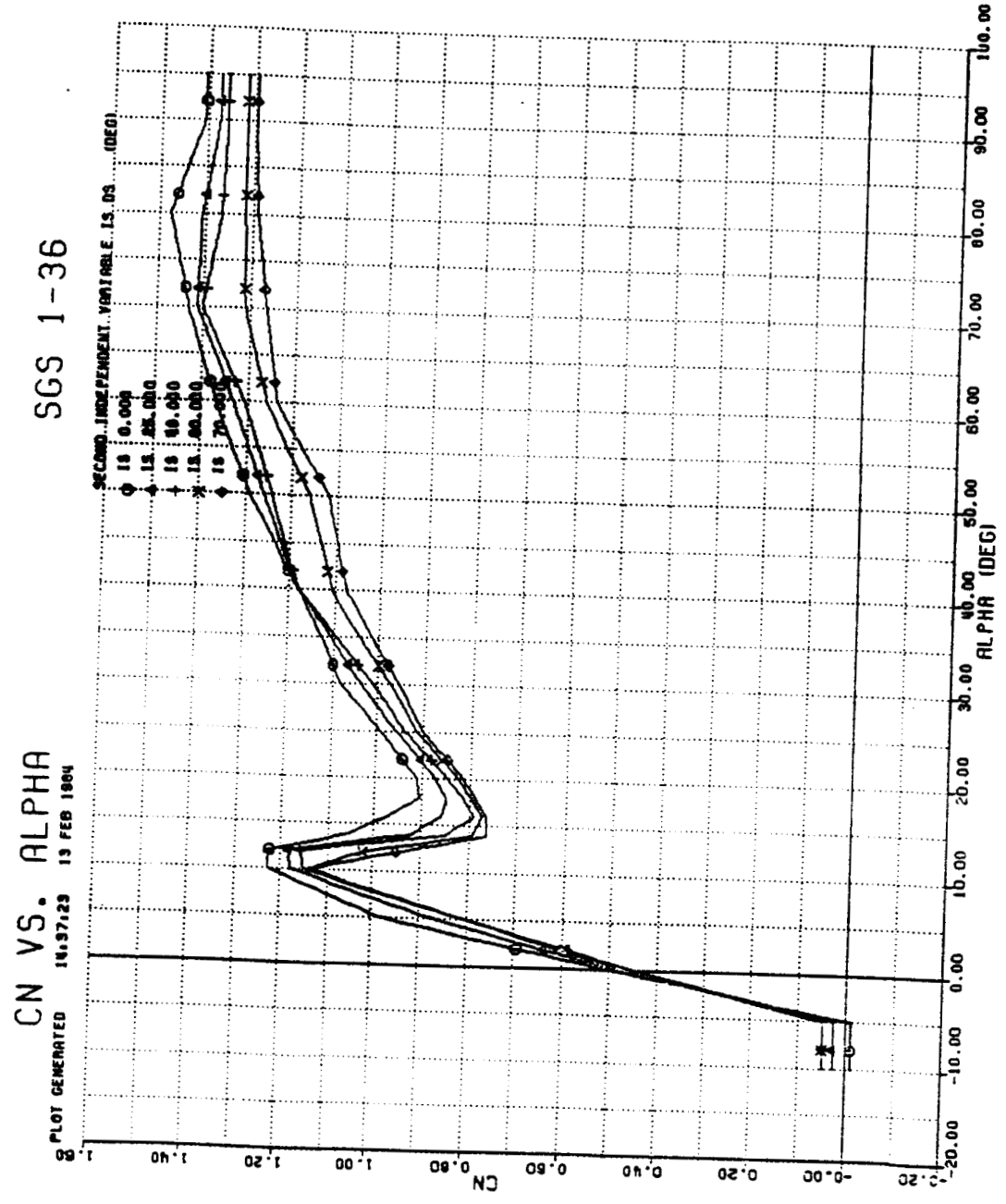

ORIGINAL PAGE IS
OF POOR QUALITY

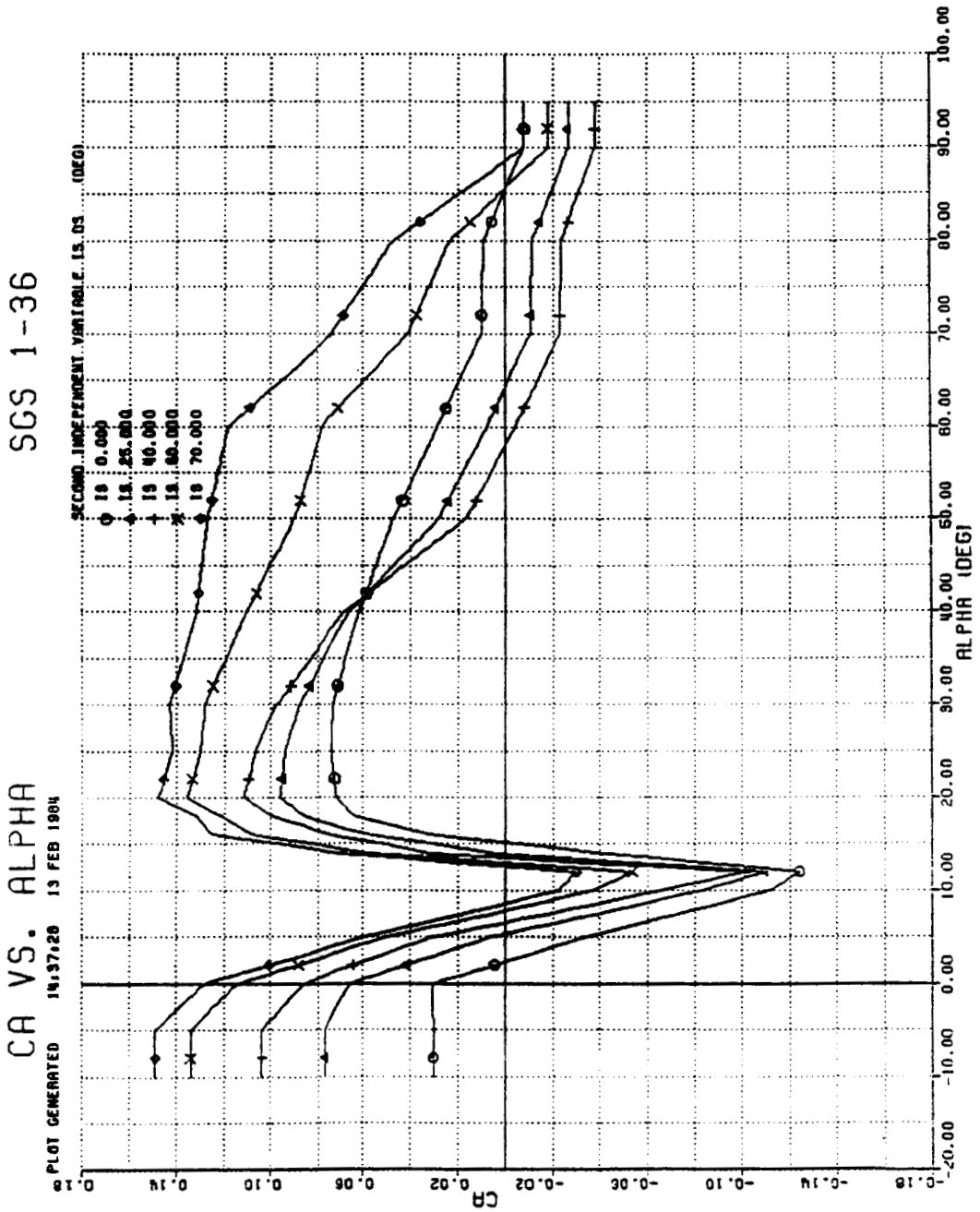

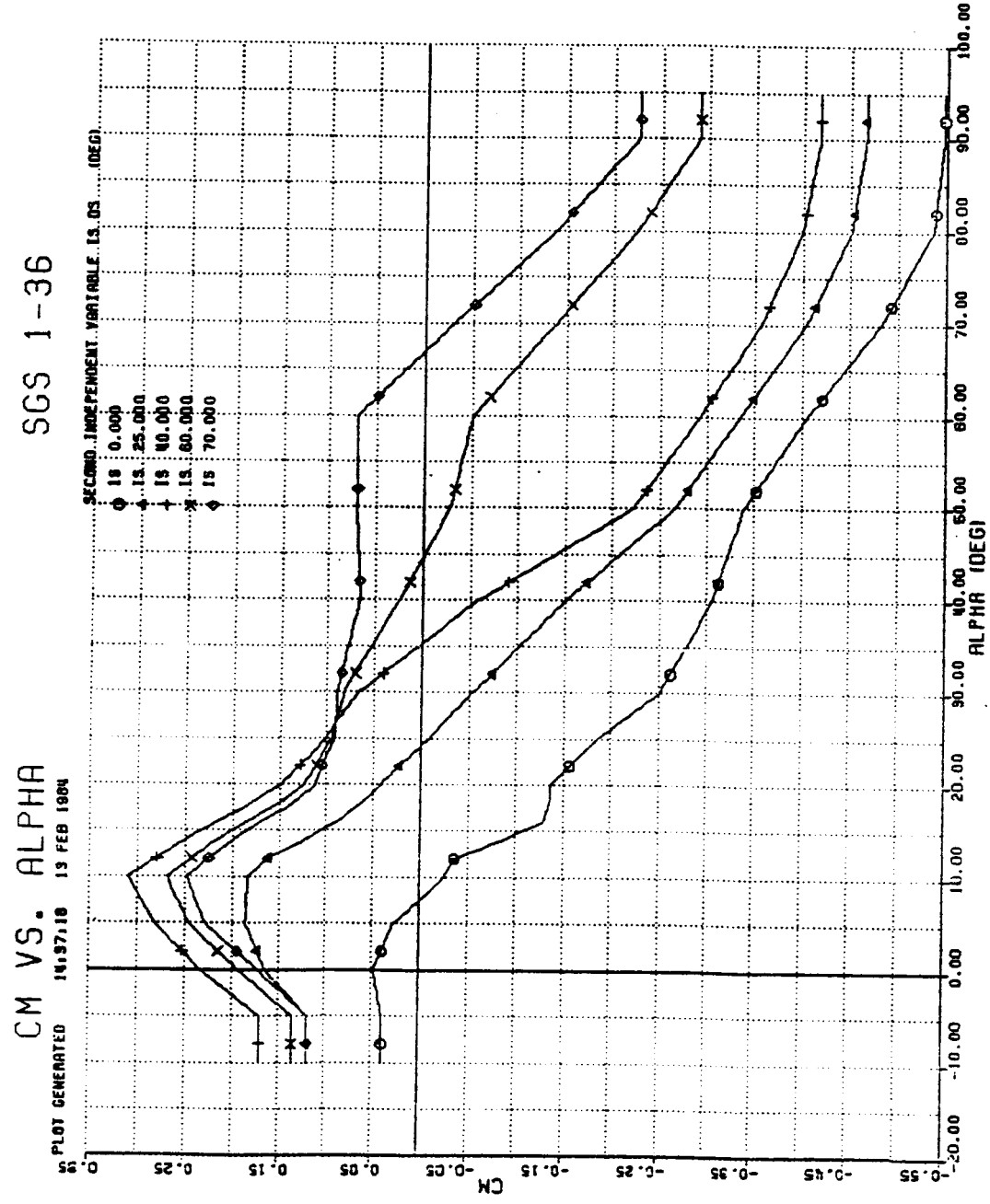
SGS 1-36
CM VS. ALPHA
PLOT GENERATED 14:37:18 13 FEB 1984
SECOND INDEPENDENT VARIABLE IS .03 (DEG)
IS 0.000
IS 25.000
IS 40.000
IS 60.000
IS 70.000
CM
ALPHA (DEG)
0.35
0.25
0.15
0.05
-0.05
-0.15
-0.25
-0.35
-0.45
-0.55
-20.00
-10.00
0.00
10.00
20.00
30.00
40.00
50.00
60.00
70.00
80.00
90.00
100.00

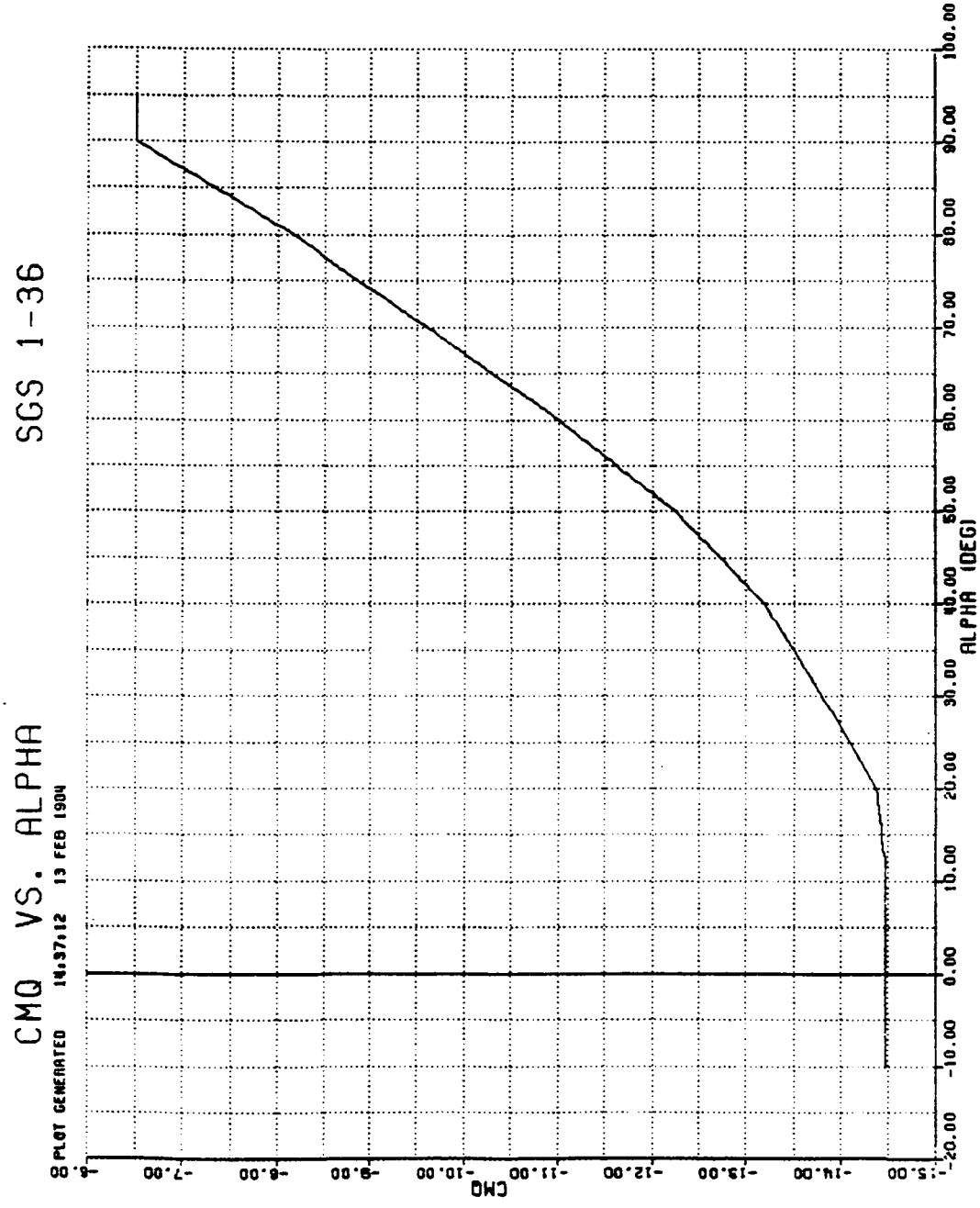

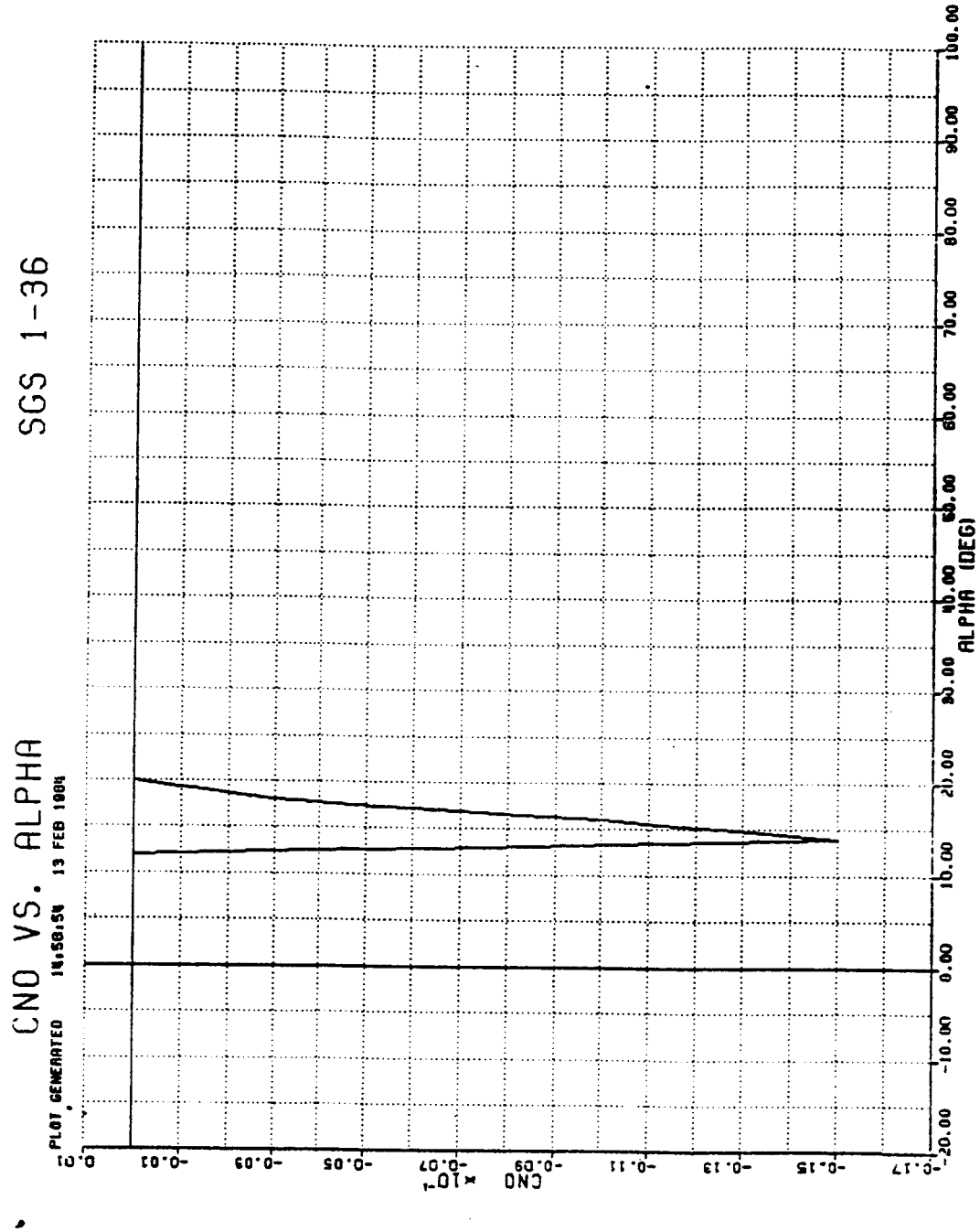
CNO VS. ALPHA
SGS 1-36
PLOT GENERATED 16:58:58 13 FEB 1984
CNO
×10⁻¹
0.01
-0.01
-0.03
-0.05
-0.07
-0.09
-0.11
-0.13
-0.15
-0.17
ALPHA (DEG)
100.00
90.00
80.00
70.00
60.00
50.00
40.00
30.00
20.00
10.00
0.00
-10.00
-20.00

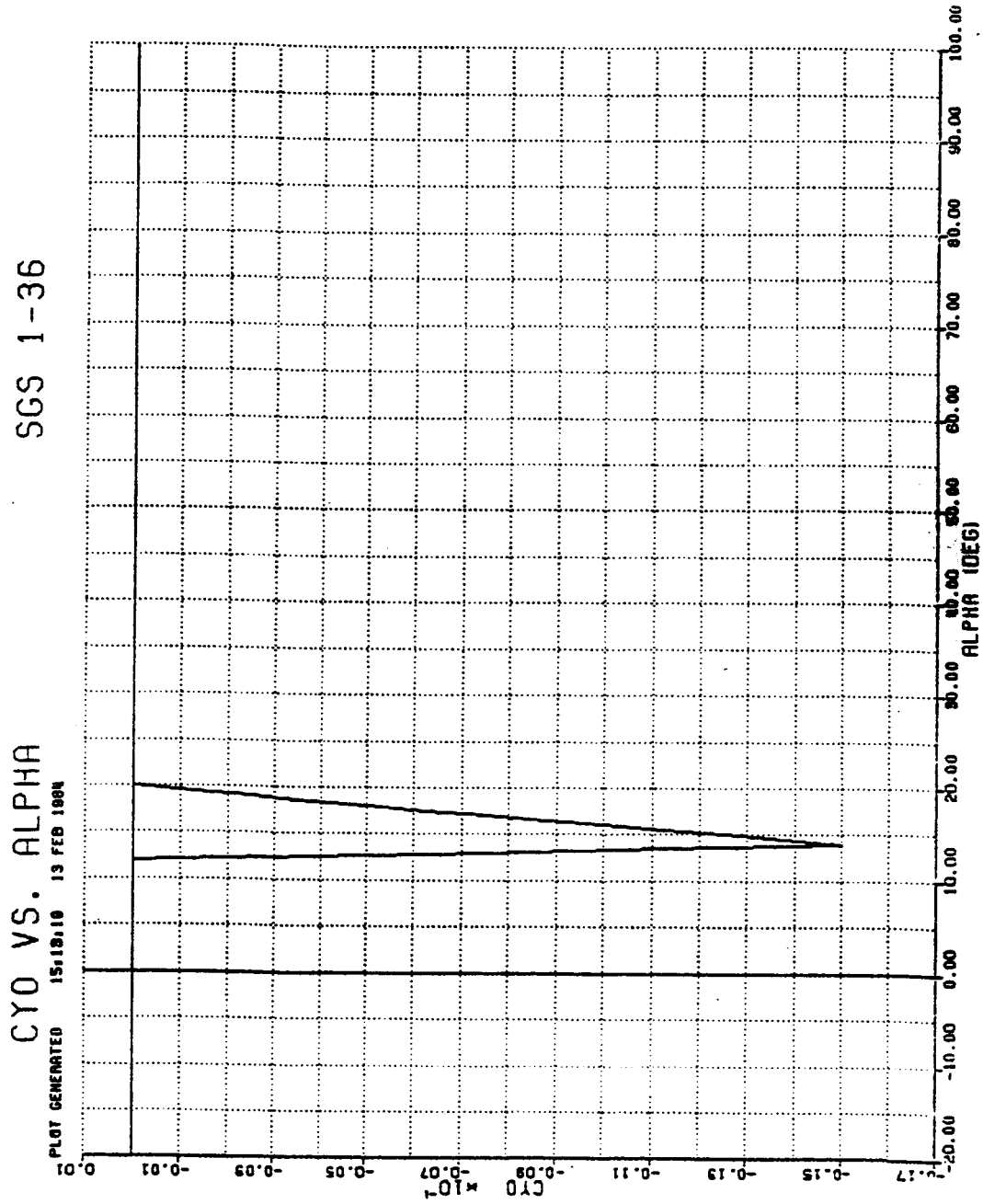
CYO VS. ALPHA
SGS 1-36
PLOT GENERATED 15:18:18 13 FEB 1988
CYO *10^-1
0.01
-0.01
-0.03
-0.05
-0.07
-0.09
-0.11
-0.13
-0.15
-0.17
ALPHA (DEG)
100.00
90.00
80.00
70.00
60.00
50.00
40.00
30.00
20.00
10.00
0.00
-10.00
-20.00

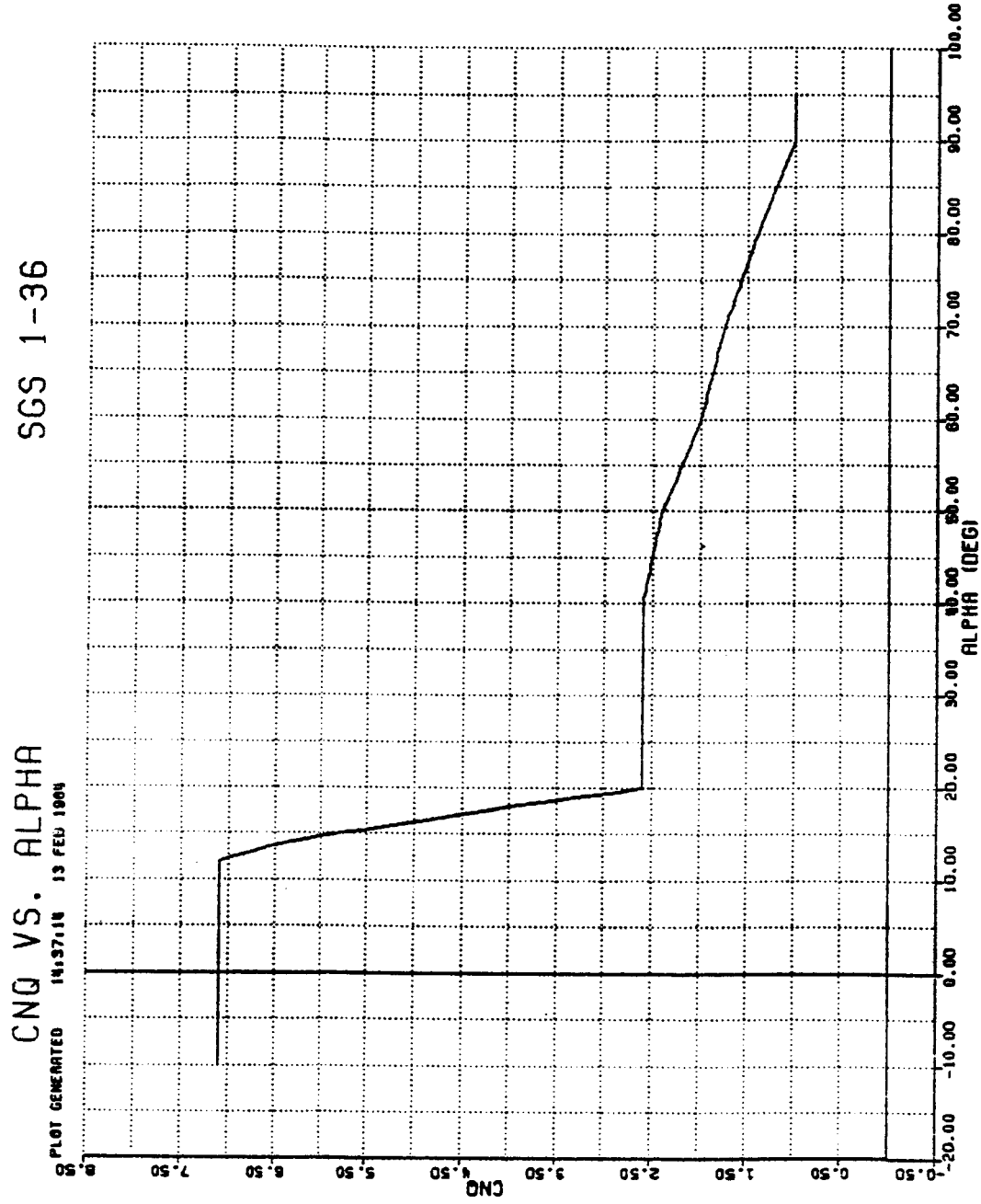
CNQ VS. ALPHA
SGS 1-36
PLOT GENERATED 14:37:18 13 FEB 1986
CNQ
ALPHA (DEG)
-0.50
0.50
1.50
2.50
3.50
4.50
5.50
6.50
7.50
8.50
-20.00
-10.00
0.00
10.00
20.00
30.00
40.00
50.00
60.00
70.00
80.00
90.00
100.00

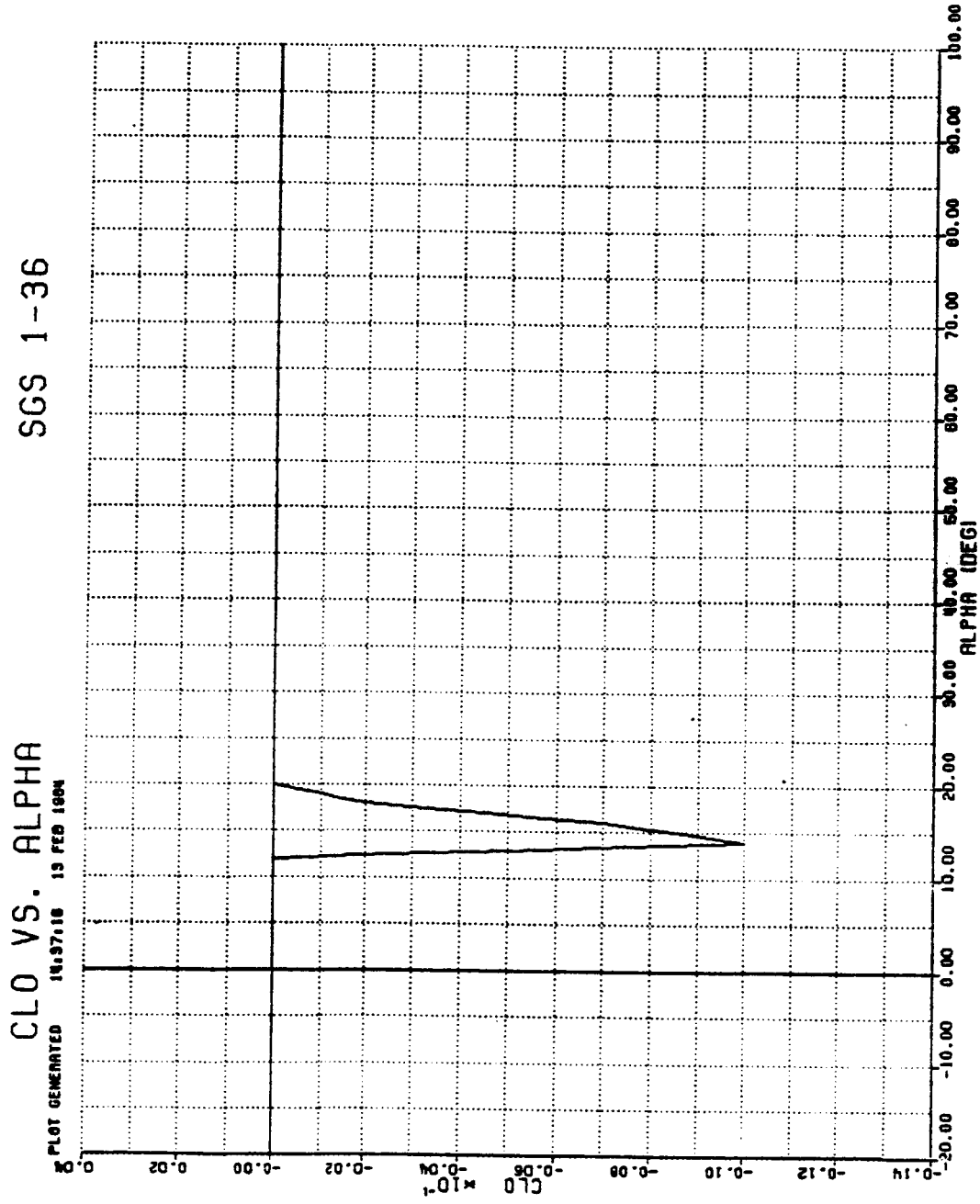
CLO VS. ALPHA
SGS 1-36
PLOT GENERATED 15:37:16 13 FEB 1984
CLO ×10⁻¹
ALPHA (DEG)
0.02
0.00
-0.02
-0.04
-0.06
-0.08
-0.10
-0.12
-0.14
100.00
90.00
80.00
70.00
60.00
50.00
40.00
30.00
20.00
10.00
0.00
-10.00
-20.00

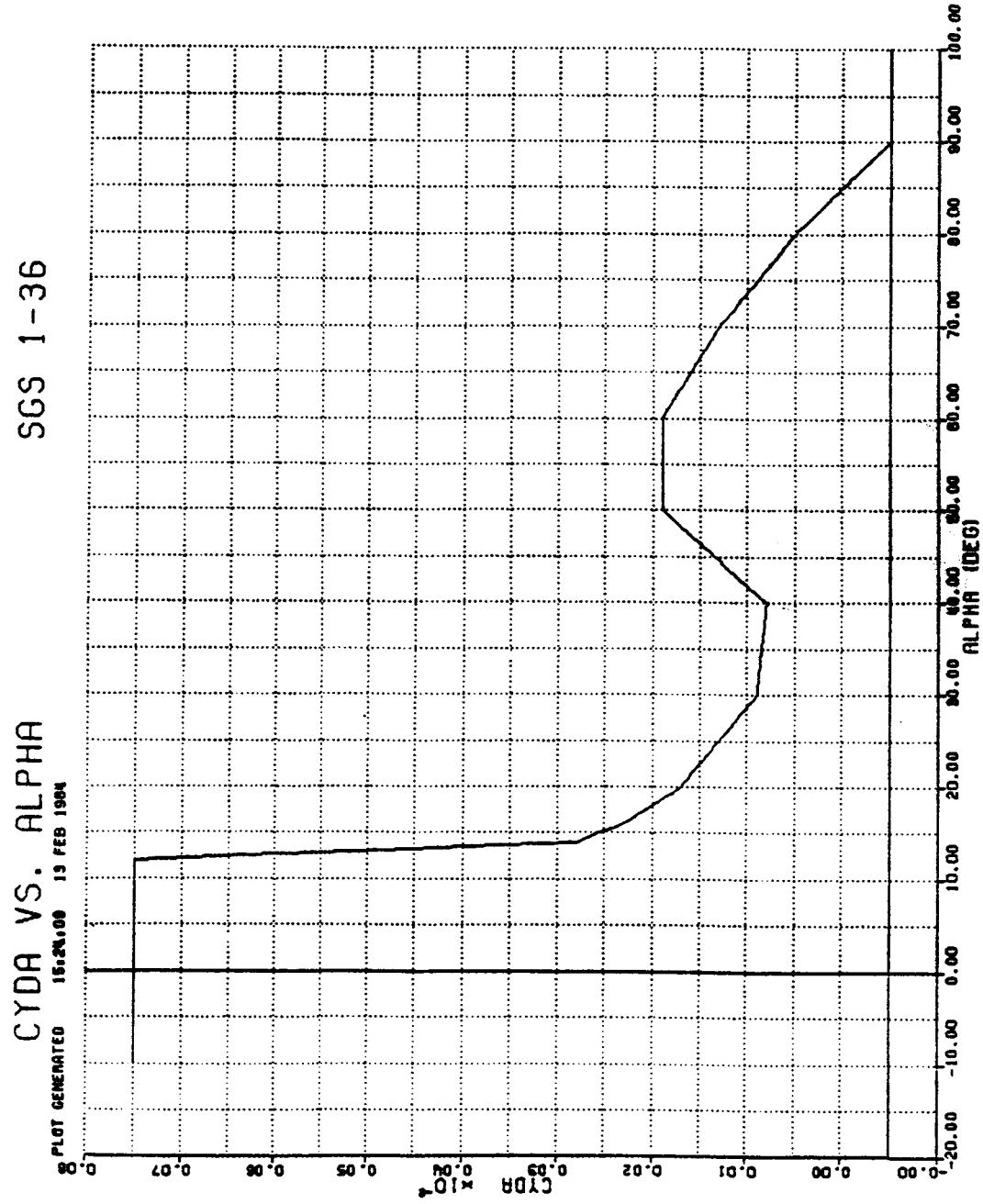
CYDA VS. ALPHA
SGS 1-36
PLOT GENERATED 15:24:00 13 FEB 1984
CYDA x10⁻⁴
ALPHA (DEG)
0.08
0.07
0.06
0.05
0.04
0.03
0.02
0.01
0.00
-20.00
-10.00
0.00
10.00
20.00
30.00
40.00
50.00
60.00
70.00
80.00
90.00
100.00

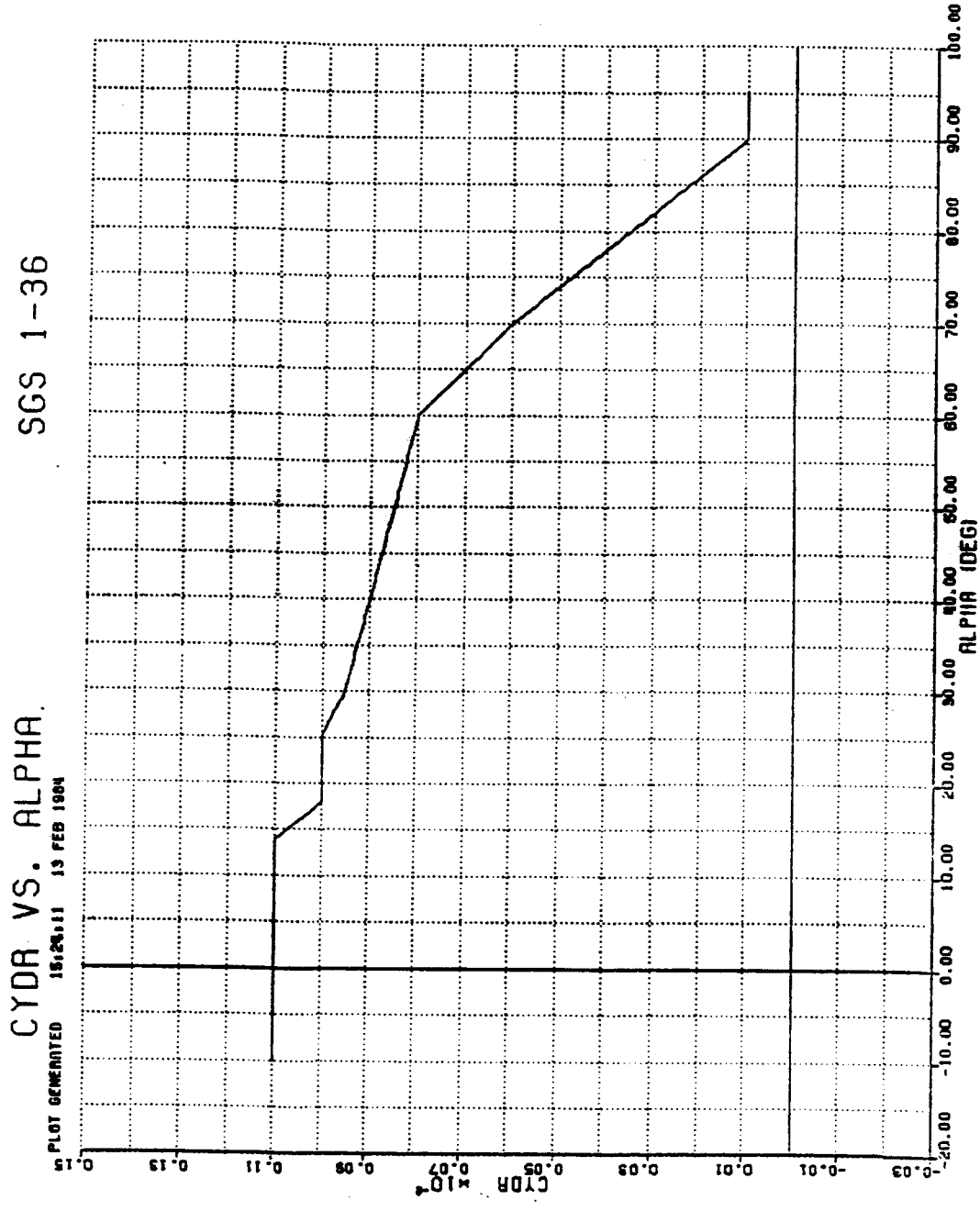
CYDR VS. ALPHA
SGS 1-36
PLOT GENERATED 15:26:11 13 FEB 1984
CYDR x10⁻⁴
ALPHA (DEG)
0.15
0.13
0.11
0.09
0.07
0.05
0.03
0.01
-0.01
-0.03
100.00
90.00
80.00
70.00
60.00
50.00
40.00
30.00
20.00
10.00
0.00
-10.00
-20.00

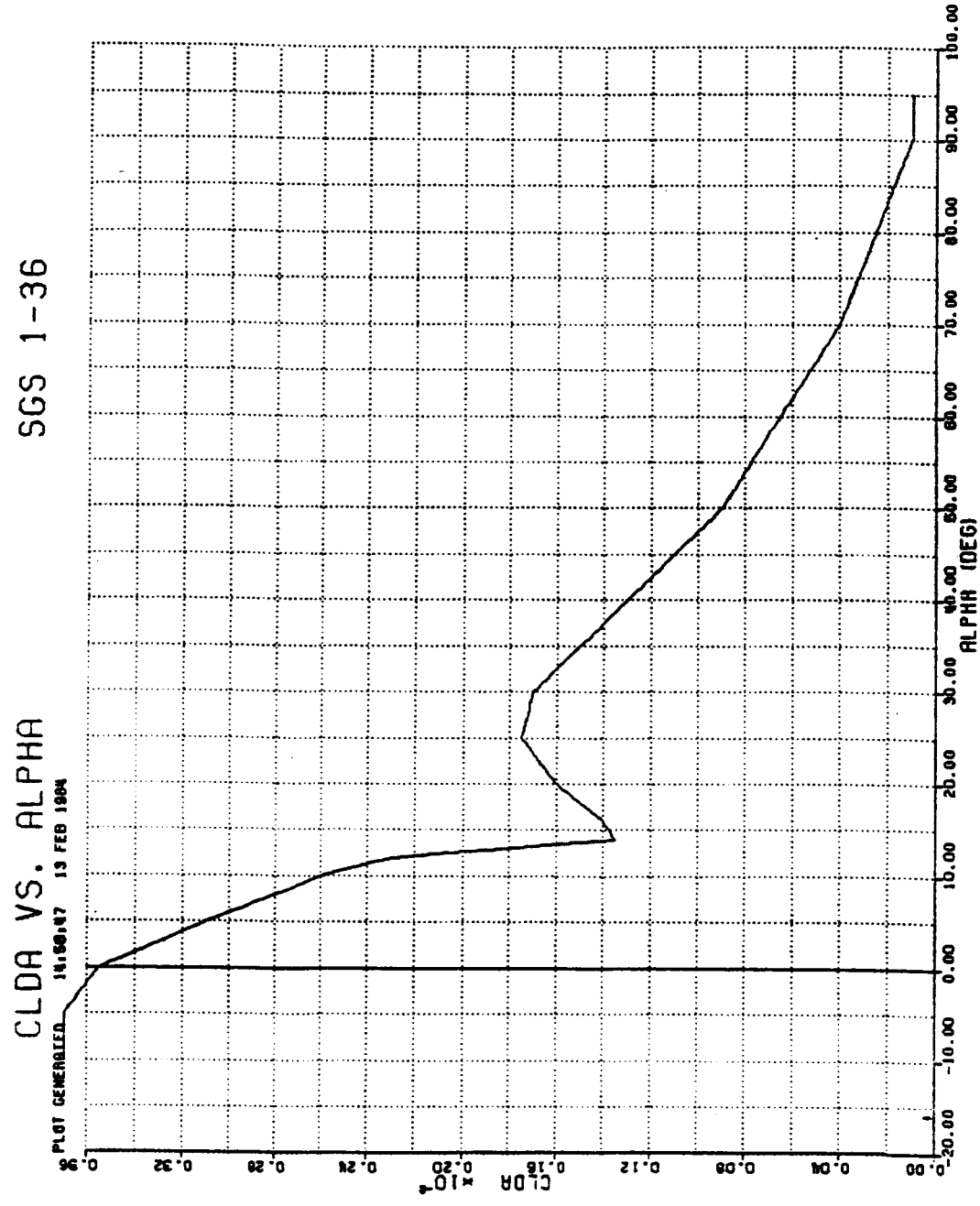
CLDA VS. ALPHA
SGS 1-36
PLOT GENERATED 13 FEB 1984
CLDA x10⁻⁴
ALPHA (DEG)
0.00
0.04
0.08
0.12
0.16
0.20
0.24
0.28
0.32
0.36
-20.00
-10.00
0.00
10.00
20.00
30.00
40.00
50.00
60.00
70.00
80.00
90.00
100.00

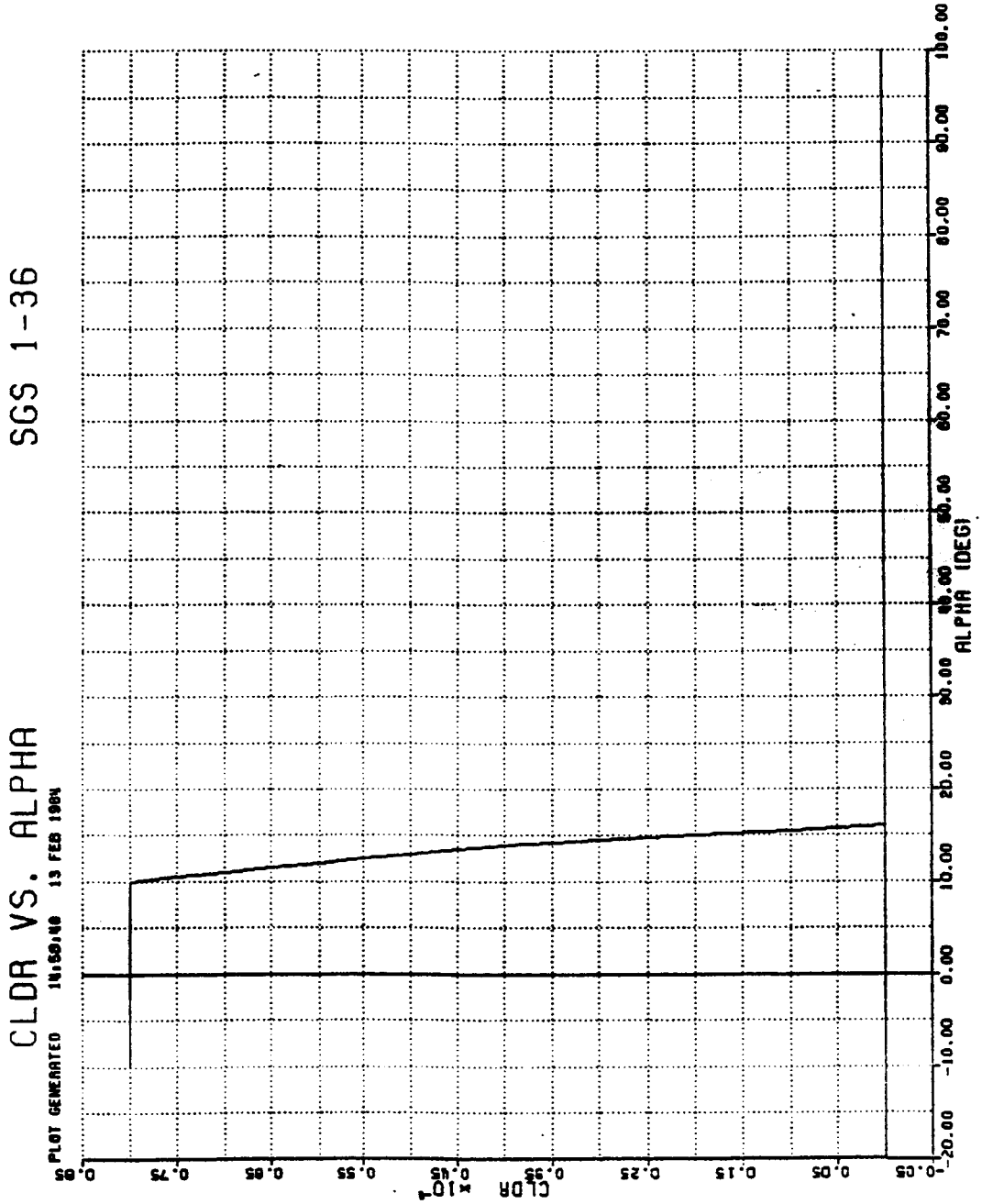
CLDR VS. ALPHA
SGS 1-36
PLOT GENERATED 14:50:48 13 FEB 1984
CLDR x10⁻⁴
0.05
0.15
0.25
0.35
0.45
0.55
0.65
0.75
0.85
ALPHA (DEG)
-20.00
-10.00
0.00
10.00
20.00
30.00
40.00
50.00
60.00
70.00
80.00
90.00
100.00

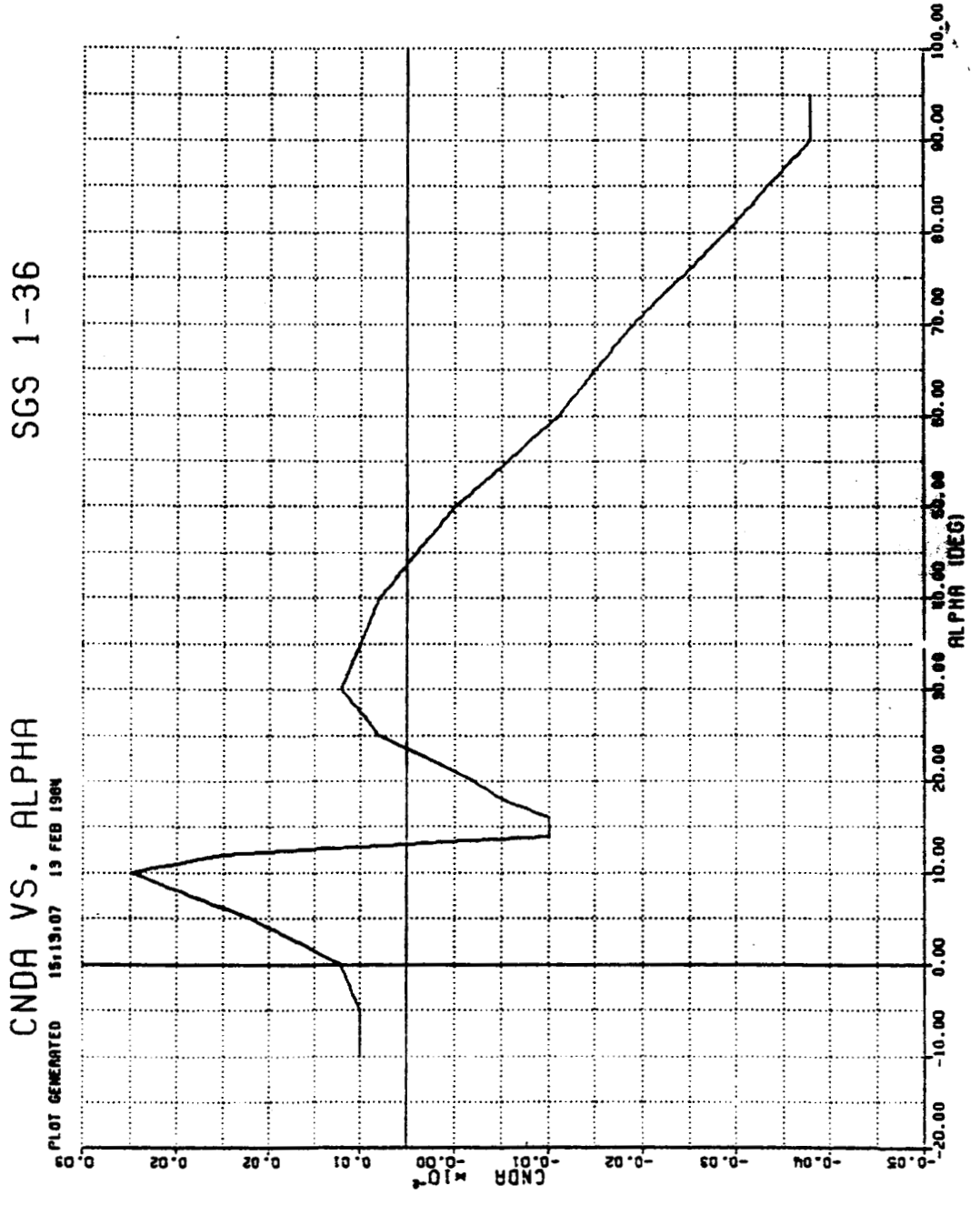
CNDA VS. ALPHA
SGS 1-36
PLOT GENERATED 15:13:07 13 FEB 1984
CNDA x10^-4
ALPHA (DEG)
0.03
0.02
0.02
0.01
-0.00
-0.01
-0.02
-0.03
-0.04
-0.05
100.00
90.00
80.00
70.00
60.00
50.00
40.00
30.00
20.00
10.00
0.00
-10.00
-20.00

ORIGINAL PAGE IS
OF POOR QUALITY

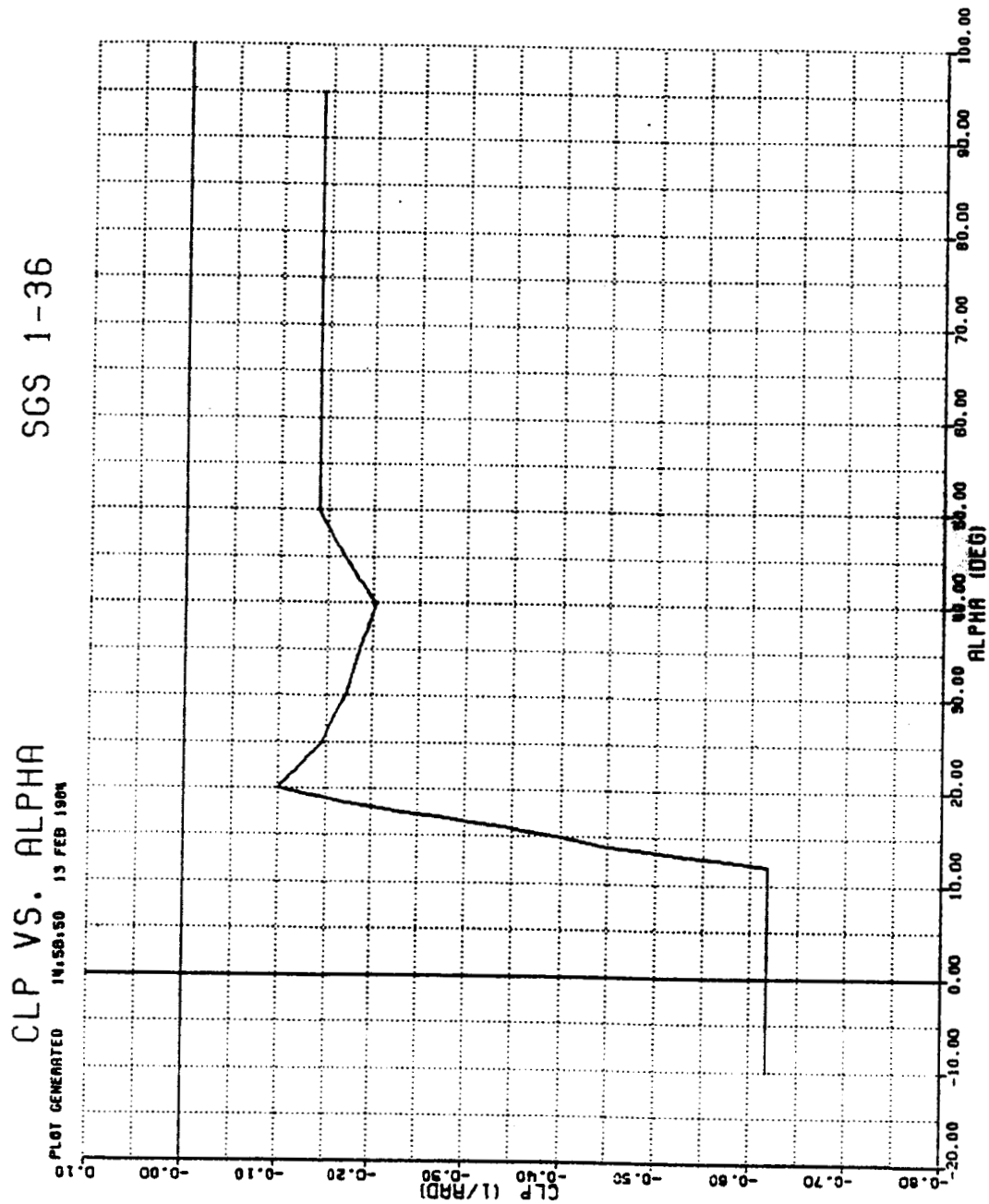

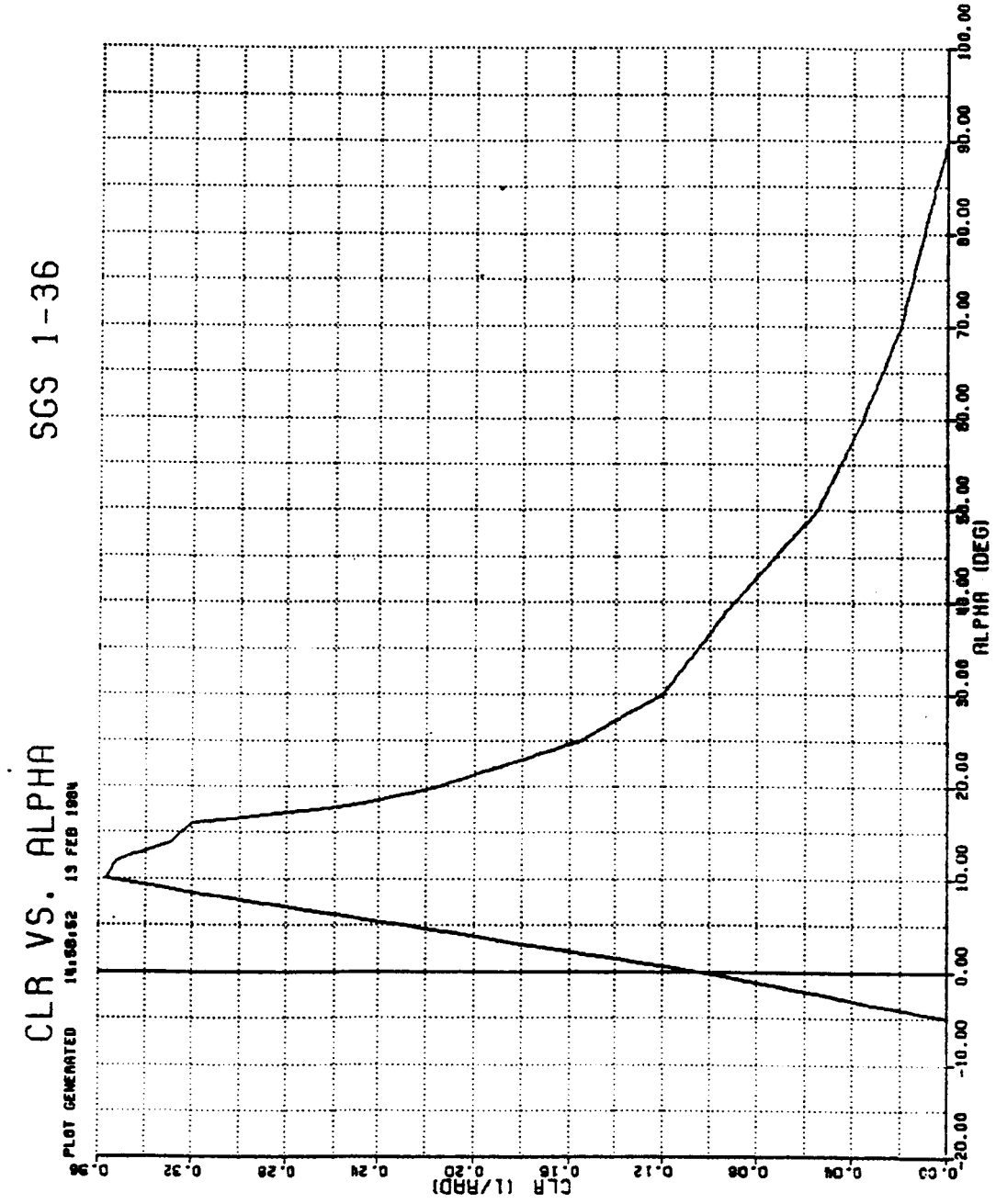
CLR VS. ALPHA
SGS 1-36
PLOT GENERATED 14:58:52 13 FEB 1984
CLR (1/RAD)
ALPHA (DEG)
0.00
0.04
0.08
0.12
0.16
0.20
0.24
0.28
0.32
0.36
-20.00
-10.00
0.00
10.00
20.00
30.00
40.00
50.00
60.00
70.00
80.00
90.00
100.00

ORIGINAL PAGE IS
OF POOR QUALITY

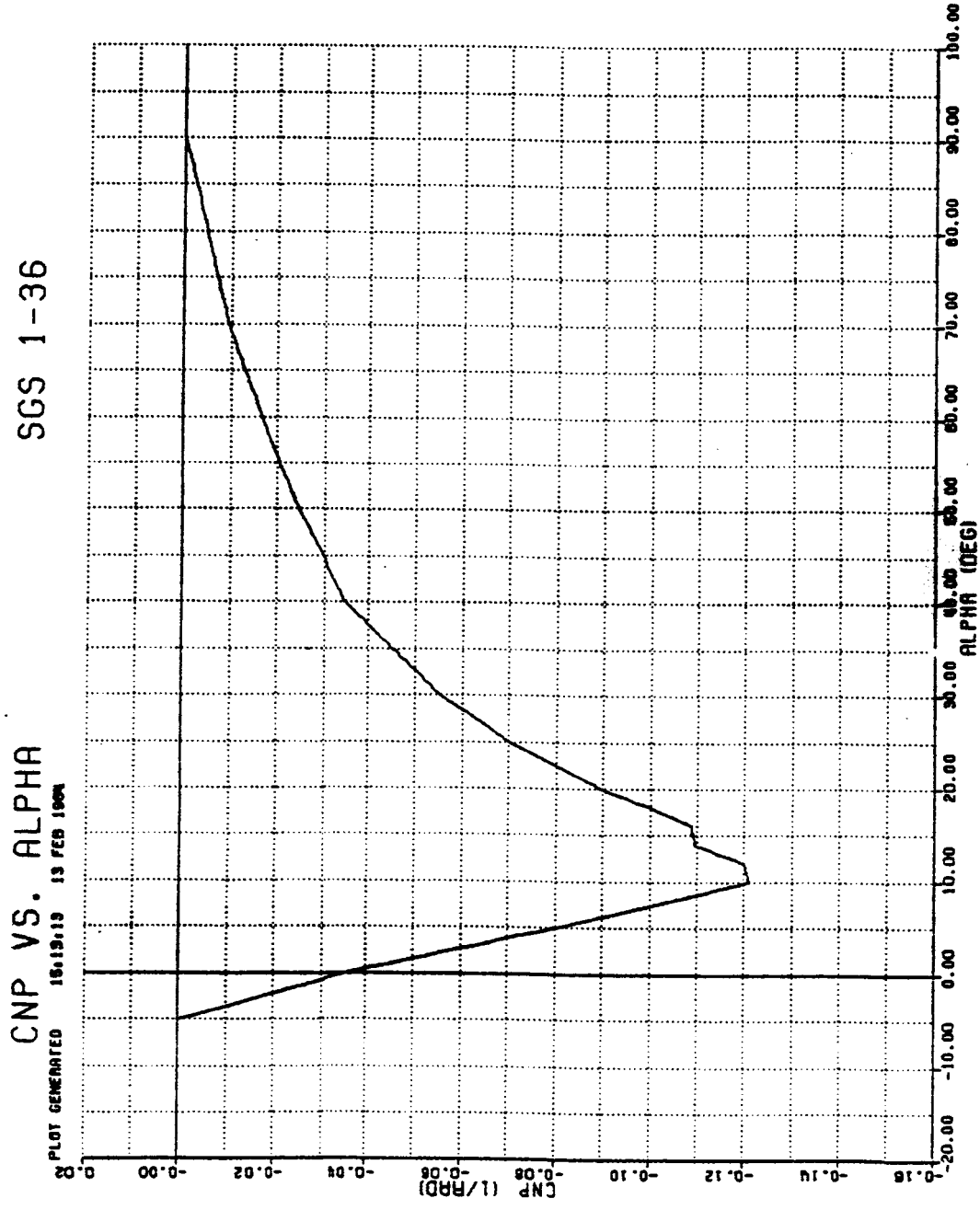

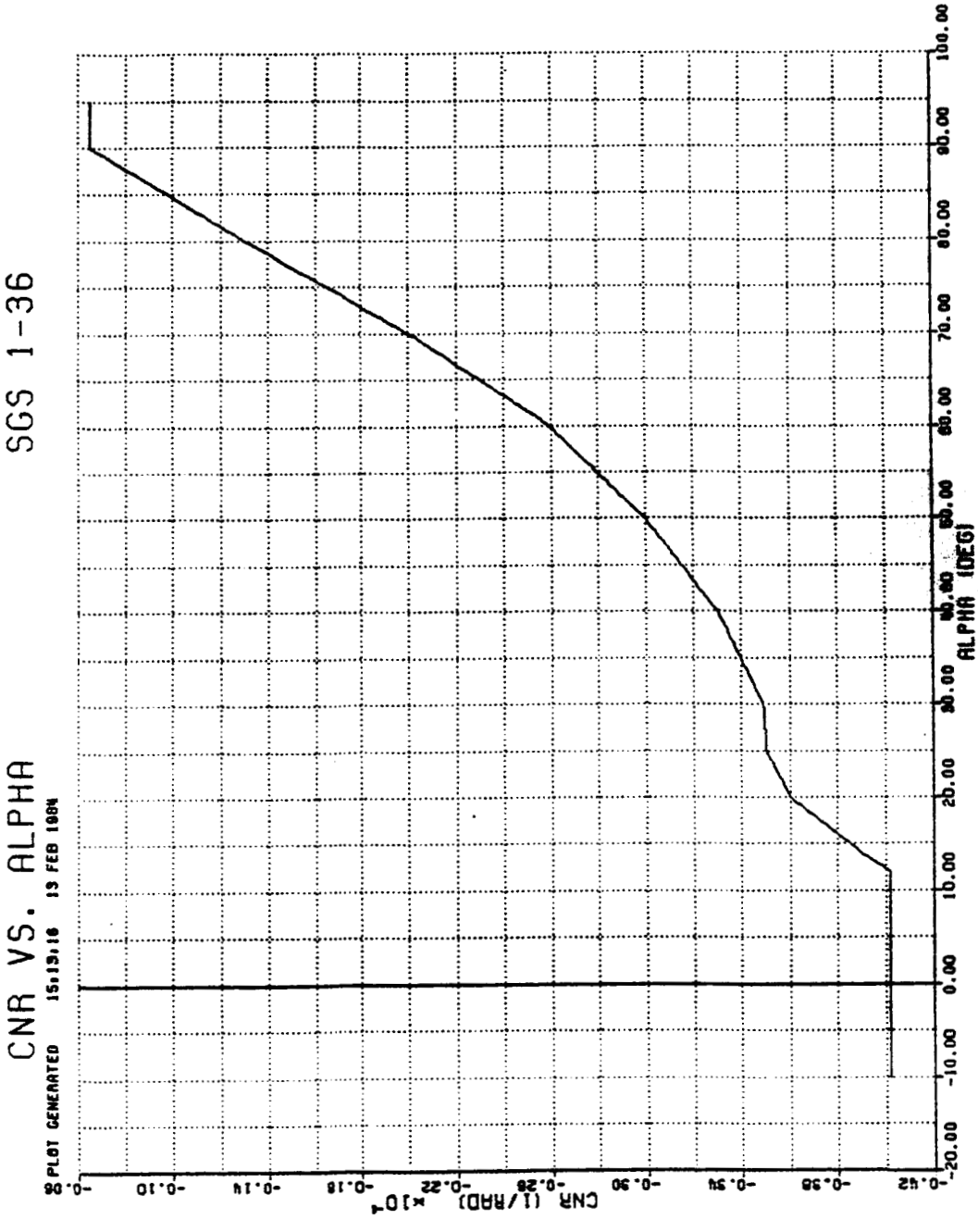
CNR VS. ALPHA
SGS 1-36
PLOT GENERATED 15:13:16 13 FEB 1984
CNR (1/RAD) x10⁻⁴
-0.02
-0.06
-0.10
-0.14
-0.18
-0.22
-0.26
-0.30
-0.34
-0.38
-0.42
ALPHA (DEG)
-20.00
-10.00
0.00
10.00
20.00
30.00
40.00
50.00
60.00
70.00
80.00
90.00
100.00

ORIGINAL PAGE IS
OF POOR QUALITY

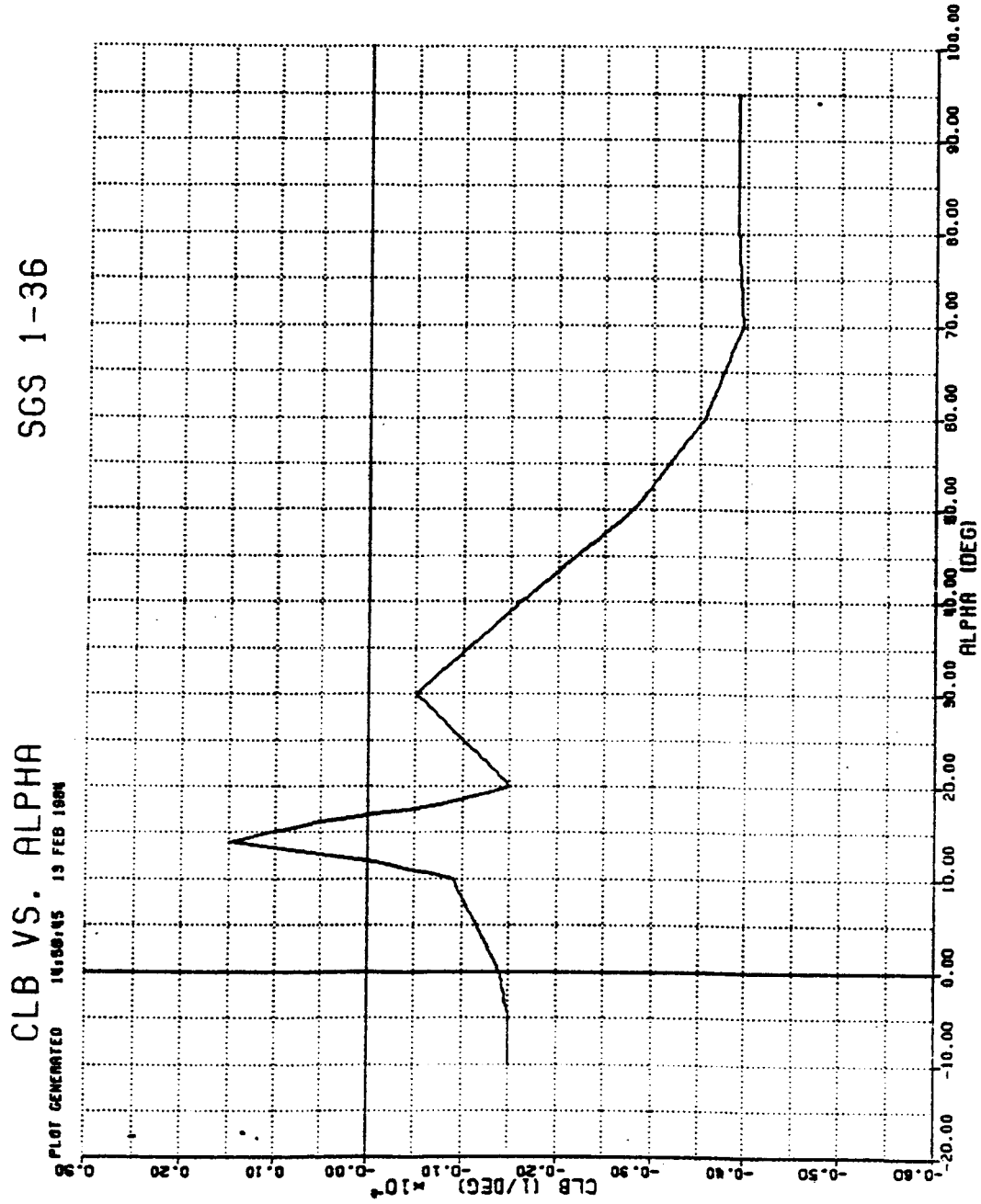

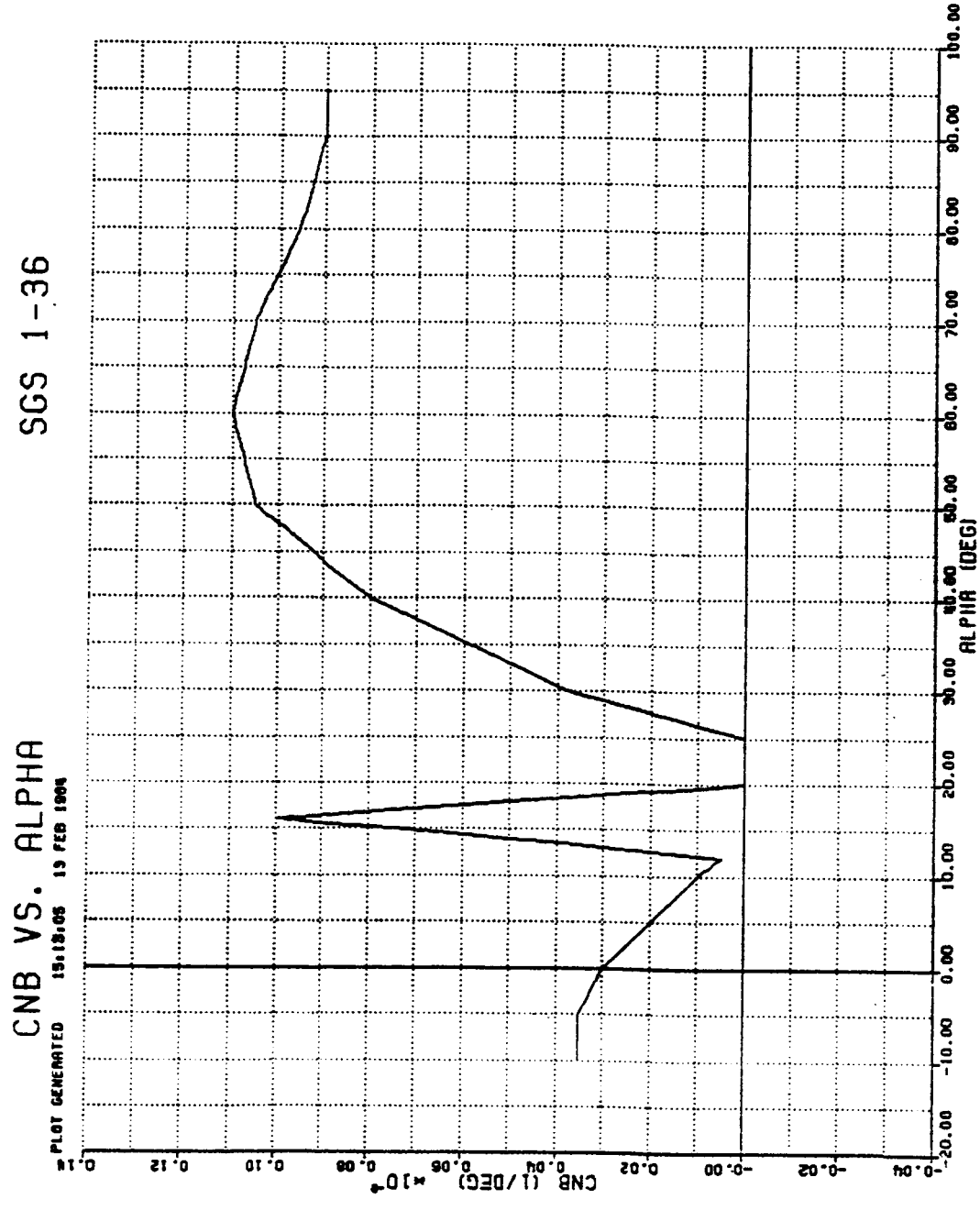
CNB VS. ALPHA
SGS 1-36
PLOT GENERATED 15:15:05 13 FEB 1986
CNB (1/DEG) *10**4
ALPHA (DEG)
0.14
0.12
0.10
0.08
0.06
0.04
0.02
0.00
-0.02
-0.04
100.00
90.00
80.00
70.00
60.00
50.00
40.00
30.00
20.00
10.00
0.00
-10.00
-20.00

C-2

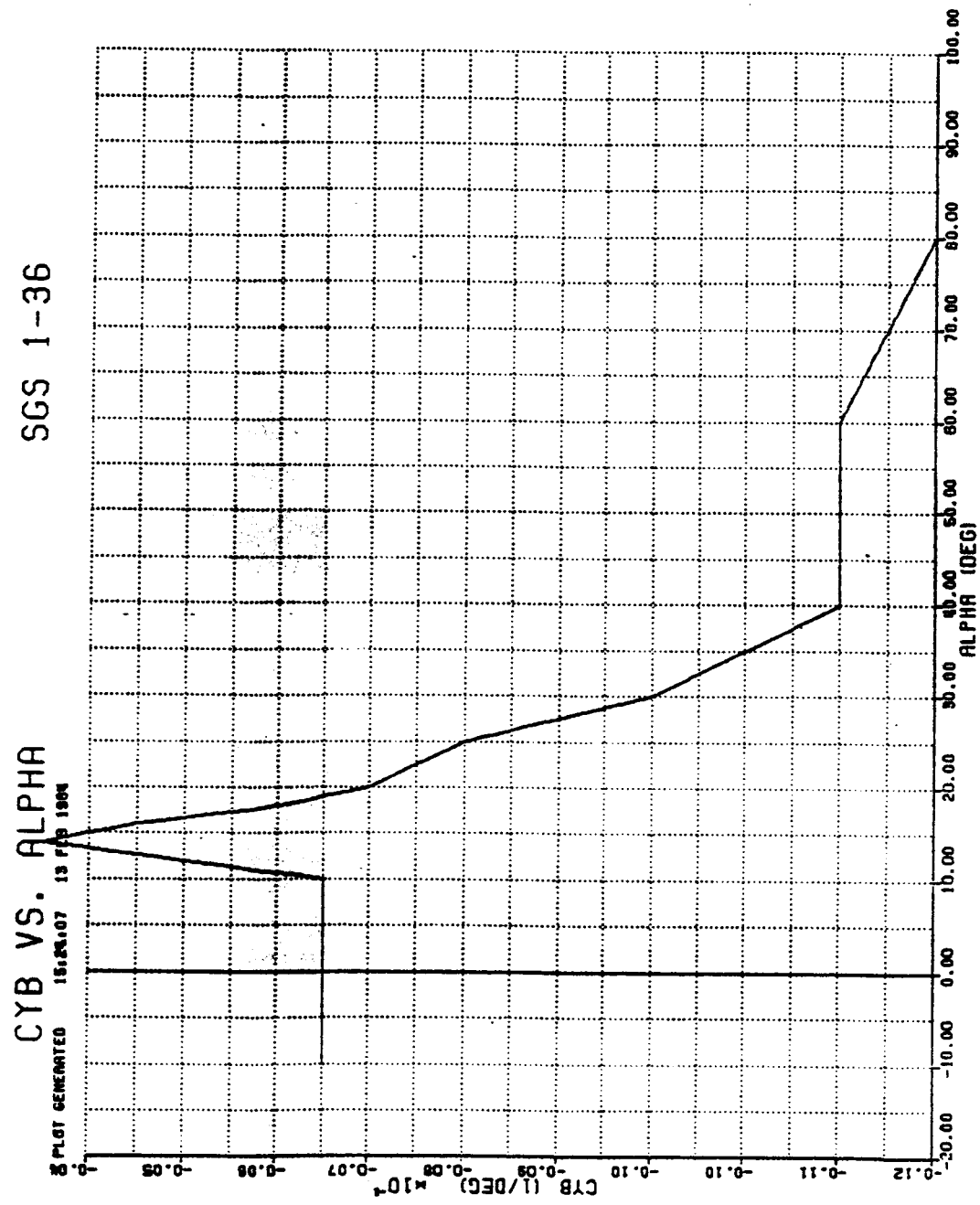
CYB VS. ALPHA
SGS 1-36
CYB (1/DEG) *10**-4
ALPHA (DEG)
0.00
-0.01
-0.02
-0.03
-0.04
-0.05
-0.06
-0.07
-0.08
-0.09
-0.10
-0.11
-0.12
-20.00
-10.00
0.00
10.00
20.00
30.00
40.00
50.00
60.00
70.00
80.00
90.00
100.00

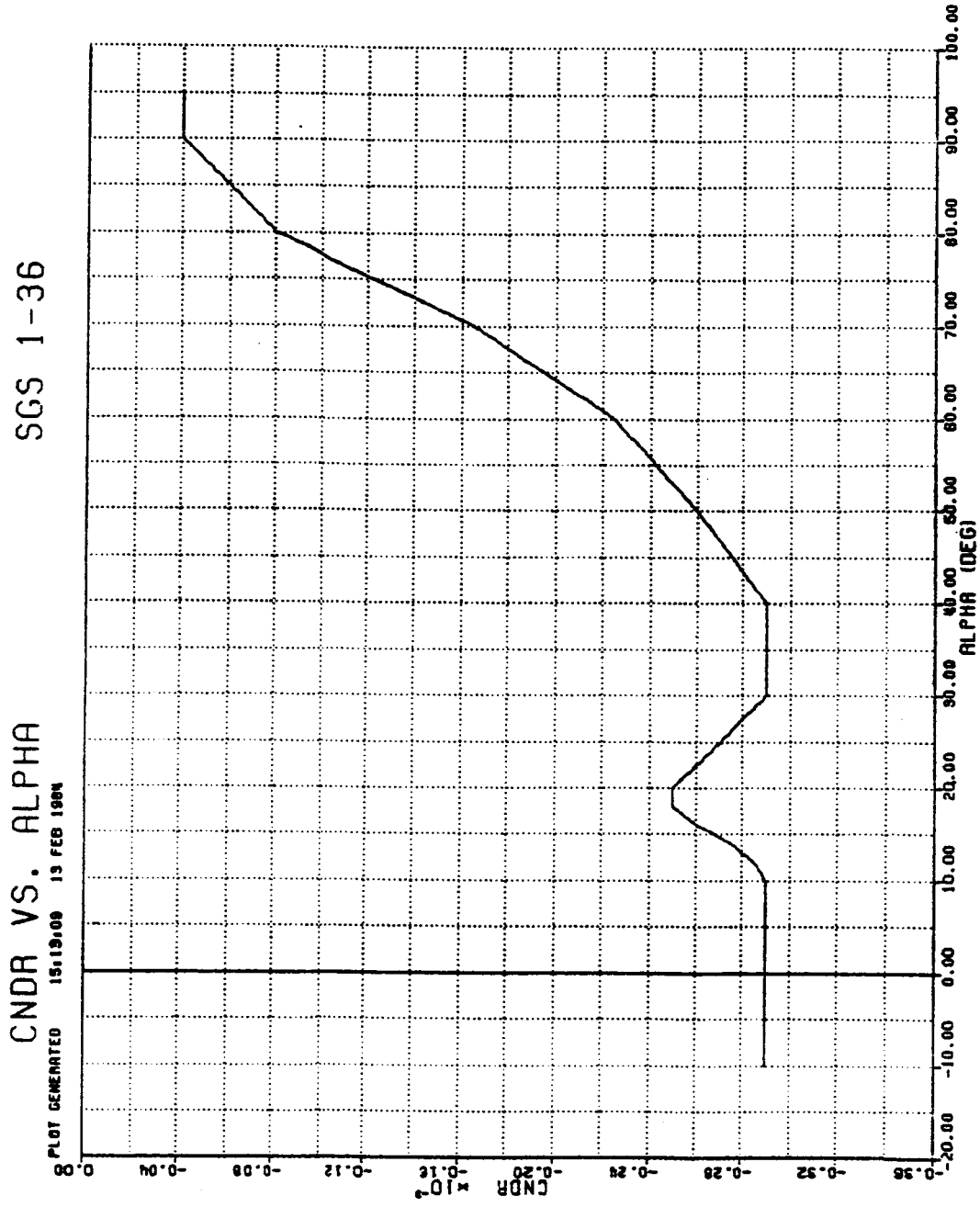
CNDR VS. ALPHA
SGS 1-36
PLOT GENERATED 15:19:00 13 FEB 1984
CNDR x10⁻³
0.00
-0.04
-0.08
-0.12
-0.16
-0.20
-0.24
-0.28
-0.32
-0.36
ALPHA (DEG)
100.00
90.00
80.00
70.00
60.00
50.00
40.00
30.00
20.00
10.00
0.00
-10.00
-20.00

Appendix B: Linearized equations of motion as used by the Modified Maximum Likelihood Estimation program.

The general form of the equations is:

$$R(t)\dot{x}(t) = A(t)x(t) + B(t)u(t) + S(t)$$

$$z(t) = C(t)x(t) + D(t)u(t) + H(t) + E(t)\dot{x}(t)$$

where A, B, S, R, C, D, H, and E are defined by relationships such as:

$$A_{ij}(t) = AM_{ij}(t) \times AN_{ij} + AL_{ij}(t)$$

The α_c and β_c used are obtained from α_m and β_m by the equations:

$$\alpha_c = \frac{\alpha_m}{KALF} + \frac{q(XALF + DCGFT)}{V} - \frac{pYALF}{V}$$

$$\beta_c = \frac{\beta_m}{KB} + \frac{pZB}{V} - \frac{r(XB + DCGFT)}{V}$$

where,

α_m Measured angle of attack

α_c Computed angle of attack

β_m Measured angle of sideslip

β_c Computed angle of sideslip

KALF Flow amplification factor for angle of attack

DCGFT Flight C.G. minus wind tunnel C.G.

XAN Longitudinal location of the normal acceleration sensor

XAY Longitudinal location of the lateral acceleration sensor

ZAX Vertical location of the longitudinal acceleration sensor

ZAY Vertical location of the lateral acceleration sensor

Longitudinal. - The nondimensional longitudinal matrices are:

$$AN = \begin{bmatrix} C_{L_\alpha} & C_{L_q} & 0 \\ C_{m_\alpha} & C_{m_q} & 0 \\ 0 & 0 & 0 \end{bmatrix} \qquad BN = \begin{bmatrix} C_{L_{\delta_e}} \\ C_{m_{\delta_e}} \\ 0 \end{bmatrix} \qquad SN = \begin{bmatrix} C_{L_0} + \dot{\alpha}_0 \\ C_{m_0} \\ \dot{\theta}_0 \end{bmatrix} \qquad RN = \begin{bmatrix} 1 & 0 & 0 \\ C_{m_{\dot{\alpha}}} & 1 & 0 \\ 0 & 0 & 1 \end{bmatrix}$$

$$CN = \begin{bmatrix} \text{KALF} & \text{KALF} \times (\text{XALF} + \text{DCGFT}) & 0 \\ 0 & 1 & 0 \\ 0 & 0 & 1 \\ C_{N_\alpha} & C_{N_q} & 0 \\ C_{A_\alpha} & C_{A_q} & 0 \\ 0 & 0 & 0 \end{bmatrix} \qquad DN = \begin{bmatrix} 0 \\ 0 \\ 0 \\ C_{N_{\delta_e}} \\ C_{A_{\delta_e}} \end{bmatrix}$$

$$HN = \begin{bmatrix} 0 \\ 0 \\ 0 \\ C_{N_0} \\ C_{A_0} \end{bmatrix} \qquad EN = \begin{bmatrix} 0 & 0 & 0 \\ 0 & 0 & 0 \\ 0 & 0 & 0 \\ 0 & \text{XAN} + \text{DCGFT} & 0 \\ 0 & \text{ZAX} & 0 \\ 0 & 1 & 0 \end{bmatrix}$$

The longitudinal dimensionalization matrices defined by the user routines are:

AM —

$$\begin{bmatrix} -\frac{\bar{q}s}{mV}\mathcal{R} & \frac{\bar{q}s}{mV}\frac{c}{2V} & 1 \\ \frac{\bar{q}sc}{I_y}\mathcal{R} & \frac{\bar{q}sc}{I_y}\frac{c}{2V} & 1 \\ 1 & 1 & 1 \end{bmatrix}$$

BM —

$$\begin{bmatrix} -\frac{\bar{q}s}{mV}\mathcal{R} & -\frac{\bar{q}s}{mV}\mathcal{R} & -\frac{\bar{q}s}{mV}\mathcal{R} & -\frac{\bar{q}s}{mV}\mathcal{R} \\ -\frac{\bar{q}sc}{I_y}\mathcal{R} & -\frac{\bar{q}sc}{I_y}\mathcal{R} & -\frac{\bar{q}sc}{I_y}\mathcal{R} & -\frac{\bar{q}sc}{I_y}\mathcal{R} \\ 1 & 1 & 1 & 1 \end{bmatrix}$$

SM —

$$\begin{bmatrix} \frac{\bar{q}s}{mV}\mathcal{R} & -\frac{\bar{q}s}{mV}\mathcal{R} & -\frac{\bar{q}s}{mV}\mathcal{R} & -\frac{\bar{q}s}{mV}\mathcal{R} \\ -\frac{\bar{q}sc}{I_y}\mathcal{R} & -\frac{\bar{q}sc}{I_y}\mathcal{R} & -\frac{\bar{q}sc}{I_y}\mathcal{R} & -\frac{\bar{q}sc}{I_y}\mathcal{R} \\ 1 & 1 & 1 & 1 \end{bmatrix}$$

RM —

$$\begin{bmatrix} 1 & 1 & 1 \\ -\frac{qsc}{I_y}\frac{c}{2V} & 1 & 1 \\ 1 & 1 & 1 \end{bmatrix}$$

CM —

$$\begin{bmatrix} 1 & -\frac{1}{V} & 1 \\ 1 & 1 & 1 \\ 1 & 1 & 1 \\ \frac{\bar{q}s}{mg} & \frac{\bar{q}s}{mg}\frac{c}{2V\mathcal{R}} & 1 \\ -\frac{\bar{q}s}{mg} & -\frac{\bar{q}s}{mg}\frac{c}{2V\mathcal{R}} & 1 \end{bmatrix}$$

DM —

$$\begin{bmatrix} 1 & 1 & 1 & 1 \\ 1 & 1 & 1 & 1 \\ 1 & 1 & 1 & 1 \\ \frac{qs}{mg} & \frac{qs}{mg} & \frac{qs}{mg} & \frac{qs}{mg} \\ -\frac{qs}{mg} & -\frac{qs}{mg} & -\frac{qs}{mg} & -\frac{qs}{mg} \end{bmatrix}$$

EM —

$$\begin{bmatrix} 1 & 1 & 1 \\ 1 & 1 & 1 \\ 1 & 1 & 1 \\ 1 & \frac{1}{g\mathcal{R}} & 1 \\ 1 & \frac{1}{g\mathcal{R}} & 1 \end{bmatrix}$$

HM —

$$\begin{bmatrix} 1 & 1 & 1 & 1 \\ 1 & 1 & 1 & 1 \\ 1 & 1 & 1 & 1 \\ \frac{qs}{mg} & \frac{qs}{mg} & \frac{qs}{mg} & \frac{qs}{mg} \\ -\frac{qs}{mg} & -\frac{qs}{mg} & -\frac{qs}{mg} & -\frac{qs}{mg} \end{bmatrix}$$

The *FM* matrix is filled with 1's.

$$AL = \begin{bmatrix} 0 & 1 & \frac{g}{V}(-\cos\varphi \sin\theta \cos\alpha_c + \cos\theta \sin\alpha_c) \\ 0 & 0 & 0 \\ 0 & \cos\varphi & 0 \end{bmatrix}$$

The *BL*, *SL*, *CL*, *DL*, *HL*, and *EL* matrices are filled with 0's.

Lateral-directional. - The nondimensional lateral-directional matrices are:

$$AN = \begin{bmatrix} C_{Y_\beta} & C_{Y_p} & C_{Y_r} & 0 \\ C_{\ell_\beta} & C_{\ell_p} & C_{\ell_r} & 0 \\ C_{n_\beta} & C_{n_p} & C_{n_r} & 0 \\ 0 & 0 & 0 & 0 \end{bmatrix} \qquad BN = \begin{bmatrix} C_{Y_{\delta_a}} & C_{Y_{\delta_r}} \\ C_{\ell_{\delta_a}} & C_{\ell_{\delta_r}} \\ C_{n_{\delta_a}} & C_{n_{\delta_r}} \\ 0 & 0 \end{bmatrix}$$

$$SN = \begin{bmatrix} C_{Y_0} - \dot{\beta}_0 \\ C_{\ell_0} \\ C_{n_0} \\ \dot{\varphi}_0 \end{bmatrix}$$

RN —

$$\begin{bmatrix} 1 & 0 & 0 & 0 \\ C_{\ell_\beta} & 1 & -\frac{I_{xz}}{I_x} & 0 \\ C_{n_\beta} & -\frac{I_{xz}}{I_z} & 1 & 0 \\ 0 & 0 & 0 & 1 \end{bmatrix}$$

CN —

$$\begin{bmatrix} \text{KB} & \text{KB} \times \text{ZB} & \text{KB} \times (\text{XB} + \text{DCGFT}) & 0 \\ 0 & 1 & 0 & 0 \\ 0 & 0 & 1 & 0 \\ 0 & 0 & 0 & 1 \\ C_{Y_\beta} & C_{Y_p} & C_{Y_r} & 0 \\ 0 & 0 & 0 & 0 \\ 0 & 0 & 0 & 0 \end{bmatrix}$$

DN —

$$\begin{bmatrix} 0 & 0 \\ 0 & 0 \\ 0 & 0 \\ 0 & 0 \\ C_{Y_{\delta_a}} & C_{Y_{\delta_r}} \end{bmatrix}$$

HN —

$$\begin{bmatrix} 0 \\ 0 \\ 0 \\ 0 \\ C_{Y_0} \end{bmatrix}$$

EN —

$$\begin{bmatrix} 0 & 0 & 0 & 0 \\ 0 & 0 & 0 & 0 \\ 0 & 0 & 0 & 0 \\ 0 & 0 & 0 & 0 \\ 0 & \text{ZAY} & \text{XAY} + \text{DCGFT} & 0 \\ 0 & 1 & 0 & 0 \\ 0 & 0 & 1 & 0 \end{bmatrix}$$

The dimensionalization matrices defined by the standard aircraft routines for a lateral-directional case are:

AM —

$$\begin{bmatrix} \frac{\bar{q}s}{mV}\mathcal{R} & \frac{\bar{q}s}{mV}\frac{b}{2V} & \frac{\bar{q}s}{mV}\frac{b}{2V} & 1 \\ \frac{\bar{q}sb}{I_x}\mathcal{R} & \frac{\bar{q}sb}{I_x}\frac{b}{2V} & \frac{\bar{q}sb}{I_x}\frac{b}{2V} & 1 \\ \frac{\bar{q}sb}{I_z}\mathcal{R} & \frac{\bar{q}sb}{I_z}\frac{b}{2V} & \frac{\bar{q}sb}{I_z}\frac{b}{2V} & 1 \\ 1 & 1 & 1 & 1 \end{bmatrix}$$

BM —

$$\begin{bmatrix} \frac{\bar{q}s}{mV}\mathcal{R} & \frac{\bar{q}s}{mV}\mathcal{R} & \frac{\bar{q}s}{mV}\mathcal{R} & \frac{\bar{q}s}{mV}\mathcal{R} \\ \frac{\bar{q}sb}{I_x}\mathcal{R} & \frac{\bar{q}sb}{I_x}\mathcal{R} & \frac{\bar{q}sb}{I_x}\mathcal{R} & \frac{\bar{q}sb}{I_x}\mathcal{R} \\ \frac{\bar{q}sb}{I_z}\mathcal{R} & \frac{\bar{q}sb}{I_z}\mathcal{R} & \frac{\bar{q}sb}{I_z}\mathcal{R} & \frac{\bar{q}sb}{I_z}\mathcal{R} \\ 1 & 1 & 1 & 1 \end{bmatrix}$$

SM —

$$\begin{bmatrix} \frac{\bar{q}s}{mV}\mathcal{R} & \frac{\bar{q}s}{mV}\mathcal{R} & \frac{\bar{q}s}{mV}\mathcal{R} & \frac{\bar{q}s}{mV}\mathcal{R} \\ \frac{\bar{q}sb}{I_x}\mathcal{R} & \frac{\bar{q}sb}{I_x}\mathcal{R} & \frac{\bar{q}sb}{I_x}\mathcal{R} & \frac{\bar{q}sb}{I_x}\mathcal{R} \\ \frac{\bar{q}sb}{I_z}\mathcal{R} & \frac{\bar{q}sb}{I_z}\mathcal{R} & \frac{\bar{q}sb}{I_z}\mathcal{R} & \frac{\bar{q}sb}{I_z}\mathcal{R} \\ 1 & 1 & 1 & 1 \end{bmatrix}$$

RM —

$$\begin{bmatrix} 1 & 1 & 1 & 1 \\ -\frac{\bar{q}sb}{I_x}\frac{b}{2V} & 1 & 1 & 1 \\ -\frac{\bar{q}sb}{I_x}\frac{b}{2V} & 1 & 1 & 1 \\ 1 & 1 & 1 & 1 \end{bmatrix}$$

CM —

$$\begin{bmatrix} 1 & -\frac{1}{V} & \frac{1}{V} & 1 \\ 1 & 1 & 1 & 1 \\ 1 & 1 & 1 & 1 \\ 1 & 1 & 1 & 1 \\ \frac{\bar{q}s}{mg} & \frac{\bar{q}s}{mg}\frac{b}{2V\mathcal{R}} & \frac{\bar{q}s}{mg}\frac{b}{2V\mathcal{R}} & 1 \\ 1 & 1 & 1 & 1 \\ 1 & 1 & 1 & 1 \end{bmatrix}$$

DM —

$$\begin{bmatrix} 1 & 1 & 1 & 1 \\ 1 & 1 & 1 & 1 \\ 1 & 1 & 1 & 1 \\ 1 & 1 & 1 & 1 \\ \frac{\bar{q}s}{mg} & \frac{\bar{q}s}{mg} & \frac{\bar{q}s}{mg} & \frac{\bar{q}s}{mg} \\ 1 & 1 & 1 & 1 \\ 1 & 1 & 1 & 1 \end{bmatrix}$$

$$HM = \begin{bmatrix} 1 & 1 & 1 & 1 \\ 1 & 1 & 1 & 1 \\ 1 & 1 & 1 & 1 \\ 1 & 1 & 1 & 1 \\ \frac{\bar{q}s}{mg} & \frac{\bar{q}s}{mg} & \frac{\bar{q}s}{mg} & \frac{\bar{q}s}{mg} \\ 1 & 1 & 1 & 1 \\ 1 & 1 & 1 & 1 \end{bmatrix} \qquad EM = \begin{bmatrix} 1 & 1 & 1 & 1 \\ 1 & 1 & 1 & 1 \\ 1 & 1 & 1 & 1 \\ 1 & 1 & 1 & 1 \\ 1 & -\frac{1}{g\mathcal{R}} & \frac{1}{g\mathcal{R}} & 1 \\ 1 & 1 & 1 & 1 \\ 1 & 1 & 1 & 1 \end{bmatrix}$$

The *FM* matrix is filled with 1's.

$$AL = \begin{bmatrix} 0 & \sin\alpha & -\cos\alpha & \cos\varphi\cos\theta\,\frac{g}{V} \\ 0 & 0 & 0 & 0 \\ 0 & 0 & 0 & 0 \\ 0 & 1 & \cos\varphi\tan\theta & 0 \end{bmatrix}$$

The *BL*, *SL*, *RL*, *CL*, *DL*, *HL*, *EL*, and *FL* matrices are filled with 0's.

Appendix C: The following equation was developed to estimate the value of Cl_p for the angles of attack of between 30 and 90 degrees.

It is assumed that since the wings are completely stalled above 20 degrees angle of attack, it is reasonable to consider the normal force (or drag at high angles) to be the primary damping force.

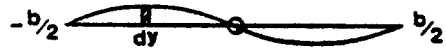

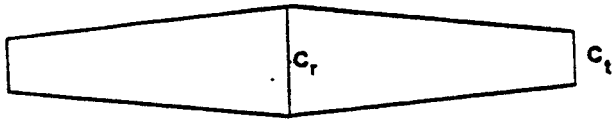

We have:

$$C_{local} = C_r - 2y/b(C_r - C_t) \text{ for } +y \quad (1)$$

Let:

$$\lambda = 2/b(C_r - C_t) \quad (2)$$

And rolling moment Cl to be:

$$Cl = \int_{-b/2}^{b/2} CN \cdot y \cdot \bar{q}_{local} \cdot C_{local} \, dy \; / \; \bar{q}_{\infty} \cdot s \cdot b \quad (3)$$

For positive P,

$$V_{local} = P\,y + V_\infty \qquad (4)$$

$$\bar{q}_{local} = 1/2\,\rho\,(P\,y + V_\infty)^2 \qquad (5)$$

and we know that:

$$\bar{q}_\infty = 1/2\,\rho\,V_\infty^2 \qquad (6)$$

$$CN = f\,(\alpha_{local}) \qquad (7)$$

$$\alpha_{local} = \alpha_\infty + \Delta\alpha \qquad (8)$$

$$\Delta\alpha = f\,(P\,y) \qquad (9)$$

substituting the equations 1, 5, and 6 into equation 3 we have:

$$Cl = CN\left\{\int_0^{b/2} y(Py+V_\infty)^2(C_r - \lambda y)\,dy + \int_{-b/2}^{0} y(Py+V_\infty)^2(C_r + \lambda y)\,dy\right\}/\,V_\infty^2\,s\,b \qquad (10)$$

integrating equation 10 we will have,

$$Cl = CN/\,V_\infty\,s\,(b^2/6\;C_r\;P - b^3/16\;\lambda\,P) \qquad (11)$$

and finally,

$$Cl_P = CN/2\,s\,b\,(b^2/6\;C_r - b^3/16\;\lambda) \qquad (12)$$

Since the value of CN as a function of α has been determined from the wind tunnel data the parameter Cl_p can now be calculated using equation 12.